CERN-THESIS-2014-101
26/09/2014

DISSERTATION

A CVD Diamond Detector for (n,α) Cross-Section Measurements

Ausgeführt zum Zwecke der Erlangung des akademischen Grades einer Doktorin der technischen Wissenschaften unter der Leitung von

Univ.Prof. Dr.techn. Gerald Badurek
Atominstitut der Österreichischen Universitäten (E141)
Technische Universität Wien

Weitere Betreuer:

Univ.Doz. Dr.techn. Erich Griesmayer
Technische Universität Wien

Dr. Carlos Guerrero
Universidad de Sevilla

eingereicht an der Technischen Universität Wien
Fakultät für Physik

von

Christina Weiss
9602317
Volkgasse 14, 1130 Wien

Genf, am 13. Juni 2014

Weiss Christina

Die vorliegende Arbeit wurde unterstützt vom

Österreichischen Bundesministerium für Wissenschaft und Forschung
im Rahmen des
CERN Austrian Doctoral Student Programme

sowie gesponsert von

CIVIDEC Instrumentation GmbH, Vienna, Austria
im Rahmen von
Grant Agreement 2507/2010

Acknowledgements

My research project started as a vague idea in 2010 and only through the possibilities which the generous funding of CIVIDEC Instrumentation GmbH and the 'Austrian doctoral students program' at CERN offered, it could become reality.
I was lucky to have three people who closely followed the development of my project at CERN and supported me whenever they could. Erich Griesmayer made me become a critical experimentalist, taught me how to perform a measurement and analyze data and shared my enthusiasm throughout the project. I want to thank him for numerous intensive discussions, for performing last-minute night shifts whenever they were needed and his honesty. Carlos Guerrero opened for me the door to experimental nuclear physics and spared no effort to help me whenever needed. I want to thank him for his critical feed-back, the detailed corrections and his friendship. Enrico Chiaveri strengthened my believe that 'anything is possible'. I want to thank him for his endless support, his trust in my work and the possibility to discuss everything in an open, 'non-diplomatic' way.
To introduce a new technology to a specific field in experimental physics and the development of a novel detector requires an enthusiastic team of experts and the support of various people. I want to specifically express my gratitude to the following people, who significantly contributed to the successful development of the Diamond Mosaic-Detector, and hope that my persistent 'telegram-style' is excused at this point:

- Bjorn Hallgren for silent enthusiasm, resulting in perfectly tailored electronics.
- Gunnar Ehrlich-Joop for a professional detector design, technical advice in various fields and accepting my naming.
- Michal Pomorski for making me improve my understanding for diamond detectors and teaching me how to metallize diamonds.
- The team of the 'laboratoire capteurs diamant' of CEA Saclay for hosting me and providing their equipment.
- Ian McGill for a perfectly bonded detector and a hint to my real destiny.
- Damien Grenier for technical advice, accepting my unprofessional drawings and enthusiasm for producing the components.
- Rui De Oliveira for the production of the DM-D PCBs.
- Jacek Pieron for the technical work in the background and 'last minute' solutions.
- Claudine Chery for teaching me how to solder MMIC connectors.
- Antonio Mongeluzzo for the vacuum chamber and pump as well as patience when I was trying to express my ideas in broken French.
- Matthias Schreck and his team for providing their interesting diamond material.
- Petra Riedler for providing me repeatedly with Si diodes and giving me a crash course in diode-carving.
- Heinz Pernegger for hosting me in the ATLAS inner-detector laboratory at CERN, despite the fact that I was an alien amongst high-energy physicists.

The cross-section measurement with the DM-D was only possible thanks to the n_TOF collaboration which keeps the facility at CERN alive and provides a great framework for interesting discussions about science and related topics. I want to thank especially Franz Käppeler for his support, for two star-photos and for providing the sample together with Paul Koehler. I thoroughly appreciated the private lecture in resonance analysis by Peter Schillebeeckx and his most professional supervision of the measurement and I want to thank Eric Berthoumieux as well as Andrea Tsinganis for their every-day help on the ground and a good team spirit. My thanks also go to Vasilis Vlachoudis for answering all questions that I could come up with and playing my 'EN/STI-EET rubber duck' when needed.

Apart from the people directly related to the detector production and the measurement, there were multiple people who supported my work and gave me the opportunity to expand my knowledge in various fields. Being member of the EN/STI-EET section at CERN I had the opportunity to learn FLUKA and I appreciated the numerous discussions and distractions during coffee breaks and lunch times. Anton Lechner introduced me to the features of object oriented programming and prevented me from throwing my computer out of the window, which I honestly want to thank him for.

I want to thank Erwin Jericha for his support, for giving me a private lecture in LabView programming and supplying me continuously with literature. I had the opportunity to participate in two exciting test-beams with Christoph Kurfürst and appreciated the discussions with Hendrik Jansen. I want to thank Phil Bryant for his detailed corrections of various drafts of publications and interesting discussions on diamond detectors. And finally I want to thank my 'doctor-father' Gerald Badurek for his support, his trust in my work and his patience for receiving the final manuscript.

Lastly I want to thank Dennis Upper, for cheering me up in times of desperation [1], my temporary and continuously changing family in Prevessin, for 'Monday-Night Mayhems' and other important distractions, my family and friends for giving me stability, love and all the really important things in life and my parents for giving me the possibility to study physics and much more!

Deutsche Kurzfassung der Dissertation

Die Einführung einer neuen Technologie für (n,α) Wechselwirkungsquerschnitts-Messungen am Neutronen-Flugzeitexperiment n_TOF am CERN war die Zielsetzung der vorliegenden Dissertation. Bei solch einem Experiment wird die Wahrscheinlichkeit, dass ein Neutron vom Kern eines vorliegenden Isotops eingefangen wird und darauf folgend ein α-Teilchen emittiert wird gemessen. Bei n_TOF wird dies in Abhängigkeit der Neutronenenergie E_n ermittelt, wobei mit 10^{-2} eV $\leq E_n \leq$ 20 GeV ein weiter Energiebereich zur Verfügung steht.

Die experimentelle Herausforderung bei (n,α) Messungen liegt in der Notwendigkeit sehr dünne Isotopen-Proben verwenden zu müssen, damit die α-Teichen auch tatsächlich die Probe verlassen und im Detektor ankommen können. Zusätzlich sind die im Interesse stehenden Wechselwirkungsquerschnitte of sehr gering. Dies erfordert einen Detektor der direkt im Neutronenstrahl positioniert werden kann um die Zählrate zu maximieren. Jegliche Materialien im Neutronenstrahl provozieren allerdings Hintergrundreaktionen die vom zu messenden Signal unterschieden werden müssen. Zusätzlich muss der Photonen-Hintergrund im Neutronenstrahl erfolgreich vom Signal abgezogen werden können. Dies kann am besten mit einem spektroskopischen Detektor bewerkstelligt werden. Für die Spektroskopie von α-Teilchen eignen sich besonders Festkörper-Detektoren, wobei CVD-Diamantsensoren aus Gründen der Strahlungstoleranz, der geringen Effizienz für Photonenmessungen und der Tatsache dass hoch-energetische Hintergrundreaktionen aufgrund Neutronen-induzierter Kernreaktionen in ^{12}C erst bei $E_n > 6$ MeV auftreten, besonders geeignet sind. Diese Argumente haben zur Entwicklung des 'Diamond Mosaic-Detector' (DM-D) geführt mit dem der ^{59}Ni(n,α)^{56}Fe Wechselwirkungsquerschnitt, mit besonderem Augenmerk auf das Resonanzintegral bei $E_n = 203$ eV, bei n_TOF im Jahr 2012 gemessen wurde, um Diskrepanzen zwischen zwei vergangenen Messungen dieser Reaktion (Harvey 1976 [2] und Koehler 1999 [3]) aufklären zu können.

Die vorliegende Dissertation teilt sich in vier Teile. Im ersten Teil ('Introduction') wird die Motivation für (n,α) Messungen dargelegt mit speziellem Fokus auf die gemessene ^{59}Ni(n,α)^{56}Fe Reaktion, die sowohl in der Astrophysik als auch in der Kerntechnologie eine wichtige Rolle spielt. Die experimentellen Herausforderungen und die Motivation für CVD Diamant sind ebenfalls in diesem Kapitel angeführt. In Kapitel 2 wird das n_TOF Experiment am CERN und dessen Charakteristika vorgestellt. Im darauffolgenden Kapitel werden die Grundbegriffe für Neutronen-induzierte Kernreaktionen eingeführt. Kapitel 4 gibt eine kurze Einführung in die Wechselwirkungsmechanismen verschiedener Teilchen mit Materie, der Grundlage fuer die Teilchendetektion. Die CVD-Diamant Technologie wird in Kapitel 5 vorgestellt, in dem auch die Entstehung des Detektorsignals anhand des Modells einer Kapazität dargestellt ist. Das letzte Kapitel im ersten Teil beschäftigt sich mit Elektronik, deren Auswirkung auf eine Messung und den Verstärkersystemen die für den DM-D verwendet wurden.

Der Detektor, bestehend aus einem Mosaik aus acht einkristallinen (sCVD) Diamant-Sensoren und einem 'Diamond on Iridium' (DOI) Sensor, ist im zweiten Teil der Arbeit ('The Diamond Mosaic-Detector') beschrieben. Kapitel 7 beschreibt das genaue Design und den Produktionsprozess des Detektors. Die Charakterisierung der verwendete Elektronik, die speziell für die Messung bei n_TOF optimiert wurde, ist im darauffolgenden Kapitel zu finden. Die Charakterisierung des Detektors ist in Kapitel 9 angegeben, bevor die Charakteristika des Detektors im letzten Kapitel des zweiten Teils zusammengefasst werden. Die beste α-Energieauflösung wurde

bei der Kalibration mit einer radioaktiven α-Quelle, mit $dE = 31$ keV bei $E_\alpha = 5.8$ MeV, für den Sensor DIAM2 gemessen.
Der dritte Teil der vorliegenden Arbeit ('Proof of Principle') beschäftigt sich mit der Messung mit dem DM-D bei n_TOF. Der experimentelle Aufbau und die durchgeführten Messungen sind in Kapitel 11 beschrieben. Die ^{59}Ni Probe war mit ^{6}LiF beschichtet, wobei die Tritonen von ^{6}Li(n,α)^{3}H zur Determinierung des Neutronenflusses verwendet wurde. Der Datenauswertungsprozess von den einfachen Signalen bis zum endgültigen Wechselwirkungsquerschnitt ist in Kapitel 12 angegeben. Der resonante Hintergrund, kommend von Neutronen-Einfangsreaktionen in unterschiedlichen Materialien die im Strahl positioniert waren, wurde zur Kalibration der Konversion von Neutronen-Flugzeit (TOF) zu E_n verwendet. Die Konditionen für die Datenanalyse und die notwendigen Korrekturen, als auch die Unsicherheitsbestimmung des Ergebnisses sind in diesem Kapitel angeführt. Der resultierende ^{59}Ni(n,α)^{56}Fe Wechselwirkungsquerschnitt ist in den Konklusionen dieses Teils, Kapitel 13, mit den vorhandenen Daten der früheren Messungen und den vorhandenen Kern-Datenbanken verglichen.
Das Ergebnis der Messung bei n_TOF liegt zwischen den beiden vergangenen Messungen. Das Resonanzintegral bestätigt mit 6.7% geringer als Harvey und 12.4% höher als Koehler, die Messung von Harvey, die 1976 in Oak Ridge durchgeführt wurde. Zusätzlich wird bestätigt das alle Kern-Datenbanken den Wechselwirkungsquerschnitt bei der Resonanz überschätzen.
Die Ergebnisse der Dissertation sind in kurzer Form im letzten Teil der Arbeit ('Summary and Outlook') zusammengefasst. Der Detektor wurde erfolgreich fuer die Wechselwirkungsquerschnittsmessung eingesetzt und kann in der vorliegenden Form im Energiebereich 1 MeV $\leq E_\alpha \leq 22$ MeV fuer (n,α) Messungen verwendet werden. Der untere Grenzwert ist limitiert durch die Hintergrundsignale von Neutronen-Einfangreaktionen in unterstützenden Materialien. Die α-Spektroskopie ist limitiert zu $E_\alpha = 22$ MeV durch die Dicke der Diamant-Sensoren, $d = 150$ μm. Ein Ausblick auf zukünftigen Entwicklungen und Projekte schliesst die Arbeit ab.

Abstract

A novel detector based on the chemical vapor deposition (CVD) diamond technology has been developed in the framework of this PhD, for the experimental determination of (n,α) cross-sections at the neutron time-of-flight facility n_TOF at CERN. The ^{59}Ni(n,α)^{56}Fe cross-section, which is relevant for astrophysical questions as well as for risk-assessment studies in nuclear technology, has been measured in order to validate the applicability of the detector for such experiments.

The thesis is divided in four parts. In the introductory part the motivation for measuring (n,α) cross-sections, the experimental challenges for such measurements and the reasons for choosing the CVD diamond technology for the detector are given. This is followed by the presentation of the n_TOF facility, an introduction to neutron-induced nuclear reactions and a brief summary of the interaction of particles with matter. The CVD diamond technology and the relevant matters related to electronics are given as well in this first part of the thesis. The second part is dedicated to the design and production of the Diamond Mosaic-Detector (DM-D) and its characterization. The ^{59}Ni(n,α)^{56}Fe cross-section measurement at n_TOF and the data analysis are discussed in detail in the third part of the thesis, before the summary of the thesis and an outlook to possible future developments and applications conclude the thesis in the forth part.

In this work, the Diamond Mosaic-Detector, which consist of eight single-crystal (sCVD) diamond sensors and one 'Diamond on Iridium' (DOI) sensor has proven to be well suited for (n,α) cross-section measurements for 1 MeV $\leq E_\alpha \leq$ 22 MeV. The upper limit is given by the thickness of the sensors, d = 150 μm, while the lower limit is dictated by background induced by neutron capture reactions in in-beam materials.

The cross-section measurement was focussed on the resonance integral of ^{59}Ni(n,α)^{56}Fe at E_n = 203 eV, with the aim of clarifying the discrepancies between the measurements by Harvey 1976 [2] and Koehler 1999 [3]. The results from the measurement of this reaction with the DM-D at n_TOF in 2012 confirm rather the measurement of Harvey, given a resonance integral 6.7% below these data and 12.4% above the results of Koehler. The determined cross-section confirms that the current evaluated nuclear data files overestimate the cross-section at the resonance.

Contents

I Introduction **1**

1 Why measuring (n,α) Reactions? **5**

1.1 Motivation for measuring ^{59}Ni(n,α)^{56}Fe 6

1.1.1 Relevance of ^{59}Ni in Nuclear Astrophysics 6

1.1.2 Relevance of ^{59}Ni in Nuclear Technology 8

1.1.3 Previous Measurements and Evaluated Nuclear Data 9

1.2 Experimental Challenges in (n,α) Cross-Section Measurements 10

1.2.1 Motivation for Diamond as Detector Material 11

2 The n_TOF Facility at CERN **13**

2.1 Layout 13

2.2 Characteristics of the n_TOF Neutron Beam 15

2.3 Principle of the Time-of-Flight Method 19

3 Neutron-induced Nuclear Reactions **23**

3.1 Cross-Section and Reaction Yield 23

3.2 The Q-Value of a Reaction 26

4 Basic Principles of Particle Detection **29**

4.1 Interaction of Charged Particles with Matter 30

4.1.1 Heavy Charged Particles 30

4.1.2 Electrons 34

4.2 Interaction of Photons with Matter 34

4.3 Interaction of Neutrons with Matter 37

5 CVD Diamond Technology **41**

5.1 Carbon and its Allotropes 41

5.2 Diamond Synthesis and Materials 43

5.3 Electronic Properties of Diamond 45

5.4 Signal Creation in Diamond Detectors 47

5.4.1 Electric Field in a Diamond Sensor 47

5.4.2 Induced Current from Ionizing Particles 49

5.4.3 Pulse Shapes in Diamond Detectors 50

6 Electronics 55
6.1 Electronic Time Constant 55
6.2 Current Amplification 56
6.3 Charge Amplification 57
6.4 Noise and Resolution 58
6.5 Calibration of Electronics 62

II The Diamond Mosaic-Detector 65

7 Design and Production 69
7.1 The Diamonds 71
7.2 Metallization of the Diamonds 71
7.3 PCB Design 74
7.4 Mounting 76

8 Characterization of the dedicated Electronics 77

9 Characterization of the DM-D Channels 81
9.1 Current over Voltage Behaviour 82
9.2 Calibration with α Particles 83
9.2.1 Saturation Curve 83
9.2.2 Energy Resolution 84
9.2.3 Charge Yield of the sCVD Diamonds 87

10 Conclusions on the Diamond Mosaic-Detector 91

III Proof of Principle 93

11 ^{59}Ni(n,α)^{56}Fe Measurement at n_TOF in 2012 97
11.1 Experimental Setup at n_TOF 97
11.2 The Sample 98
11.3 Measurements during the ^{59}Ni Campaign at n_TOF 101
11.3.1 Calibration of the DM-D during the ^{59}Ni Campaign 102

12 From Data to Cross-Section 105
12.1 Raw Data and Pulse Shape Analysis 105
12.2 Background of the DM-D in the n_TOF Beam 109
12.3 TOF to E_n Calibration 111
12.4 Analysis Conditions and Efficiency Corrections 113

12.5 Reaction Yield Calculation and resulting Cross-Section 116

13 Conclusions on the Measurement Results **121**

IV Summary and Outlook **123**

A Data from the Diamond Mosaic-Detector **129**

Bibliography **146**

V BIBLIOGRAPHY **147**

Part I

Introduction

The aim of this PhD project has been to introduce a new technology to neutron cross-section measurements, in particular for studying (n,α) reactions. In such an experiment one aims at determining the probability of neutron absorption followed by the emission of an α particle for a given isotope. This can either be measured for a large neutron energy range with the neutron time-of-flight technique, or at a specific neutron energy in a mono-energetic neutron beam, where the latter gives one point on the cross-section graph of the former.

The specific challenges of these experiments are the low expected counting rate and the background conditions in a neutron beam. Chemical vapor deposition (CVD) diamond is known to be specifically radiation hard and hence offers the possibility to be operated directly inside the neutron beam, increasing in this way the detection efficiency because of solid angle coverage. Furthermore, the low atomic number $Z = 6$ of the element Carbon makes diamond nearly transparent to γ radiation, which is a major background in neutron facilities. Hence the CVD diamond technology offers a good solution for such measurements. Spectroscopic grade CVD diamond substrates of reasonable size became available only in recent years and hence the possibility to build a detector based on this technology arose.

A new detector has been developed and the ^{59}Ni(n,α)^{56}Fe cross-section has been measured at the neutron time-of-flight facility n_TOF at CERN in the framework of this thesis. The Diamond Mosaic-Detector is presented in the second part of the thesis, followed by the description, data-analysis and results of the measurement in the third part. This first part gives an introduction to the various fields of physics and technology that are involved in such experiments.

The motivations to measure the ^{59}Ni(n,α)^{56}Fe reaction are given in the first Chapter, followed by the experimental challenges for (n,α) measurements and the motivation to use single-crystal chemical vapor deposition (sCVD) diamond as detector material.

An introduction to the n_TOF facility at CERN is given in Chapter 2 where the principles of a neutron time-of-flight experiment are presented as well.

In Chapter 3 the basic quantities for the description of neutron-induced nuclear reactions, such as the cross-section, are introduced.

The basic mechanisms of particle detection are given in Chapter 4, with special focus on α and γ particles as well as neutrons. To introduce the expected background in a diamond detector, which is operated in a high-energetic neutron beam, the spectrum recorded in a 14 MeV neutron beam are presented and discussed.

Chapter 5 gives an introduction to the CVD diamond technology and the electronic properties of diamond. A derivation of the expected signal shapes in diamond sensors is given, followed by a comparison with experimental results.

The concluding chapter of this introductory part focusses on the electronics that was used for the measurements as well as the introduction of quantities that are relevant to spectroscopic measurements at time-of-flight facilities, such as energy and time resolution.

Chapter 1

Why measuring (n,α) Reactions?

Our knowledge of nuclear structure is primarily based on experiments which are investigating various nuclear reactions. The pioneering experiment by Rutherford, with α particles impinging on a Au foil [4], led to the understanding that the atom consists of a very small but massive nucleus, which is surrounded by light-weight electrons. The field of nuclear physics developed as a consequence to this result.

Further experiments of various kinds have led to the development of different models of the atomic nucleus. The combination of nuclear models with experimental data allow nowadays to generate databases of evaluated nuclear data which are an important input for various calculations or simulations. In particular, the study of neutron-induced nuclear reactions is relevant not only for expanding our knowledge on nuclear physics but also for nuclear technology, nuclear astrophysics and medical physics. In all these fields nuclear data files are inputs needed to further investigate a given problem.

In contrary to neutron scattering and capture reactions, which are possible at all incident neutron energies, the (n,α) reaction is for most isotopes only possible above a given neutron threshold-energy, as the α particle has to overcome the coulomb barrier of the nucleus. Still, in some isotopes this reaction is exothermic and hence does not feature a threshold-energy. Two examples are the ^{10}B(n,α)^{7}Li and ^{6}Li(n,α)^{3}H cross-sections, which are considered as standard over a wide neutron energy range and are hence used in neutron detection technologies. Other (n,α) reactions are by far not as well known and need to be measured experimentally if the data is needed for certain applications. For example, the ^{33}S(n,α)^{30}Si reaction is currently studied for its applicability in neutron capture therapy [5].

In nuclear astrophysics the measurement of (n,α) reactions in A = 100 - 200 nuclei would allow to enhance the reliability of global low-energy α particle-nucleus optical potentials [6], which are strongly energy dependent. These potentials are used in the Hauser Feshbach statistical model [7] to predict reaction-rates, which are needed for the complex calculations to understand the p-process in stellar environments. The p-process is responsible for the formation of 32 proton-rich stable isotopes between ^{74}Se and ^{196}Hg. The astrophysical site where this process happens is still under discussion and there is no model developed yet to explain the solar abundances of all p nuclei within a single scenario. To develop a consistent p-process picture, reliable reaction rates are fundamental and experimental data are important either as direct input to the calculations, or for testing the theoretical predictions of the reaction rates.

The measurement of (n,α) reactions can also be used to determine the reaction rates for the inverse (α,n) reaction, which is more difficult to determine experimentally. This is for instance the case with ^{25}Mg(n,α)^{22}Ne [8]. The inverse reaction ^{22}Ne(α,n)^{25}Mg is the main neutron source in massive stars for the astrophysical s-process and the accurate determination of this cross-section would improve our understanding of the origin of heavy elements.

Also in nuclear technology (n,α) reactions play an important role for security aspects and related material studies, as is the case for the isotope ^{59}Ni.

1.1 Motivation for measuring ^{59}Ni(n,α)^{56}Fe

$^{59}_{28}$Ni is a radioactive isotope of Ni. It disintegrates with a half-life of $t_{1/2} = (76 \pm 5) \cdot 10^3$ years [9] to the ground state of $^{59}_{27}$Co by basically pure e$^-$-capture ($3.7{\cdot}10^{-5}\%$ β^+-decay). The decay radiation is predominantly X-rays of 7 keV, besides Auger e$^-$ of up to 6 keV.

The (n,α) reaction in this isotope of Ni has relevance in nuclear astrophysics for the calculation of the natural abundances of the chemical elements in the universe. In nuclear technology this reaction is related to material embrittlement in structural materials. Although ^{59}Ni is not a constituent of natural Ni, it is created by neutron capture on ^{58}Ni in nuclear reactor environments.

1.1.1 Relevance of ^{59}Ni in Nuclear Astrophysics

The formation of elements with a mass number A $\geq$ 56 is mainly related to neutron capture processes in stars [11]. The neutron densities and the temperature in stellar environments dictate the path that is taken to form these elements and their corresponding isotopes.

One classifies the rapid neutron capture process (r process) in explosive stellar environments, where the neutron density is high. Consecutive neutron capture reactions occur and the reaction path is driven far from the valley of stability on the neutron rich side of the chart of nuclides up to the neutron drip line.

When the neutron density is small, β-decays occur generally faster than the consecutive neutron capture reaction and one classifies the slow neutron capture process (s process), which evolves close to the valley of stability. Where neutron capture is competing with β-decay or alternative nuclear reactions, the s process features branching points [12].

The reaction path of these processes is sketched in Figure 1.1, where one observes that there are certain isotopes which are shielded from the r process due to a stable isobar. These s-only isotopes are indicated in the chart with 's'. Nuclides which can only be synthesized via the r process are marked with 'r'. The abundance distribution, which is displayed in the top left corner, shows peaks which are related to one of the two processes in the region of neutron magic nuclides [10].

Isotopes on the proton rich side of the valley of stability are bypassed by the neutron capture processes. They are formed by photo-disintegration in the p process. Their abundance is in general much smaller than the abundance of nuclides produced in the s and r processes.

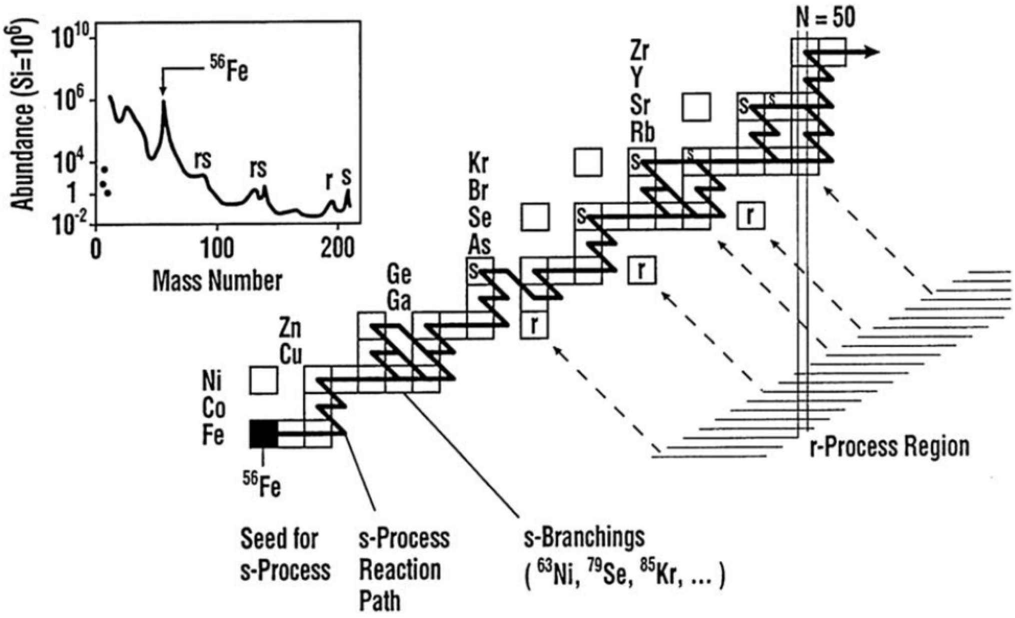
Abundance (Si=10^6)
10^10
10^6
10^4
1
10^-2
0
100
200
Mass Number
56Fe
rs
rs
r s
N = 50
Zr
Y
Sr
Rb
Kr
Br
Se
As
Ge
Ga
Zn
Cu
Ni
Co
Fe
s
r
56Fe
r-Process Region
Seed for
s-Process
s-Process
Reaction
Path
s-Branchings
(63Ni, 79Se, 85Kr, ...)

Figure 1.1: Schematic sketch of the reaction path of the s and r process on the chart of nuclides, picture taken from [10]; s- and r-only isotopes are indicated with the respective letter. The abundance as a function of the mass number is displayed on the top left. The peaks in this distribution are related to the small capture cross-section of neutron magic nuclei.

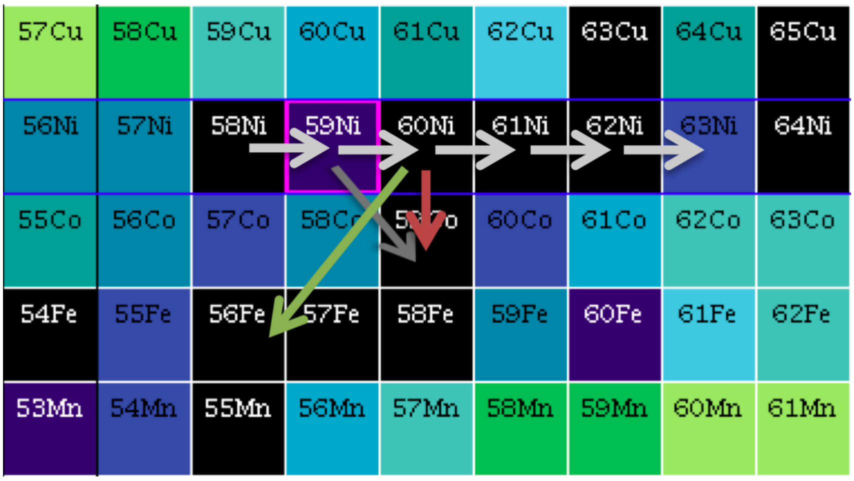

57Cu	58Cu	59Cu	60Cu	61Cu	62Cu	63Cu	64Cu	65Cu
56Ni	57Ni	58Ni	59Ni	60Ni	61Ni	62Ni	63Ni	64Ni
55Co	56Co	57Co	58Co	59Co	60Co	61Co	62Co	63Co
54Fe	55Fe	56Fe	57Fe	58Fe	59Fe	60Fe	61Fe	62Fe
53Mn	54Mn	55Mn	56Mn	57Mn	58Mn	59Mn	60Mn	61Mn

Figure 1.2: Chart of nuclides in the region of Fe and Ni. A neutron capture reaction in the secondary s process seed ^{58}Ni forms ^{59}Ni. At this isotope the capture reaction (light gray arrows) is competing with the (n,α) (green arrow) and (n,p) (red arrow) reaction. The natural decay of the radioactive ^{59}Ni is indicated in dark gray.

The main seed for the s process is ^{56}Fe, as indicated in Figure 1.1, but also ^{58}Ni can be considered as a secondary seed for this process. Therefore, the neutron induced reactions in ^{59}Ni, produced by neutron capture on ^{58}Ni, become important to understand the paths and abundances related to the s process. The isotope ^{59}Ni has the particularity that, unlike most isotopes, the (n,α) and (n,p) reaction channels opened at neutron energies relevant for the astrophysical s process. These processes and the natural radioactive decay of ^{59}Ni compete with neutron capture [13], see the flow diagram of Figure 1.2, and hence make ^{59}Ni a first branching point in the s process. Furthermore the ^{59}Ni(n,α)^{56}Fe reaction has a recycling effect, as it supports the production of the main s process seed nucleus ^{56}Fe and strengthens its role as such.

1.1.2 Relevance of ^{59}Ni in Nuclear Technology

Due to their high strength and corrosion resistance, alloys containing Ni, namely stainless steel, are used for nuclear reactor vessels. Also in other environments with a high neutron fluence [14, 15], this material is used as structural material.
The mechanical and dimensional properties of stainless steel change in high radiation environments due to He production through various (n,α) reactions [16]. The He atoms precipitate in the grain boundaries and form He bubbles which lead to material embrittlement. The risk of irradiation assisted stress corrosion cracking, see Figure 1.3, in the structural materials reduces the lifetime for safe operation of nuclear facilities.
Although ^{59}Ni is not a natural constituent of stainless steel, it is generated via the neutron capture reaction on ^{58}Ni. The two step reaction ^{58}Ni(n,γ)^{59}Ni(n,α)^{56}Fe becomes the major contributor to the He production in structural materials for longer irradiation times. A good knowledge of the corresponding cross-sections is vital for reliable risk assessment studies [17].

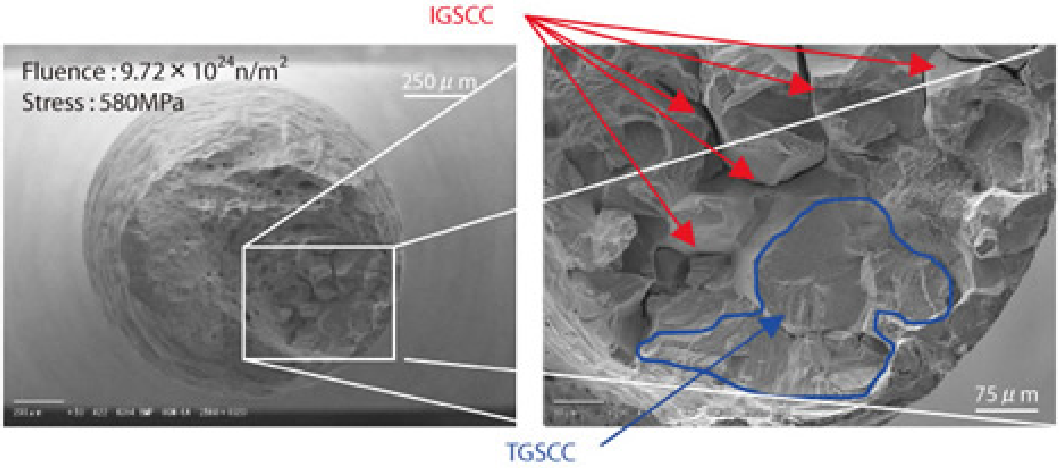

Figure 1.3: Microscopic picture of inter-granular (IGSCC) and trans-granular (TGSCC) stress corrosion cracking, picture from [18].

1.1.3 Previous Measurements and Evaluated Nuclear Data

In the 70ies, various measurements of the ^{59}Ni(n,α)^{56}Fe cross-section have been performed. At thermal energies there are four different measurements available with highly discrepant values. Harvey et al. [19] measured $\sigma = (11.4 \pm 0.8)$ barn at the Oak Ridge e^{-} linear accelerator. McDonald et al. [20] measured, with $\sigma = (22.3 \pm 1.6)$ barn, a value twice as high at the nuclear reactor of the Chalmers University of Technology in Gothenburg, Sweden. Eiland et al. [21] and Werner et al. [22], who have also measured the cross-section at 55.1 meV, lie in between the other two measurements.
Harvey et al. also measured the cross-section for the neutron energy (E$_n$) region 30 eV $\leq$ E$_n$ $\leq$ 23 keV [2]. Koehler and Gledenov [3] repeated the measurement in 1999 at Oak Ridge with the same sample for the neutron energies 0.2 eV $\leq$ E$_n$ $\leq$ 20 keV. The data of this measurement lie systematically below the results published by Harvey et al. The sample that was used for both measurements was also used for the measurements at n_TOF, which will be reported on in the third part of this thesis.

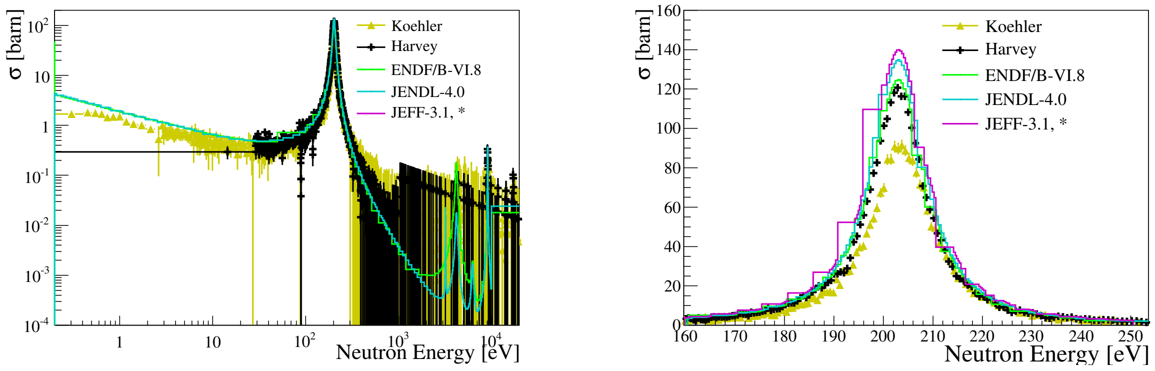

(a) Existing data in the energy region 0.2 eV $\leq E_n \leq 20$ keV.

(b) Existing data at the dominant resonance at $E_n = 203$ eV.

*Figure 1.4: Existing experimental and evaluated data for the ^{59}Ni(n,α)^{56}Fe reaction. The libraries ROSFOND-2010, ENDF/B-VII.1 and ENDF/B-VII.0 are equivalent to JEFF-3.1 *.*

The evaluated nuclear data libraries ROSFOND-2010, JEFF-3.1, ENDF/B-VII.1 and ENDF/B-VII.0 follow the measurement of Eiland at thermal energies. JENDL-4.0 lies in between the data of Harvey and Eiland at these energies. ENDF/B-VI.8 is in agreement, within the experimental error margins, with the measurement of Harvey, et al. at thermal energies and follows the data up to 1 keV. In Figure 1.4 the cross-section for the ^{59}Ni(n,α)^{56}Fe reaction given by the evaluated nuclear data files is plotted in comparison with the measurements by Harvey et al. and Koehler and Gledenov from thermal neutron energies up to 23 keV. The zoom on the dominant resonance at $E_n = 203$ eV shows that most evaluated data files overestimate the strength of the resonance when comparing with the existing measurements. The measurement of Koehler and Gledenov lies about 30% below the measurement of Harvey et al.

1.2 Experimental Challenges in (n,α) Cross-Section Measurements

The cross-section of a nuclear reaction is experimentally determined by comparing the number of incoming neutrons with the number of outgoing reaction products. The α particle, which corresponds to a ^{4}He nucleus, is the particle to be detected when investigating (n,α) reactions. The feasibility of the experiment is at first dependent on the Q-value of the (n,α) reaction in question, which determines the energy of the outgoing α particles.

Due to the high mass, about 4 atomic mass units or 3.7 GeV/c^2, and double elementary charge, α particles are highly ionizing particles. Their range in matter is small, for typical α energies of a few MeV less than 20 μm in diamond, and the energy loss significant when only passing through a thin layer of material. In order to accomplish low α-absorption in the sample and to reduce the energy loss of the α particle on its way to the detector, the sample in use for a (n,α) cross-section measurement needs to be very thin and the measurement should be performed under vacuum, given a certain distance between sample and detector.

The choice of a thin sample reduces the counting rate of the experiment and, in addition, (n,α) reactions often feature small cross-sections. Therefore the neutron facility at which the experiment shall be performed needs to provide sufficient neutron fluence to allow the (n,α) measurement. In addition, the signal-to-background ratio may be a limiting factor for the experiment. Only if signal and background reactions can be distinguished from each other by means of the deposited energy spectrum in the detector or via pulse shape analysis, the signal-to-background ratio will not affect the feasibility of the (n,α) measurement.

In a first approximation and at low neutron energies, the α particle emission in (n,α) reactions can be assumed to be isotropic. At higher neutron energies the reaction kinematics makes the α emission peaked in the forward direction in the laboratory frame. For some reactions, for example the ^{6}Li(n,α)^{3}H reaction, the anisotropy of the reaction has to be taken additionally into consideration for the efficiency of the experimental setup. To maximize the angular coverage and hence the experimental yield and to minimize anisotropy effects, the detector is to be placed in the neutron beam in close proximity to the sample, see Figure 1.5, for cross-section measurements. To maximize the efficiency, the detector should be matched to the size of the sample and the neutron beam profile respectively.

Due to the neutron production processes, at neutron facilities there is an unavoidable in-beam

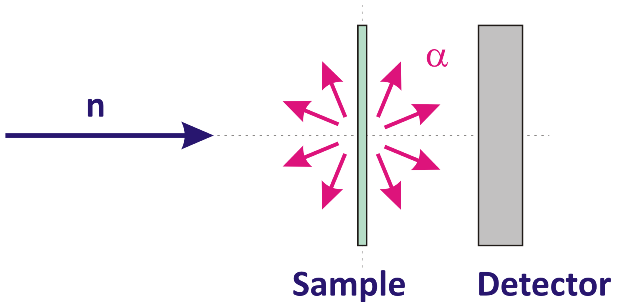

Figure 1.5: Schematic experimental setup for (n,α) cross-section measurements. The neutron beam, together with the in-beam γ-background, impinges on the sample, detector and the surrounding materials.

γ-background, as will be shown in the next chapter for the n_TOF facility at CERN. To reduce the background contribution, the sensitivity of the detector to γ-rays should be minimal. Low-Z materials are hence favorable for the detector and the surrounding materials.

Apart from in-beam γ-rays, neutron-induced nuclear reactions in the surrounding materials and the detector itself need to be considered for the background estimation. In the experiment, the background needs to be carefully determined with dedicated measurements, which calls for a compact detector-design, allowing the exchange of the sample placed in front of the detector.

In order to achieve optimal background identification and subsequent rejection it is advisable to use a high resolution spectroscopic detector. This also allows the identification of different nuclear reactions which can then be measured simultaneously. In the case of ^{59}Ni this is mandatory as both the (n,α) and the (n,p) channels are opened at all neutron energies and the two reactions need to be distinguished from each other. High resolution particle spectroscopy with a compact experimental setup can be best achieved with a solid-state detector, whose thickness is adjusted to the range of the α-particles in the detector.

1.2.1 Motivation for Diamond as Detector Material

Under the above considerations, single-crystal chemical vapor deposition (sCVD) diamond detectors seem to be the optimal solution, compared to other solid-state and gaseous detectors:

- Diamond is a low-capacitance detector material, which does not induce noise at room temperature. Both is favorable for a high-resolution measurement.
- Single-crystal diamond has been proven to be well suited for spectroscopic measurements of charged particles [23, 24].
- The exceptional radiation tolerance of diamond [25, 26] allows the positioning of the detector inside the neutron beam.
- As diamond is made of Carbon, with Z = 6, its sensitivity to γ-radiation is the lowest of all solid state detector materials.
- The inelastic nuclear reaction channels in ^{12}C, which yield high energetic background, open only above a threshold neutron energy of $E_n = 6.2$ MeV. For ^{28}Si, the best alternative as spectroscopic solid-state detector for the above conditions, the threshold lies at 2.8 MeV.
- Diamond is a semi-conducting detector which does not need a p-n junction, like Si or Ge detectors. This is favorable for the measurement in a neutron beam, as some dopants, like B, may induce a high-energetic background.

These arguments have lead to the development of the Diamond Mosaic-Detector for (n,α) cross-section measurements.

Chapter 2

The n_TOF Facility at CERN

The neutron time-of-flight facility n_TOF was proposed by C. Rubbia et al. [27] in 1998 with the aim to provide a facility that allows high-resolution cross-section measurements of neutron-induced nuclear reactions, over a wide neutron energy (E_n) range. The facility was built in 2000-2001 at CERN. The measurements are primarily focused on satisfying the data needs for nuclear astrophysics [28, 29] and nuclear technology [30]. Lately also experiments for medical physics [5] and basic nuclear physics [31] are scheduled. At n_TOF the neutrons are produced by spallation of 20 GeV/c protons incident on a Pb target, where the original Pb target was replaced by a new one in 2008.

By summer 2014, an additional experimental hall will be available at n_TOF [32]. The beam line will be installed vertical above the spallation target and the new experimental area will be situated about 20 m above the target, while the existing measuring station is about 200 m downstream the target, at the end of a horizontal beam line. The new beam line will provide a neutron fluence on average a factor 20 higher in comparison to the existing experimental area and hence the possibility to measure smaller mass samples or smaller cross-sections. This will be advantageous for (n,α) reaction measurements, as they often feature small cross-sections. The combination of a short flight path and high instantaneous neutron fluence will in addition be advantageous for measurements on short-lived radioactive isotopes.

This chapter aims at introducing the n_TOF facility along with the principle of time-of-flight measurements. The results given herein can be found in full detail in Reference [33].

2.1 Layout

The schematic layout of the n_TOF facility at CERN is illustrated in Figure 2.1. The n_TOF facility receives a pulsed proton beam, with an average repetition rate of 0.4 Hz, from the CERN Proton Synchrotron (CERN-PS). The protons impinge on the lead target with a momentum of 20 GeV/c. The nominal proton pulse has an intensity of $7{\cdot}10^{12}$ protons on target (pot) and a width of 7 ns root mean square (rms).

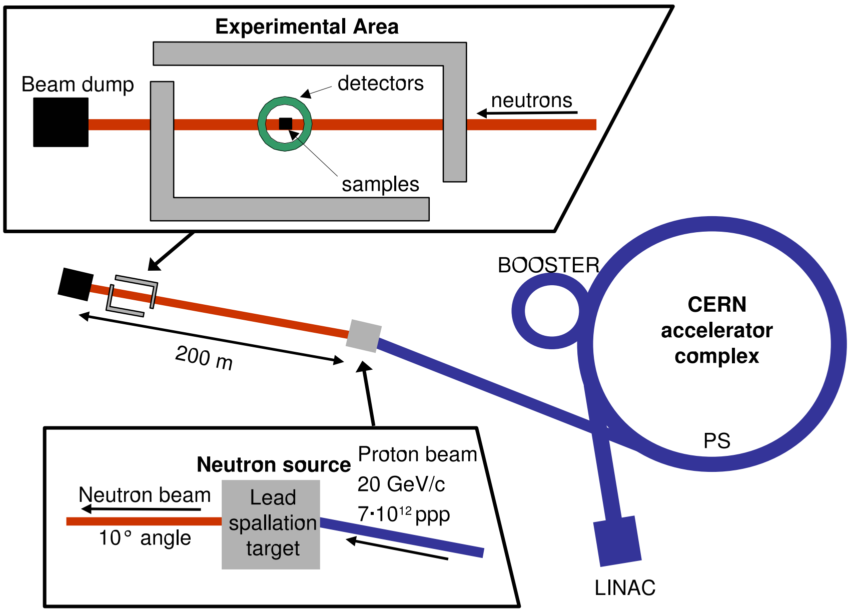

Figure 2.1: Schematic layout of the n_TOF facility at CERN, picture from [33]. The pulsed proton beam, which is delivered by the CERN Proton Synchrotron (PS) impinges on the Pb spallation target. The experimental hall is situated about 200 m behind the target at the end of the horizontal beam line.

Lead was chosen as material for the spallation target as it has a very high neutron yield of about 600 neutrons per proton at 20 GeV/c and a high transparency for neutrons with energies below MeV, which is favorable for the resulting neutron energy resolution. The Pb target is surrounded by a 1 cm thick cooling-water layer. An additional 4 cm moderator layer, which can be either deionized water or borated water, is present in the front face of the target. The aim of the moderator layer is to reduce the energy of the neutrons in the beam via elastic colisions, transforming the initially fast (MeV-GeV) neutron spectrum into a white spectrum that ranges from thermal (25 meV) up to 20 GeV.
The impinging proton beam (primary beam) has a horizontal angle of 10° to the existing neutron beam line. This is to avoid the forward peaked charged particle shower, coming from the spallation process, in the neutron beam (secondary beam).
The experimental area (EAR1), where the measurements take place, is situated about 182 m downstream the spallation target, see Figure 2.2. Two collimators are installed in the neutron beam line, to shape the neutron beam. The inner diameter of the second collimator is adjustable, either 1.8 cm for neutron capture measurements or 8 cm for fission measurements. A sweeping magnet is installed in the beam line to deflect all charged particles from the beam. A multi-filter station is installed before the first collimator to absorb neutrons of a given energy, if needed. There is a significant amount of shielding around the beam line to absorb negative muons, which were responsible for a strong neutron background in the experimental area at the beginning of the facility's operation. The beam dump is situated 10 m downstream from the experimental area in a separate room, see also Figure 2.1, which is beneficial for the background situation for

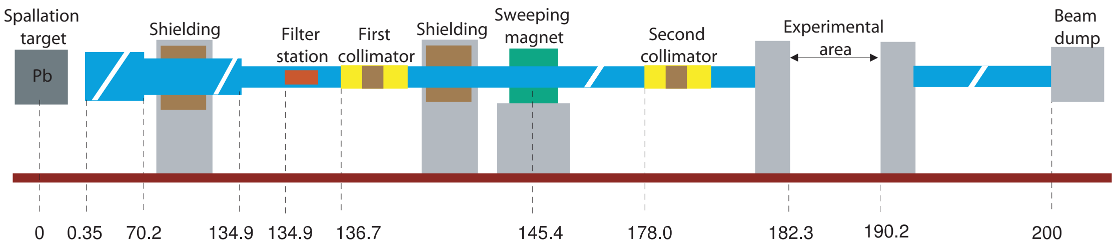

Figure 2.2: Schematic beam line of the n_TOF facility at CERN, picture from [33].

the experiments.

2.2 Characteristics of the n_TOF Neutron Beam

Neutron and Photon Fluence Besides neutrons and charged particles, there is a significant amount of photons produced during the spallation and the consecutive neutron moderation process in the target and the surrounding moderator. The spallation-photons, or prompt photons, are the first particles to arrive at the experimental area. This intense photon burst is registered as the so-called 'γ-flash' by the detectors and can blind the system in use, especially big-volume detectors containing high Z materials, for a significant amount of time. This affects the high neutron-energy limit for any given experiment at n_TOF. The delayed photons, also called 'in-beam γ', are related to the moderation process of the neutrons and neutron capture reactions in various materials. These photons have to be considered in background estimations for the experiments, especially for 1 keV $\leq E_n \leq$ 1 MeV.

The particle fluence for neutrons and photons in the experimental area as a function of time-of-flight (TOF) is illustrated in Figure 2.3 for both moderator configurations (deionized and borated water). The corresponding E_n, see Section 2.3, is indicated at the neutron spectra with arrows. When borated water is used as moderator, more low-energy neutrons are absorbed in the moderator (because of the high absorption cross section of ^{10}B) and there are less in-beam γ-rays with $E_\gamma \geq 1$ MeV arriving at the measuring station (x1/10).

In Figure 2.4 the energy spectra of the photons arriving at the experimental area are shown for both moderator configurations. The prompt γ-spectrum is independent of the moderator type, as these photons are related to the spallation process and not to the moderation. In contrary, the in-beam γ-spectrum differs significantly, depending on the moderator. The main contribution to the γ-spectrum, when H_2O is used as moderator, are 2.2 MeV photons, coming from the neutron capture reaction ^{1}H(n,γ). When ^{10}B is added to the moderator, this reaction becomes less important as the ^{10}B(n,α)^{7}Li cross-section is about four orders of magnitude higher. The latter reaction yields in 94% photons of E_γ = 478 keV, corresponding to ^{10}B(n,α)^{7}Li*, where the residual nucleus is left in the first excited state. The peaks at 7.7 MeV and 511 keV correspond to ^{27}Al(n,γ) and pair annihilation, respectively.

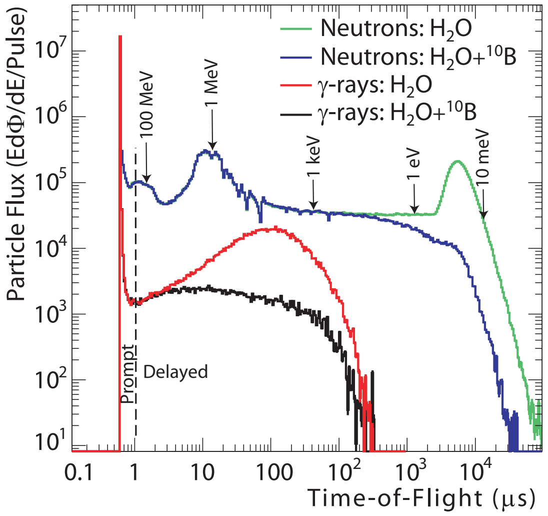

Figure 2.3: Simulated particle spectra at n_TOF for water and borated water as neutron moderator respectively, picture from [33]. The in-beam γ-ray background ($E_\gamma \geq$ 1 MeV) is reduced by more than one order of magnitude, when borated water is used.

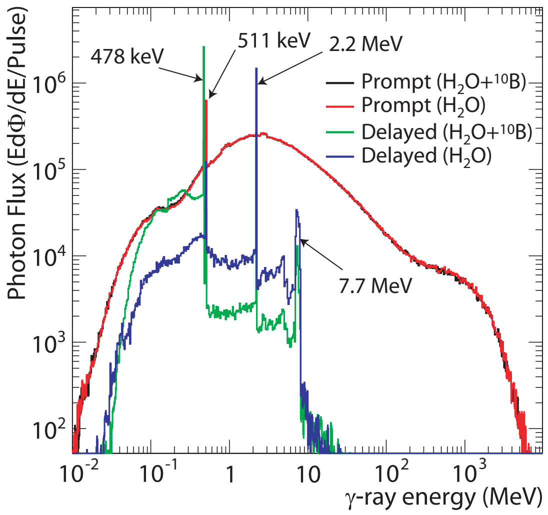

Figure 2.4: Simulated photon energy spectra at n_TOF with water and borated water as neutron moderator, picture from [33]. The main contribution of the delayed γ when borated water is used, comes from the $^{10}B(n,\alpha)^7Li^*$ reaction.

E_n	Neutrons/pulse
10-100meV	$1.5 \cdot 10^4$
0.1-1 eV	$1.3 \cdot 10^4$
1-10 eV	$2.0 \cdot 10^4$
10-100 eV	$2.5 \cdot 10^4$
0.1-1 keV	$2.9 \cdot 10^4$
1-10 keV	$3.2 \cdot 10^4$
10-100 keV	$4.4 \cdot 10^4$
0.1-1MeV	$1.3 \cdot 10^5$
1-10MeV	$1.5 \cdot 10^5$
10-100MeV	$5.0 \cdot 10^4$
0.1-1 GeV	$4.7 \cdot 10^4$
Total	$5.5 \cdot 10^5$

Table 2.1: Number of neutrons per $7 \cdot 10^{12}$ pot in different neutron energy (E_n) ranges for the capture collimator (18 mm diameter) and borated water as neutron moderator.

The spectra shown in Figures 2.3 and 2.4 result from detailed Monte Carlo simulations. Although qualitatively reliable, these simulations can not provide accurate enough information about the neutron fluence, which is essential for the high-accuracy cross-section measurements

performed at this facility. The neutron fluence at n_TOF has been determined accurately by means of various different measurements and cross-checking these results with Monte Carlo simulations [33, 34].
The integrated neutron fluence for a nominal pulse intensity of 7·10^{12} pot and borated water as neutron moderator, which was the setup during the ^{59}Ni(n,α)^{56}Fe measurement described in the third section of this thesis, is 5.5·10^5 neutrons per pulse. In Table 2.1 the evaluated neutron fluence for different energy intervals is listed for the capture collimator and borated water as neutron moderator. The neutron fluence spectrum at n_TOF for both borated and deionized water as neutron moderator and the capture collimator is illustrated in Figure 2.5. The statistical and systematic uncertainties are given in the bottom panel.

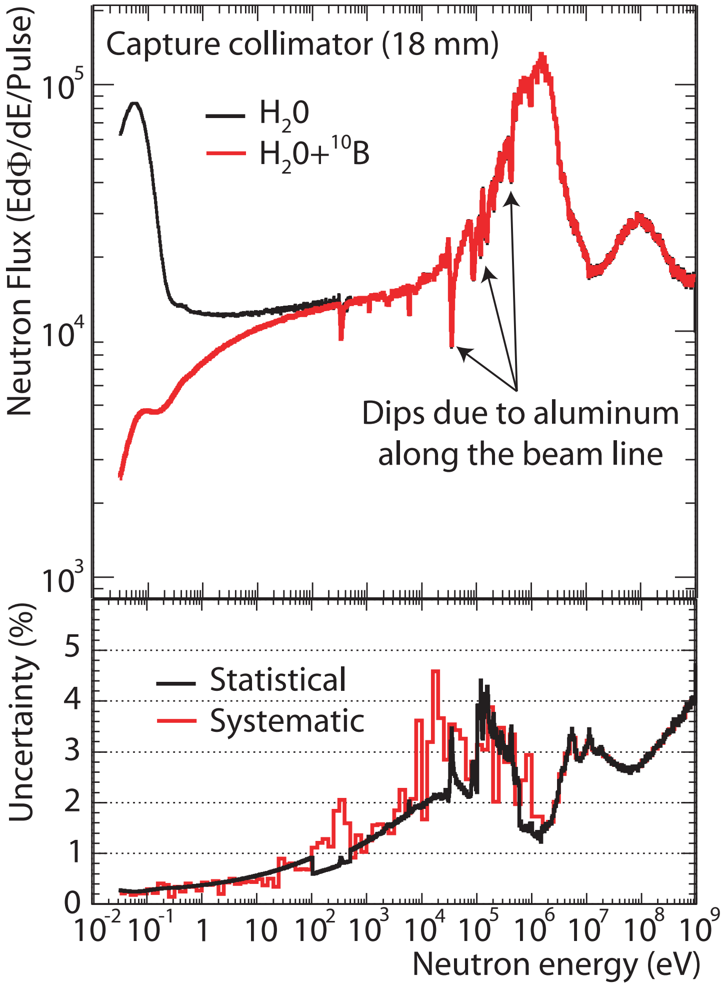

Figure 2.5: Evaluated n_TOF neutron flux in the configuration with the capture collimator (18 mm diameter) with water and borated water as moderator. The systematic and statistical uncertainties are given in the bottom panel, see Reference [33] for details.

Neutron Energy Resolution Neutron cross-sections have in general a pronounced resonance structure. The accuracy with which a cross-section, the corresponding resonances and their shape can be measured at a TOF facility is dependent on multiple factors, only one of them being the time resolution of the detection system. The overall neutron energy resolution ($\delta E/E$) of a TOF facility, which affects the shape of the observed resonances, results from a combination of the moderation process in the target and surrounding materials, the time width of the impinging primary beam (protons at n_TOF) and the distance between experimental hall and target. A full Monte Carlo simulation is needed to estimate the effect coming from the neutron moderation [35]. The full width at half maximum (FWHM) of the simulated neutron energy distributions as a function of TOF is used to define the resolution-function of the facility. The thermal motion of the sample-nuclei leads in addition to a 'Doppler broadening' of the resonances.
In order to illustrate the situation for a specific measurement, the components (FWHM) contributing to the observed resonance width for a measurement of the ^{232}Th(n,γ) cross-section at n_TOF [36] are displayed in Figure 2.6. The Doppler broadening of the resonances is the dominant factor for $E_n \leq 3$ keV. Above this energy, the resolution is primarily dominated by the moderation process in the n_TOF target and surrounding moderator. For neutron energies where the resonance spacing is above the resulting $\delta E/E$, the resonances are observable in the measurement. The intrinsic resonance widths Γ of ^{232}Th(n,γ) are displayed as given by the JEFF-3.1. library.

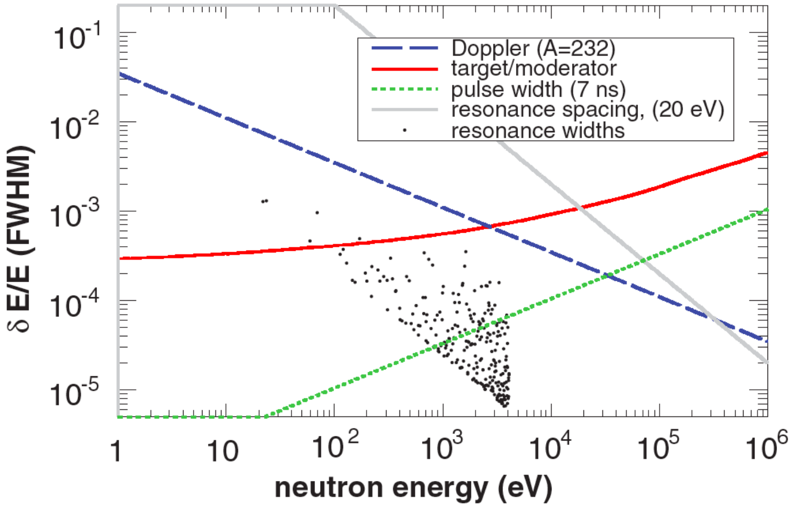

Figure 2.6: Different components contributing to observed resonance widths at n_TOF, picture from [36]. Below 3 keV, the Doppler broadening of resonances is dominating. Above this energy, the moderation process in the target and in the surrounding moderator has the biggest influence on the shape of the observed resonances. The proton pulse width starts dominating at even higher E_n. The resonance spacing and intrinsic resonance widths are given for ^{232}Th(n,γ).

Spatial Beam Profile The neutron beam profile at the experimental station at n_TOF has a Gaussian shape, which changes slightly for different E_n and widens with increasing distance to the collimator. For measurements with the capture collimator $\sigma \approx 7$ mm at the measuring position of the Diamond Mosaic-Detector.
Given a good alignment, the integrated neutron fluence can be used for samples bigger than the neutron beam itself. The beam interception factor (BIF) has to be estimated for smaller samples. If it is feasible, a parallel measurement of the neutron fluence, with the same experimental setup as for the cross-section measurement, is the most reliable method. This was the case for the ^{59}Ni(n,α)^{56}Fe measurement described in the third section of this thesis, where the ^{6}Li(n,α)^{3}H reaction was used, who's cross-section is considered standard up to $E_n = 1$ MeV [37].

2.3 Principle of the Time-of-Flight Method

In a Time-of-Flight (TOF) experiment, the kinetic energy of the neutrons E_n is determined by their arrival time at the measuring station. The determination of the TOF at n_TOF and the consecutive conversion into E_n is described in the following.

Determination of TOF The data acquisition system (DAQ) of the n_TOF facility [38] is triggered shortly before a proton pulse impinges on the spallation target. The DAQ starts recording at this time, t_{PS}, for the time window available by the data-storage buffer. To reduce the amount of stored data, a constant threshold trigger is normally used in the DAQ and a time stamp is saved with each set of raw data.
The time of particle creation t_0 can not be measured and thus has to be determined relative to other times. It is related to the moment when the protons impinge on the target. The spallation γ then travel for the time $\frac{L}{c}$, with the geometrical flight path L and the speed of light c, to the experimental area, where they are registered by the detection system at the time t_γ as the

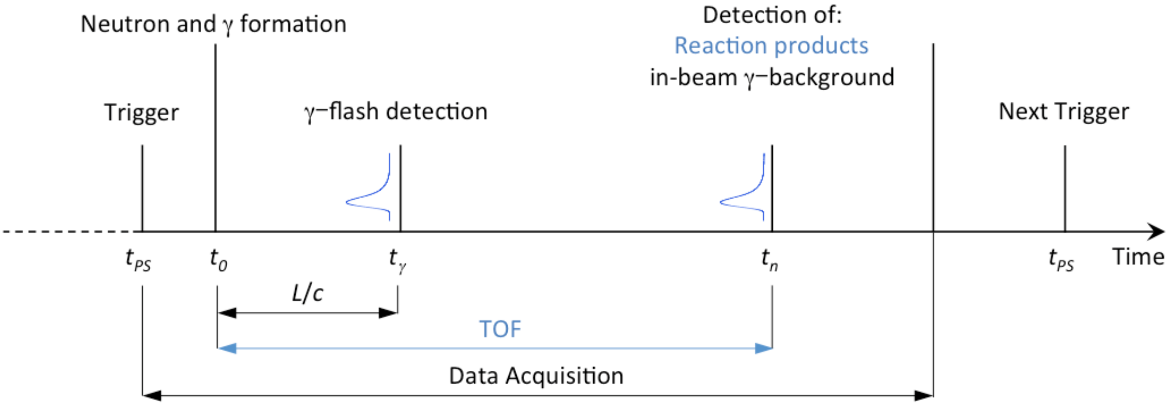

Figure 2.7: Time-of-flight measurement principle.

'γ-flash'. All signals which are registered by the detector at later times t_n are generally related to either neutron induced reactions or in-beam γ.
There is a certain delay between the creation of the neutrons and the time when the neutrons leave the target. A constant time correction factor t_{offset} can be given for this effect cause by the moderation of the neutrons. Lorusso et al. [39] determined t_{offset} = -73 ns for n_TOF. Taking this into account, the TOF can be calculated with the following relation:

$$TOF \;=\; t_n - t_\gamma + \frac{L}{c} + t_{offset}. \tag{2.1}$$

In Figure 2.7 the TOF determination is illustrated schematically. The precision of the TOF measurement is limited by the time resolution Δt of the detector, which is dependent on the signal amplitude. Effects coming from the spallation and moderation as well as from the longitudinal profile of the proton beam are considered via the resolution function. In general, only at short TOF and hence high E$_n$, the timing properties of the electronics influence considerable the final neutron energy resolution ΔE_n. The maximum detection rate of the experimental setup is limited by the double pulse resolution of the electronics.

Determination of the n_TOF γ-flash The effect of the γ-flash was recorded with a 500 μm thick sCVD diamond detector operated with a 2 GHz current amplifier at a test beam in 2010 for the first time [40]. Figure 2.8 shows multiple γ-flash signals and the corresponding average signal. The parabolic fit to the average signal has a FWHM = 16 ns and 6.8 ns rms respectively.

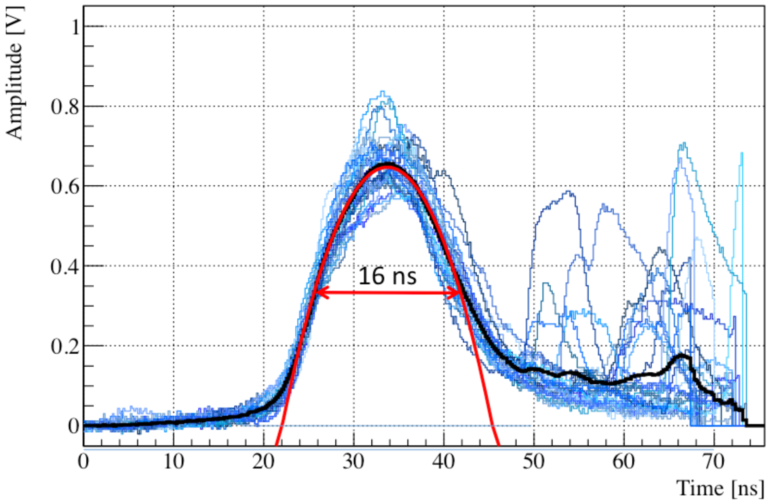

Figure 2.8: Multiple γ-flash signals recorded during a test beam at n_TOF in 2010 with a sCVD diamond detector in combination with a 2 GHz current amplifier. The parabolic fit shows a FWHM of 16 ns, corresponding to 6.8 ns rms from the primary proton beam. Signals on the right hand side correspond to signals created by high energetic neutrons.

This corresponds precisely to the longitudinal beam dimensions of the PS proton beam at the n_TOF target [41]. The signals after the γ-flash correspond to reactions induced by high-energetic neutrons.
This measurement was the first experimental determination of the 'footprint' of the primary proton beam at the experimental area at n_TOF.

TOF Conversion in E$_n$ The conversion from TOF to E_n is derived from the relativistic expression for the total energy $E = E_n + m_n c^2$, where E_n is the kinetic energy of the neutron and $m_n c^2$ the rest mass energy. For $E_n <$ MeV, the classical expression for the kinetic energy, which corresponds to the first term of the Taylor series expansion, can be used.

$$E_n(eV) = m_n c^2 \left(\frac{1}{\sqrt{1-\beta^2}} - 1 \right) \tag{2.2}$$

$$\approx \left(\alpha \frac{L}{t} \right)^2 = \left(72.298 \cdot \frac{L(m)}{TOF(\mu s)} \right)^2 \quad \text{for } E_n < \text{MeV} \tag{2.3}$$

Calculating the error ΔE_n for the classical approximation, by summing the squares of the errors for L and TOF, and dividing the expression by E_n gives the energy resolution of a given TOF facility

$$\frac{\Delta E}{E} = 2 \cdot \sqrt{\left(\frac{\Delta L}{L} \right)^2 + \left(\frac{\Delta TOF}{TOF} \right)^2}. \tag{2.4}$$

In Figure 2.6 the relative energy resolution $\frac{\Delta E}{E}$ for n_TOF is plotted in red.

TOF to E_n calibration The geometrical flight path L for each experiment is determined at n_TOF by means of surveyance measurements. In order to reduce the systematic error, the resonances of known nuclear reactions can be used as additional determination of L.
One compares the recorded TOF of a set of known resonances with the corresponding E_n. Equation 2.3 is then used to fit these data, which gives the flight path L to be used for the TOF to E_n conversion. The L-calibration for the ^{59}Ni(n,α)^{56}Fe measurement with the Diamond Mosaic-Detector at n_TOF will be shown in the third part of the thesis, see Section 12.3.

Chapter 3

Neutron-induced Nuclear Reactions

There is a variety of nuclear reactions which can occur when neutrons interact with atomic nuclei. The neutron-induced reactions can be classified in direct nuclear reactions and in reactions that form a compound nucleus, with the Q-value giving information about whether the reaction is exothermic or endothermic and the cross-section giving information on the probability of the concerned reaction to take place. In the following sections, the basic principles to understand neutron-induced nuclear reactions are described and the needed quantities for cross-section measurements are introduced.

3.1 Cross-Section and Reaction Yield

The interaction cross-section σ is used to quantify the probability of neutron-induced nuclear reactions. Let a neutron beam hit a thin layer of a given isotope. The reaction rate R [1/s] is proportional to the intensity of the neutron beam I [neutrons/cm^2/s] and the number of target nuclei N

$$R \;=\; I \cdot N \cdot \sigma, \tag{3.1}$$

under the assumption that the neutron beam passes the layer practically unattenuated [42]. The proportionality constant σ is known as the cross-section and has the dimension of an area, usually given in barn (1 barn = 10^{-24} cm^2).
There is a large variety of neutron-induced nuclear reactions which can occur. For each of these reactions a partial cross-section σ_i can be defined, the sum of all σ_i giving the total cross-section σ_{tot}

$$\sigma_{tot} \;=\; \sum_i \sigma_i \;=\; \sigma_{el} + \sigma_\gamma + \sigma_{inel} + \sigma_f + \sigma_\alpha + ..., \tag{3.2}$$

where the subscript of the partial cross-sections indicate the corresponding reactions (in the listed order: elastic scattering, radiative neutron capture, inelastic scattering, neutron-induced fission and neutron capture followed by the emission of an α particle).

If nuclei were solid spheres and neutrons classical point like particles, σ would be the geometrical cross-section of the nucleus. The probability for scattering of the neutron on the nucleus would be constant at all E_n. As neutrons and nuclei are quantum-mechanical particles, the cross-sections of neutron-induced nuclear reactions vary strongly with the energy of the incoming neutron $\sigma = \sigma(E_n)$ and depend on the nuclear structure of the given isotope.
At low neutron energies, σ is proportional to $1/\sqrt{E_n}$ and hence related to the time that the neutron spends in the vicinity of the target nucleus. At intermediate energies, where potential scattering is dominant, the cross-section is constant. Here the scattering can be assumed to be similar to hard sphere scattering of the neutron on the nucleus, like in classical mechanics.
When the neutron energy becomes close to quasi-stationary levels of the compound nucleus the cross-section drastically changes and resonances are observed in the cross-section. This was first discussed by Niels Bohr [43] for fission reactions. The compound nucleus theory assumes that neutron-induced reactions are two-step processes. In a first step the target nucleus and the neutron form an excited compound nucleus, which decays in a second step into one of the open reaction channels. The correspondence of the resonances to the nuclear levels of the compound nucleus is schematically illustrated in Figure 3.1.

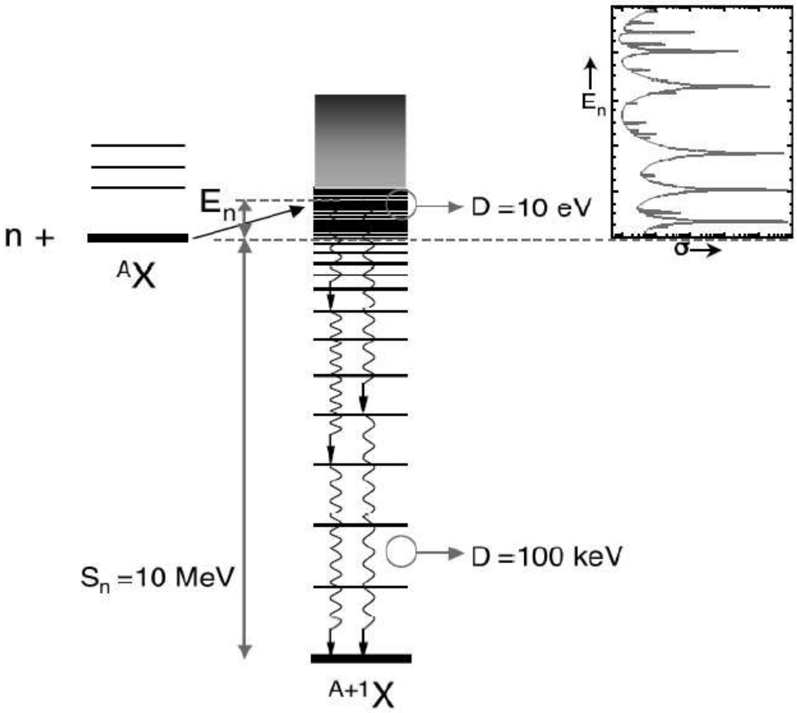

Figure 3.1: Schematic view of the formation of a compound nucleus ^{A+1}X followed by the emission of a γ ray, corresponding to radiative neutron capture, from [44]. Typical values of the average level spacing (D) at different excitation energies are given as well as the neutron separation energy S_n.

The resonances are characterized by the width Γ, the energy, spin and parity. The total width Γ is related to the life-time of the level via the relation

$$\tau = \frac{\hbar}{\Gamma}, \tag{3.3}$$

which follows from Heisenbergs uncertainty principle $\Delta E \Delta t \geq \hbar$ [45]. The shape of the resonances is well described by a Breit-Wigner form [46], which is determined by the resonance energy E_0 and a set of partial widths Γ_i, each related to the decay probability of the compound nucleus into the different exit channels (Γ_n, Γ_γ, Γ_α, etc.).

For neutron energies where the separation of the compound nucleus levels is bigger than the intrinsic width of the resonances, the resonances can be distinguished, which is called the resolved resonance region (RRR). As the energy increases, in the unresolved resonance region (URR), resonances start to overlap and resonant structures cannot be observed anymore. Finally threshold channels open up and contribute to the total cross-section.

In Figure 3.2 the total cross-section for various isotopes can be seen. The data is taken from evaluated nuclear data files (ENDF) from the library JEFF-3.1. The different regions of the cross-section are best distinguishable for the nuclides ^{56}Fe and ^{235}U.

Cross-sections are measured by experimentally determining the reaction yield $Y(E_n)$. This quantity gives the fraction of the beam that undergoes a specific nuclear reaction. It is calculated via the relation

$$Y(E_n) = \left(1 - e^{-n\sigma_{tot}(E_n)}\right) \frac{\sigma_x(E_n)}{\sigma_{tot}(E_n)}, \tag{3.4}$$

with the surface density n of the sample and σ_x the cross-section of interest. In the experiment, the number of outgoing reaction products $C(E_n)$ is measured. With the neutron fluence at

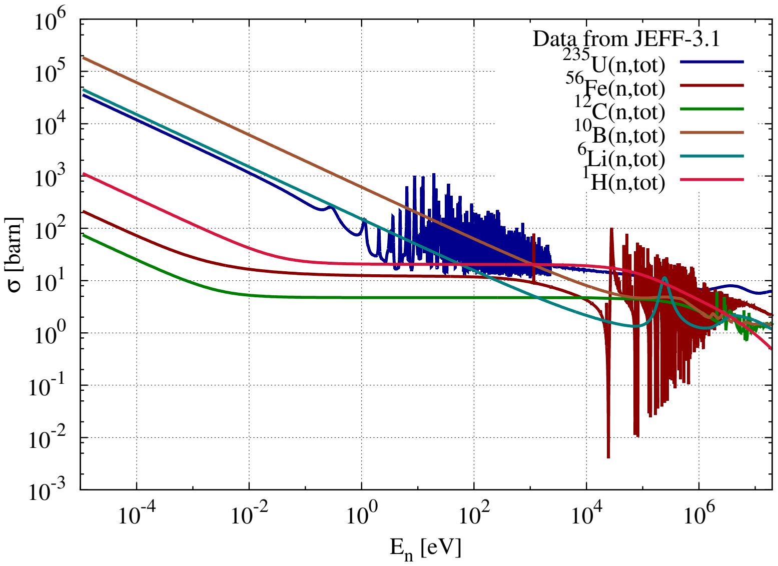

Figure 3.2: Total cross-sections for various isotopes. σ is proportional to $1/\sqrt{E_n}$ at low neutron energies for all isotopes. For ^1H, ^{12}C and ^{56}Fe the elastic scattering is the dominant reaction at intermediate energies, where σ is constant. The resolved resonance region can be seen for ^{56}Fe and ^{235}U.

the experiment $\Phi(E_n)$, the efficiency for detecting the reaction of interest ε and the recorded background $B(E_n)$, the reaction yield is determined in the following way:

$$Y(E_n) \;=\; \frac{C(E_n) - B(E_n)}{\Phi(E_n)\varepsilon}. \tag{3.5}$$

When very thin targets are used the limes $n\sigma_{tot} \rightarrow 0$ in Equation 3.4 is considered. In this so-called thin target approximation, the reaction yield becomes directly proportional to the cross-section:

$$Y(E_n) \;=\; n\sigma_x(E_n) \;=\; \frac{C(E_n) - B(E_n)}{\Phi(E_n)\varepsilon}. \tag{3.6}$$

3.2 The Q-Value of a Reaction

The binding energy $B(A, Z)$ of a given nucleus with mass number A and atomic number Z is defined as

$$B(A, Z) \;=\; [ZM_p + NM_n - M(A, Z)]c^2. \tag{3.7}$$

Here $M_p = 938.272$ MeV is the mass of the proton, $M_n = 939.565$ MeV the mass of the neutron and $M(A, Z)$ the mass of the nucleus. The sum of the masses of the constituents is always greater than the mass of the bound nucleus. The work required to separate the nucleus into the individual nucleons is $B(A, Z)$, which can also be referred to as nuclear mass defect.

The binding energy per nucleon as a function of the atomic mass number can be seen in Figure 3.3. The distribution implies that energy will be released when light nuclei are combined to form heavier ones (fusion) or when heavy nuclei are split into lighter ones (fission). The most tightly bound nuclei are ^{62}Ni, ^{58}Ni and ^{56}Ni with 8.8 MeV binding energy per nucleon [47].

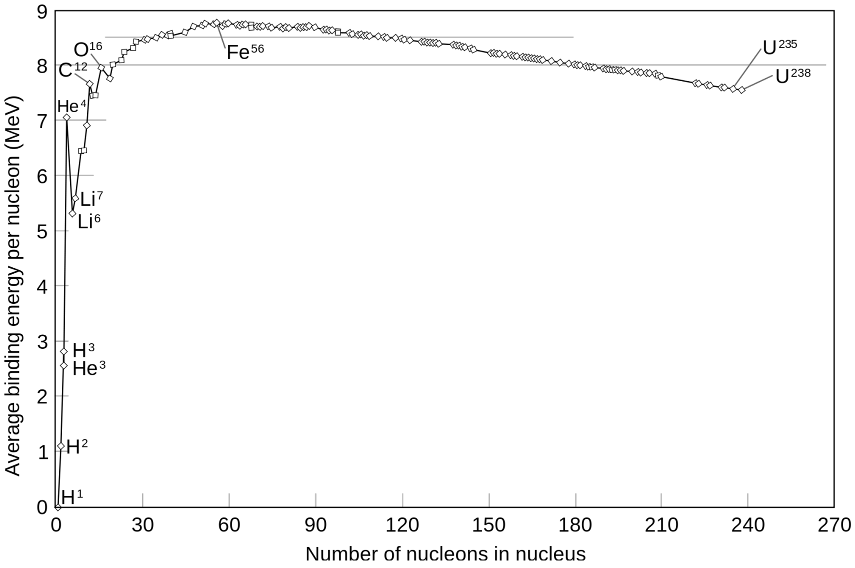

Figure 3.3: Binding Energy per nucleon as a function of the atomic mass number A. Elements near Fe have the highest nuclear binding energy.

In nuclear reactions, where the initial state consists of an incident particle x and the target nucleus X and the final state is composed of the ejectile y and a residual nucleus Y, the concept of the binding energy is applicable as well. Such a reaction X(x,y)Y can be written in the form

$$x + X \ \rightarrow \ y + Y + Q \tag{3.8}$$

where Q is the 'Q-value of the reaction'. Its magnitude is calculated by subtracting the sum of the masses of the reactants from the sum of the masses of the reaction products. Q is positive for exothermic reactions, where energy is released, and negative for endothermic reactions, where a certain amount of energy, called the threshold, has to be supplied.
At the collision of x with X, the compound nucleus C that is formed aquires kinetic energy. From the conservation of energy and momentum follows

$$E_{kin,C} \ = \ E_{kin,x}\frac{M_x}{(M_x + M_X)} \ \approx \ E_{kin,x}\frac{A_x}{A_C}, \tag{3.9}$$

where A$_x$ and A$_C$ are the mass numbers of the incident particle and the compound nucleus respectively. The kinetic energy of the projectile E$_{kin,x}$ must exceed the kinetic energy of the compound nucleus E$_{kin,C}$ by the value of Q, so that the reaction can take place.

$$E_{kin,x} \ = \ E_{kin,C} - Q \tag{3.10}$$

This gives a threshold energy E_{th} of

$$E_{th} \ = \ -Q\frac{M_x + M_X}{M_X} \ \approx \ -Q\frac{A_C}{A_X}. \tag{3.11}$$

A typical threshold reaction is neutron-induced fission in ^{238}U. At low neutron energies this

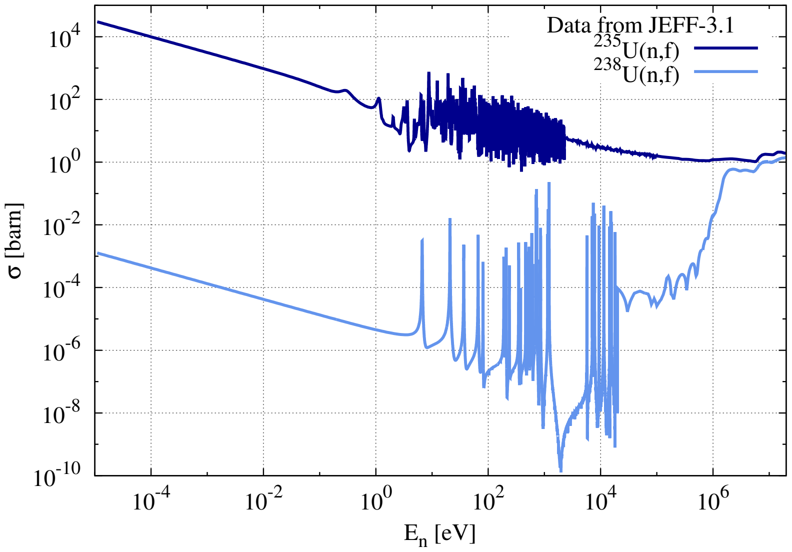

Figure 3.4: Fission cross-sections for ^{235}U and ^{238}U from the evaluated nuclear data library JEFF-3.1.

reaction is strongly suppressed as the binding energy released after capturing a thermal neutron is below the critical energy for fission $E_{th} \approx 1$ MeV. The cross-section of this reaction is shown in Figure 3.4 together with the fission cross-section of ^{235}U. Comparing the order of magnitude of the two reactions it is evident that nuclear fuel in thermal reactors has to be enriched in ^{235}U. In addition, the neutrons released after neutron-induced fission of ^{238}U cannot sustain a chain reaction in thermal reactors as their energy is typically smaller than the energy of the incoming neutron and hence below 1 MeV, the threshold for fission in this isotope.

Chapter 4

Basic Principles of Particle Detection

The possibility to detect an incident particle of any sort is directly related to the mechanisms that govern the particle interaction with the matter that the detector is made of. One can classify particles in charged and uncharged particles. The former underly the Coulomb interaction and hence continuously interact with the electrons present in any medium through which they pass. This does not yet give any information on how strong the interaction will be and whether the incident charged particle is detectable or not. The deposited energy in the detector must exceed the measurement threshold, which is typically governed by the electronic chain as discussed in Chapter 6, in order for the charged particle to be detectable. Furthermore, the full deposition of the particles energy within the volume of the detector is a prerequisite for spectroscopic measurements. By applying an electric field to the detector, the free charged particles drift to the corresponding electrode, inducing a current in the electronic chain which then serves as the signal for the detection of the charged particle. This drift of free charge carriers is the fundamental principle of particle detection in diamond detectors. This also applies to the detection of photons and neutrons, where the reaction products finally ionize the diamond sensor.

In the case of uncharged particles, such as neutrons and photons, the interaction probability is expressed in terms of cross-section, as introduced in Chapter 3 for neutrons. For photons this probability depends on the atomic number Z of the material and, dependent on the energy of the incident photon, the interaction will take place either with the electrons or the nucleus of the atom. The transfer of all or part of their energy to the electrons within the detector medium generally serves as basis for photon detection.

Neutrons predominantly interact with nuclei. For neutrons the probability of interaction depends on the nuclear structure of the specific isotope and differs for each nuclear reaction significantly. The interaction probability varies typically strongly with the energy of the incident neutron E_n. The reaction products of neutron interactions with matter are typically heavy charged particles or photons, which then serve as basis for the detection of the neutron.

In the following the interactions of charged particles, photons and neutrons with matter are shortly described with some focus on diamond detectors and comments on the spectroscopy of the concerned particles are given at each section.

4.1 Interaction of Charged Particles with Matter

The interaction of charged particles with matter is dominated by the coulomb forces between the orbital electrons of the atoms and the charge of the incident particle. Typically, the path of a heavy charged particle, i.e. particles with the mass of one atomic mass unit or more, tends to be a straight line, as any one encounter does not deflect it strongly due to the big difference in mass compared to orbital electrons. This results in a definite range R of heavy charged particles in a given matter. For electrons R is less definite and their path in the absorbing material is much more tortuous than for heavy charged particles.

4.1.1 Heavy Charged Particles

The mean energy loss, also called stopping power, of a heavy charged particle, such as α particles, of intermediate energies in a given material is well described by the Bethe-Bloch equation [48], including low energy corrections:

$$-\left\langle \frac{dE}{dx} \right\rangle = K z_e^2 \frac{Z}{A} \frac{1}{\beta^2} \left[\frac{1}{2} \ln \frac{2 m_e c^2 \beta^2 T_{max}}{I^2 (1-\beta^2)} - \beta^2 - \frac{\delta(\beta\gamma)}{2} - \underbrace{\frac{C}{Z} + z^2 L_2(\beta) + z L_1(\beta)}_{\text{low energy corrections}} \right] \tag{4.1}$$

The constant $K = 4\pi N_A r_e^2 m_e c^2$ is a product of Avogadro's number N_A, the classical electron radius r_e, the mass of the electron m_e and the speed of light c. The charge of the incident particle is z_e and its velocity is represented in $\beta = \frac{v}{c}$ and $\gamma = \frac{1}{\sqrt{1-\beta^2}}$. The properties of the matter under consideration are represented by the atomic number Z and the atomic mass A of the material as well as by the mean excitation energy of the absorber I. T_{max} is the maximum kinetic energy that can be transferred to a free electron

$$T_{max} = \frac{2 m_e c^2 \beta^2 \gamma^2}{1 + 2\gamma m_e / M + (m_e/M)^2}, \tag{4.2}$$

with M the mass of the incident particle. The energy transfer to the electrons often exceeds the mean excitation energy of the absorber I, so the electrons have enough energy to ionize themselves the absorber atoms. These high energetic electrons are called δ rays. The energy loss of the primary incident particle occurs, under typical conditions, primarily via these δ rays [49]. Along the path of the charged particle, which is for most of the track a straight line, clusters of ionized atoms and electrons form due to the ionization of the material via these δ rays. The resulting free charge carriers from the ionization of the material can then further be used for detecting the incident particle, when an electric field is applied, as in the case of a diamond detector.

For high-energetic incident particles the density effect correction δ becomes important, which takes the polarization of real media into account and removes one-half of the relativistic rise.

Above $\beta\gamma = 1000$ radiative effects are dominant, which are most relevant for muons and pions. These effects lead to the generation of electromagnetic and hadronic showers and is subject to high-energy physics and related experiments as well as for studies of cosmic rays. The energy

at which ionization and radiative losses are equally important is Z dependent and lies for the element Carbon at about 1 TeV [48].
When the low energy corrections are excluded, Equation 4.1 describes for $0.1 \leq \beta\gamma \leq 1000$ the energy loss of charged particles in intermediate Z materials with an accuracy of a few %. The energy loss is normalized to the density and hence given in MeV $\mathrm{m}^2\ \mathrm{g}^{-1}$.
An accuracy of about 1% can be achieved down to $\beta \approx 0.05$ (4.7 MeV α) with the Bethe treatment, if the low energy corrections are included. The effect of atomic bonds is taken into account by the shell correction factor $\frac{C}{Z}$, which starts to play an important role at low energies, where the velocity of the incident particle is comparable to the velocity of the atomic electrons. The higher order correction $z^2L_2(\beta)$ was introduced by Bloch. The correction by Barkas, $zL_1(\beta)$, accounts for the differing stopping power of particle and antiparticle.
Below $\beta \approx 0.05$, the phenomenological fitting formulae by Andersen and Ziegler are usually used for protons. For the region where the charged particle reaches the velocity of the outer atomic electrons, Lindhard has described the energy loss as being proportional to β. The low energy corrections are described in reference [50].
At these low energies, positively charged particles like α particles tend to pick up electrons from the absorber. The effective charge of the particle reduces until it becomes a neutral atom, in the case of the α particle, a neutral He atom. Below these energies non-ionizing nuclear losses start to play the most important role for the energy loss of the particle.

The resulting stopping power from Equation 4.1 for positive muons in Cu is illustrated in Figure 4.1. In the region where the Bethe approximation applies without corrections, the stopping power reaches a minimum. The position of the minimum is Z dependent and drops from $\beta\gamma \approx 3.5$ to 3,

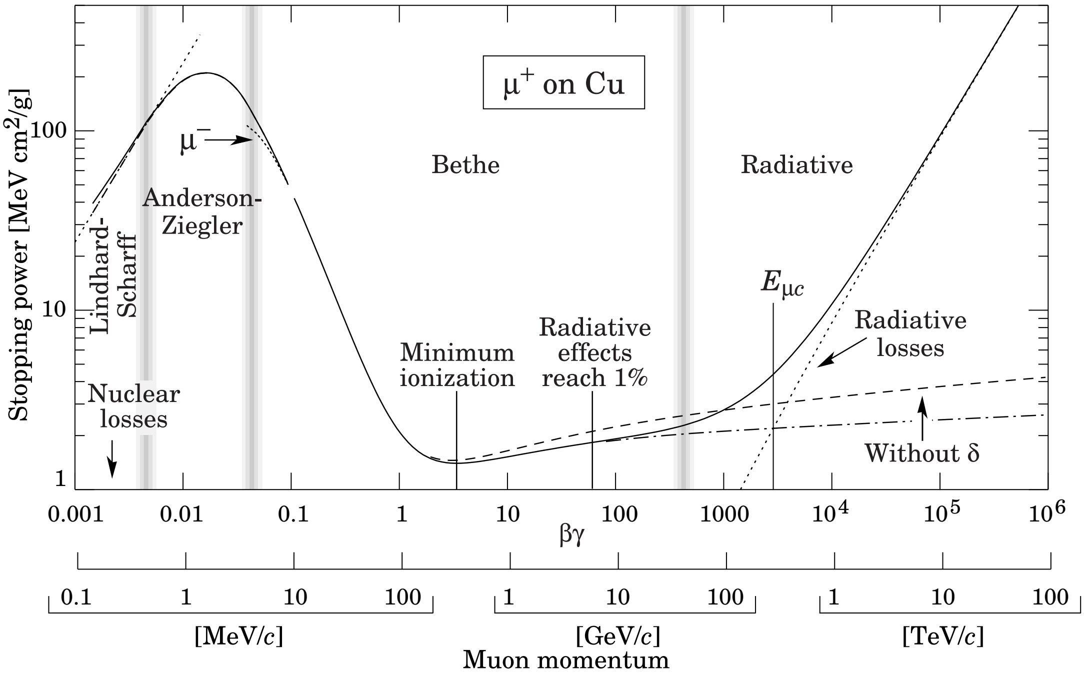

Figure 4.1: Mean energy loss of positive muons in Cu as a function of $\beta\gamma = p/Mc$, from [48]. The different regions of the approximations, as described in the text, are indicated.

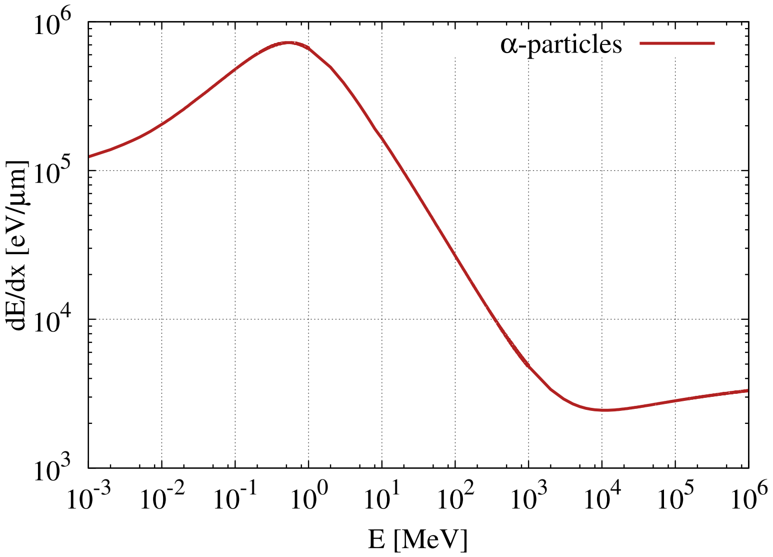

Figure 4.2: Geant4 simulation[1] *of the stopping power of α particles in diamond.*

as Z goes from 7 to 100. Particles with this energy are called minimum ionizing particles (MIP). For α particles in diamond this would be at an energy of about 10 GeV, see Figure 4.2.

The mean energy loss, given by the Bethe-Bloch equation, is used to compute the specific energy loss along the track of a charged particle in a given material. For the case where the particle is stopped within the absorber, this specific energy loss results in the so-called Bragg curve, see Figure 4.3. Spectroscopic measurements of charged particles can only be performed for such cases where the charged particle deposits its entire kinetic energy within the volume of the detector.

This is related to the fact that the energy loss of the particle is a stochastic process. When a mono-energetic beam of charged particles passes through a given layer of material the outgoing beam will be spread in energies. The width of the resulting energy distribution is a measure for the energy straggling. The straggling function, which is often called "Landau function", has a characteristic most probable value (MPV) and full width at half maximum (FWHM). The MPV is dependent on the thickness of the material layer [51], as can be seen in Figure 4.4, while the mean energy loss given by Equation 4.1 is constant for a given particle energy.

As the charged particles undergo somewhat randomly microscopic interactions in the material, each particle has also a slightly different total range. This range straggling explains the difference of the two Bragg curves shown in Figure 4.3.

Coulomb collisions between charged particles are described by the Rutherford cross-section, which can be written as a function of the kinetic energy T.

$$\frac{\mathrm{d}\sigma}{\mathrm{d}T} = \frac{2\pi z^2 Z^2 r_e^2 m_e c^2}{\beta^2 T^2}\left(\frac{m_e}{M_{nucl}}\right) \tag{4.3}$$

---

[1] Courtesy of P. Kavrigin, CIVIDEC Instrumentation

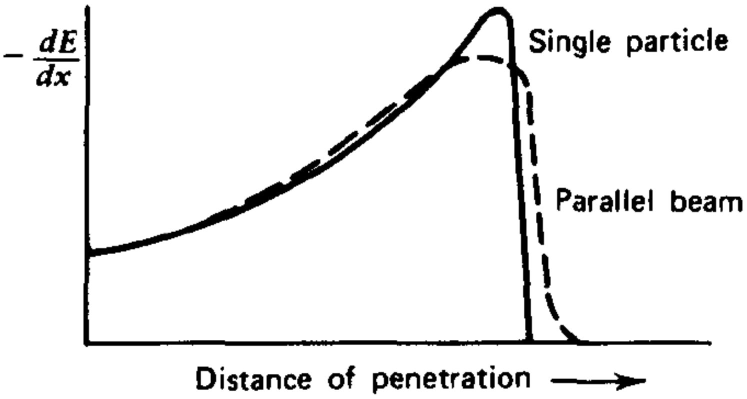

Figure 4.3: Specific energy loss along the track of an α particle with several MeV initial energy, from [49], for a single α and a beam of α particles. The difference between the two curves is due to energy and range straggling.

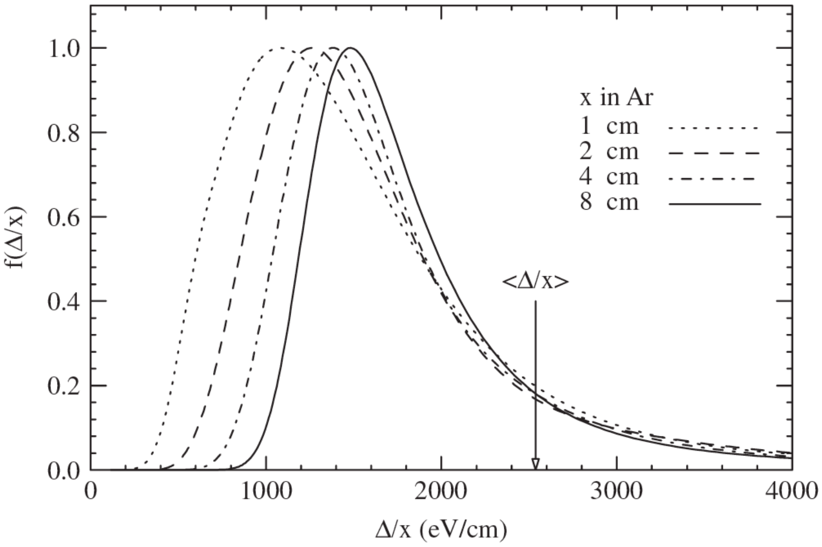

Figure 4.4: Calculated straggling functions $f(\Delta/x) = f(dE/dx)$ for $\beta\gamma = 3.6$ particles in Ar, from [51]. While the most probable value varies with the thickness x of the absorber, the mean energy loss is the same for all x.

This is dependent on the mass of the target nucleus M_{nucl} and the mass of the electron m_e. As a consequence, nuclear interactions such as Rutherford scattering or charged particle induced reactions are less likely by a factor $M_{nucleus}/Zm_e = m_{amu}/m_e \cdot A/Z$, where $m_{amu} = 931.494$ MeV/c^2 is the unified atomic mass unit. Though less likely, these reactions are the main contributors to radiation induced damage of materials, being the cause of displacement damage to crystal structures.
The stopping time of a charged particle with mass M [amu] can be estimated by the relation, [49]:

$$t \;\approx\; 1.2 \cdot 10^{-7} R \sqrt{\frac{M}{E}} \tag{4.4}$$

where R is the range of the particle in meters and E the energy of the particle in MeV. For 5.5 MeV α particles the stopping time calculates to $t = 1.4$ ps.

4.1.2 Electrons

The interaction of electrons or positrons with matter are as well governed by the Coulomb interactions. In addition to the energy loss by ionization, the energy loss due to Bremsstrahlung has to be taken into account for these light charged particles. The energy loss of electrons by Bremsstrahlung can be described by means of the radiation length X_0

$$\frac{\mathrm{d}E}{\mathrm{d}x} \;=\; -\frac{E}{X_0}. \tag{4.5}$$

The radiation length corresponds to the mean length after which the electron has lost all but 1/e of its initial energy. In addition it corresponds to 7/9 of the mean free path for pair production by a high-energy photon [48].
In principle every charged particle emits electromagnetic radiation in the form of Bremsstrahlung on acceleration. The energy loss via this radiative process is proportional to $1/\mathrm{m}_0^2$, which explains why it can be neglected for heavy charged particles, except at very high particle energies.

4.2 Interaction of Photons with Matter

The interaction processes of photons with matter are dependent on the energy of the incoming photon E_γ and the atomic number of the absorber material Z. At low E_γ the photoelectric absorption is dominant. At intermediate E_γ Compton scattering dominates the interaction of photons with matter and, at high energies, pair production is by far the most likely reaction mechanism.

Photoelectric Effect In the low energy domain the photoelectric ionization [52] is dominant. The incoming photon ionizes an absorber atom, which emits a photo-electron. The γ disappears

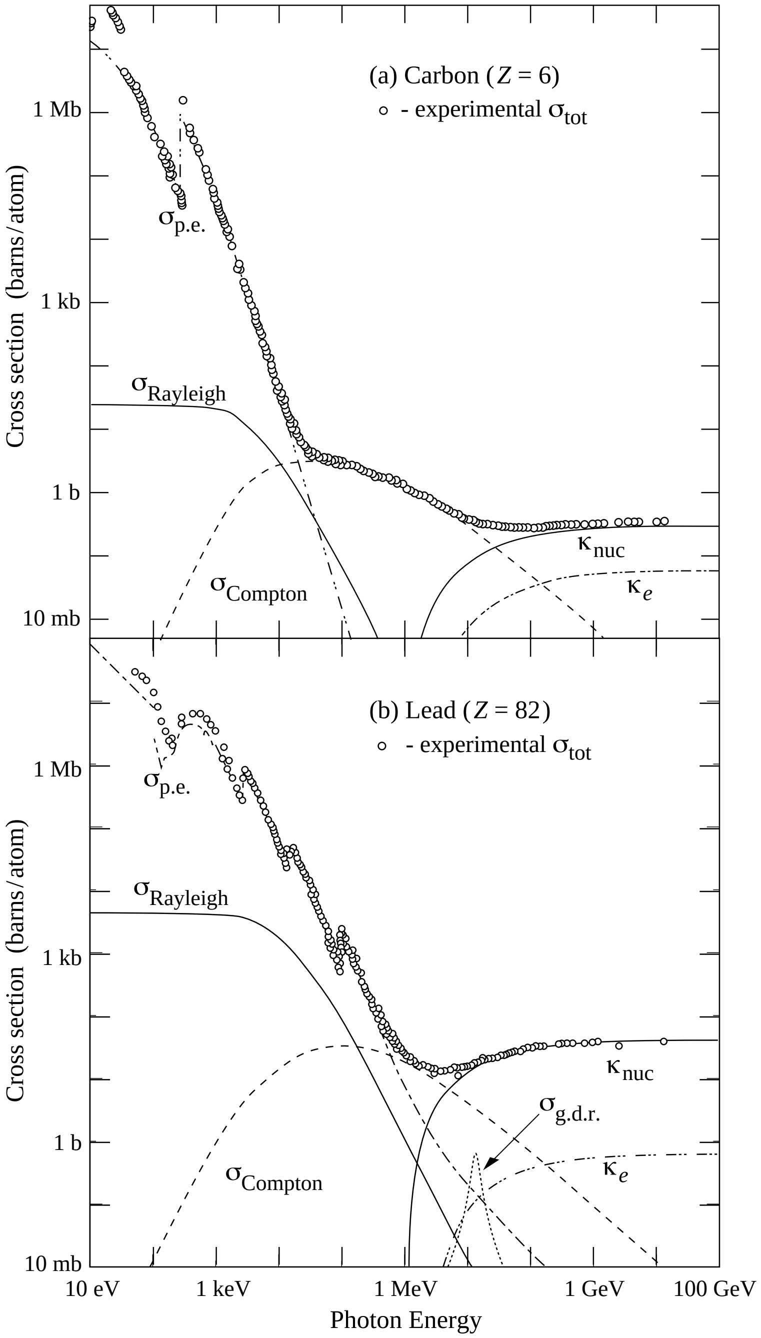

Figure 4.5: Photon total cross section and contributions of different interactions as a function of E_γ *in Carbon (a) and Lead (b), picture from [48]:*
$\sigma_{p.e.}$ = *photoelectric effect,*
$\sigma_{Rayleight}$ = *Rayleight scattering,*
$\sigma_{Compton}$ = *Compton scattering,*
κ_{nuc} = *nuclear field pair production,*
κ_e = *electron field pair production,*
$\sigma_{g.d.r.}$ = *photo nuclear interactions (target nucleus breaks up).*

completely in this process and the electron carries the excess energy of the γ with respect to the original binding energy of the electron in the atom E_B as kinetic energy E_{e^-},

$$E_{e^-} \;=\; h\nu - E_B. \tag{4.6}$$

This process is most likely to occur if the energy of the photon $h\nu$ is just above E_B, which is why 'absorption edges' can be observed in the cross-section of this reaction, corresponding to the orbital atomic shells of the absorber material. The atom predominantly de-excites after the ionization by the emission of characteristic X-rays. The emission of Auger electrons is possible as well. The photoelectric effect is the dominant mechanism in diamond detectors for $E_\gamma \leq 10$ keV. As the photon transfers its total energy to the absorber material, photon spectroscopy is in principle possible when this mechanism is dominant, but the electronic chain has to be adapted to the small amount of deposited energy.

Rayleigh Scattering Rayleigh scattering also occurs in the low energy region, although somewhat less probable. In this process the photon interacts coherently with all the electrons of an absorber atom without energy transfer. This process could be understood as γ elastic scattering. For the detection of γ this mechanism is in the first place not relevant, as the absorber material does not get ionized. On the other hand, in photon transport models and Monte Carlo simulations for the response of γ-ray detectors this effect has to be taken into account, as the photon changes its direction.

Compton Scattering Compton scattering is the dominant process at intermediate photon energies. Through the interaction with an atomic electron, the photon is deflected by an angle Θ and transfers correspondingly a fraction of its energy to the recoil electron. The photon energy after this inelastic scattering $h\nu'$ is dependent on Θ,

$$h\nu' \;=\; \frac{h\nu}{1 + \frac{h\nu}{m_0 c^2}(1 - \cos\Theta)}. \tag{4.7}$$

Even for the case $\Theta = \pi$ the photon retains some of its original energy. The photon is scattered and not absorbed in this process. The recoil electron can either go into a higher atomic shell or is emitted from the atom, dependent on the energy transfer from the photon. Compton scattering is the dominant process in diamond detectors for photon energies relevant in nuclear physics, $E_\gamma \approx$ MeV. The particle spectrum is expected to be continuous from the threshold until the maximum possible deposited energy, called the 'Compton edge'. Photon spectroscopy is not possible with small volume detectors, such as diamonds, when this process is dominant. Large volume detectors are needed for spectroscopy in this case.

Pair Production Pair production is the dominant process at high photon energies. In the coulomb field of the nucleus the γ is converted into an electron-positron pair. The threshold energy for this process is double the mass of the electron $E_{th} = 1.022$ MeV. The kinetic energy of the two reaction products is determined by $E_\gamma - E_{th}$, which is parted according to the emission angles of each particle. The positron consequently annihilates in the surrounding material.

Photo-induced Nuclear Interactions Photo-induced nuclear interactions can occur above the binding energies of the nucleons of the absorber material. Depending on the reaction products, they also contribute to the response of the detector. Due to the generally small cross-sections, photo-induced nuclear reactions are not the dominant process to be considered for the detection of photons.

In Figure 4.5 the total cross-section for photon interactions with matter as a function of E_γ is shown for Carbon and Lead. In the region where the photoelectric absorption dominates, the absorption edges corresponding to the orbital electron shells can be seen. The edge at the highest energy corresponds to the K shell and towards lower E_γ the edges corresponding to the L, M and N shell can be seen for Pb. The macroscopic cross-sections Σ of the different mechanisms scale in the following way with the atomic number Z:

Mechanism	Scaling of Σ [cm^2/g]
Photoelectric effect	Z^5/A
Rayleight scattering	Z^2/A
Compton scattering	Z/A
Pair production	Z^2/A

The cross-section for photon interactions in Pb is therefore higher than in C, as can be seen in Figure 4.5, throughout the energy range of E_γ. Still, it cannot be assumed that a diamond detector is insensitive to γ radiation and the photon background has to be taken into account for the background considerations at (n,α) cross-section measurements.
From the interaction probabilities follows that high Z materials should be used for γ spectroscopy. For typical E_γ of a few MeV in experimental nuclear physics Compton scattering is dominating. The probability for the photon to deposit its total energy in the detector volume has to be maximized for spectroscopic measurements. This is why large volume and high Z detectors are generally used for γ spectroscopy.

4.3 Interaction of Neutrons with Matter

Neutrons interact predominantly with the nuclei of matter and only via the various reaction products neutrons can be detected. The interaction probability of the neutron is expressed in terms of the cross-section σ, as introduced in Chapter 3, which is dependent on the isotope and the nuclear reaction. In addition, σ varies strongly with the energy of the incoming neutron E_n. From the various nuclear reactions that can occur, a few standard reactions are used to detect neutrons, such as ^{3}He(n,p)^{3}H, ^{10}B(n,α)^{7}Li or ^{235}U(n,f). Each of these reactions yield charged particles that can be detected and the associated cross-sections are considered standard in specific E_n intervals.

Partial cross-sections for neutron-induced nuclear reactions in ^{12}C, the main constituent of diamond detectors, are shown in Figure 4.6 together with the total cross-section, for neutron

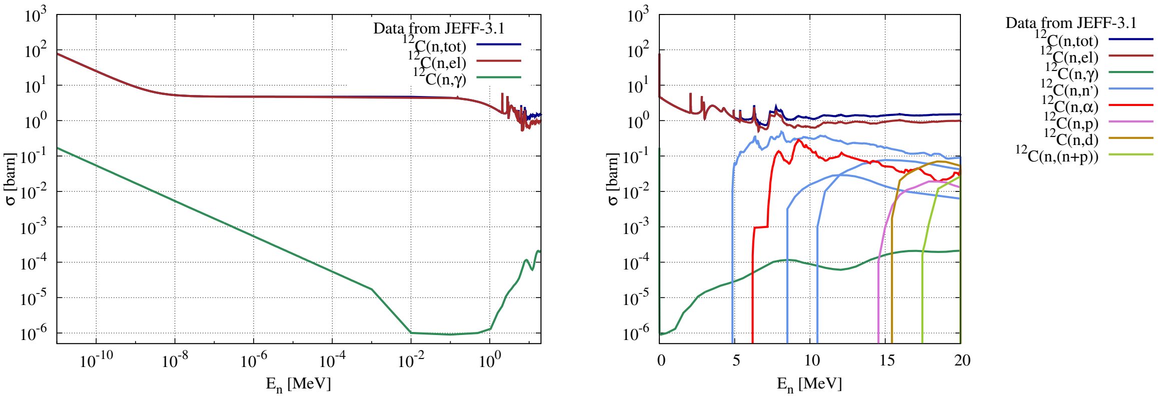

(a) For $E_n \leq 6.2$ MeV the elastic scattering is the dominant reaction.

(b) The (n,α) reaction channel opens at 6.2 MeV. The reactions (n,n') leave the ^{12}C nucleus in an excited state.

Figure 4.6: Cross-sections for different neutron-induced nuclear reactions on ^{12}C*, the main isotope in diamond detectors.*

energies up to 20 MeV. Nuclear reactions yielding charged particles only occur above E_n=6.2 MeV. Below this energy the elastic scattering of the neutron is by far the most probable reaction. When operating an in-beam detector, like the Diamond Mosaic-Detector, this reaction has to be considered for its contribution to the background. If the recoil nucleus gains sufficient energy in the elastic scattering to ionize the detector above the threshold, the elastic reaction will become detectable.

When measuring in a mono-energetic neutron beam or at a time of flight facility at $E_n \geq 6.2$ MeV with a diamond detector, all open reaction channels will contribute to the recorded signal amplitude spectrum, which corresponds to the deposited energy spectrum in the detector. The ^{12}C(n,α)^{9}Be reaction, with Q = -5.702 MeV and E_{th} = 6.181 MeV, can be distinguished the easiest from the other reactions, as it yields the highest energy deposition in the detector. This is illustrated in Figure 4.7 where a spectrum which was recorded in a (14 ± 0.2) MeV mono-energetic neutron beam [53] is converted into deposited energy. The peak corresponding to ^{12}C(n,α)^{9}Be is well separated. The mean value of the Gauss fit corresponds to $E_n - Q$ = 8.3 MeV. The energy spread of the neutron beam can be deduced from the width of the peak. The remaining spectrum is the sum of all other open reaction channels at this neutron energy and background, like γ-rays in the experimental room.

The spectrum in Figure 4.7 is a spectroscopic measurement of the reaction products at the given neutron energy. It cannot be used to deduce the neutron energy in a mixed neutron field. Neutron spectroscopy can only be performed by means of the time of flight technique.

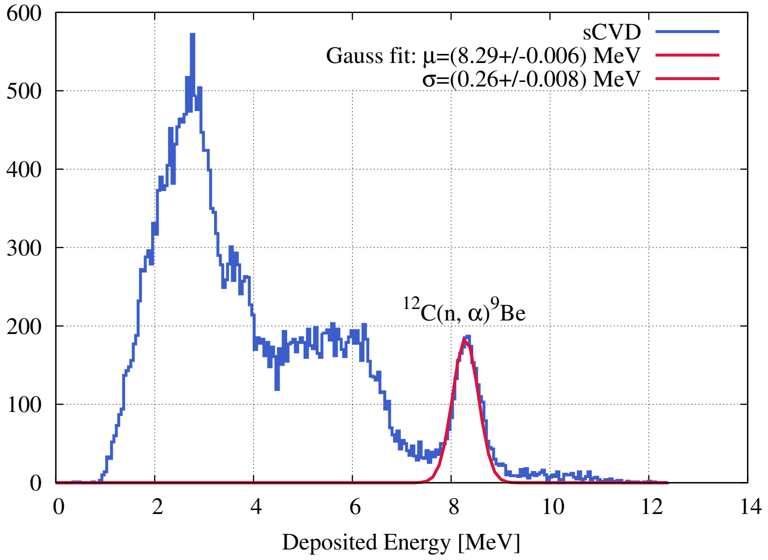

Figure 4.7: Deposited energy spectrum recorded with a sCVD diamond detector in a 14 MeV neutron beam, with an energy spread of FWHM = 0.2 MeV [53]. The peak at 8.3 MeV corresponds to α *particles coming from the* $^{12}C(n,\alpha)^{9}Be$ *reaction.*

Chapter 5

CVD Diamond Technology

Although diamond is most famous for its optical and mechanical properties, the interest in this material is constantly increasing in the scientific community. Especially in high energy physics and in fields where radiation damage is probing the lifetime of detectors, diamond became an attractive alternative for detector applications. But also other allotropes of Carbon are indispensable in the field of accelerator applications.

In this Chapter a brief introduction to Carbon and its crystalline forms is given, followed by the material properties of diamond. The different forms of diamond are presented and the chemical vapor deposition (CVD) technique to synthesize diamond is described. The third part of this Chapter is dedicated to the description of diamond detectors and which pulse shapes can be found in these semiconducting devices. If no specific reference is given, the material properties quoted in this Chapter are taken from Reference [48].

5.1 Carbon and its Allotropes

Diamond is made of the element Carbon with an atomic number Z = 6. Two stable isotopes of Carbon can be found in nature, ^{12}C and ^{13}C, where the natural abundance of ^{13}C is only about 1.1%. In natural Carbon also traces of the radioactive isotope ^{14}C can be found, which disintegrates via β^- decay to ^{14}N with a half-life of 5730 years.

Allotropes of pure Carbon can traditionally be classified as either graphite or diamond, see phase diagram of C in Figure 5.1, where the two materials differ from the crystalline structure and have consequently opposing material properties. Another commonly known allotrope is amorphous Carbon, which has a glass structure rather than a crystal lattice. More exotic allotropes of carbon are fullerenes, Ionsdaleite or carbyne which are synthesized materials and of great interest in material science. The variety of material properties that can be found in the different Carbon allotropes is worth noticing. One of the most anisotropic materials are carbon nanotubes, the strongest material ever tested is graphene and one of the softest materials known is graphite.

The crystallization of Carbon atoms in a face-centered cubic (fcc) lattice, with two atoms at

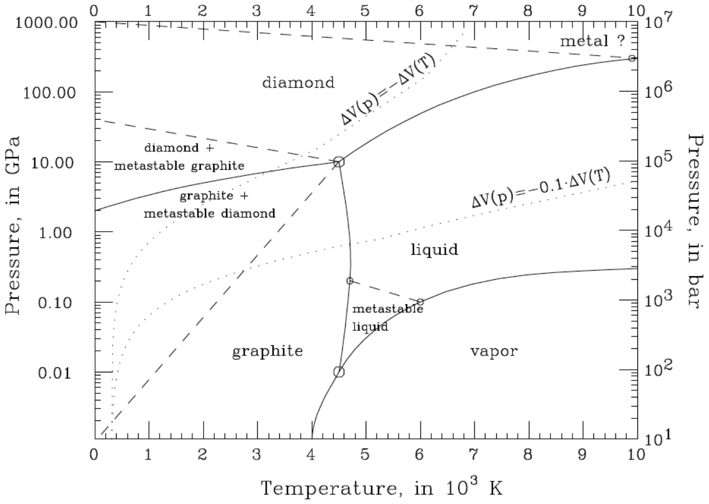

Figure 5.1: Phase diagram of Carbon, picture from [54].

each lattice point, one at [0,0,0] and the other at $[\frac{1}{4}, \frac{1}{4}, \frac{1}{4}]$, is classified as diamond. The coordinates are fractions of the cubic sides, with a cubic lattice constant of a = 3.567 Å [55] which makes the closest distance between two C atoms in diamond 1.545 Å, see Figure 5.2. The density of diamond calculates to 3.52 g/cm^3, given the mass number of natural carbon A = 12.0107 and the atomic density of $1.76{\cdot}10^{23}$ atoms/cm^3. The atomic density of diamond is the highest of any matter on Earth.
The C atoms in diamond are strongly bound to each other, with a cohesive energy of 3.62 eV/bond or 7.24 eV/bond respectively. The exceptional thermal conductivity of up to 2500 W/(Km), the fact that diamond is the hardest natural material, actually the only material which reaches Mohs hardness 10 [55], and the relatively high displacement energy of 43 eV/atom [56], result from these strong covalent bonds. The hardness of diamond is dependent on the crystal orientation, which is why diamond can be polished with diamond powder.

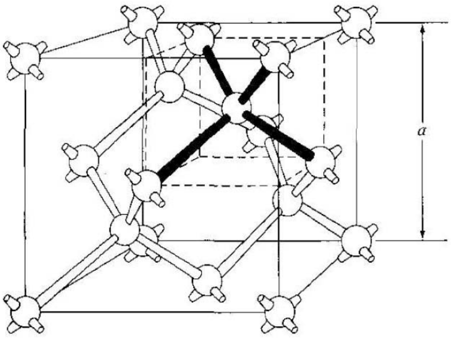

Figure 5.2: Unit cell of diamond with a the cubic lattice constant, picture from [23].

Carbon preferably crystallizes in a hexagonal lattice at room temperature and atmospheric pressure, which is why graphite is the thermodynamical stable allotrope of Carbon at these conditions. Still diamond is metastable at ambient conditions, as the activation energy for the phase transition into graphite is too high. In accelerator applications graphite is used for collimators and beam dumps to absorb high energetic particles. In diamond detector applications the preferential formation of graphite is disadvantageous for the diamond synthesis, as it is electrical conductive in contrast to diamond which is a perfect insulator.

In real diamonds imperfections of the crystal lattice can be found, which originate from the formation process of the diamond or are induced by irradiation. These crystal defects distort the periodicity of the lattice and can change the electronic properties of the material.

Zero-dimensional defects are either C or foreign atoms which take an irregular place in the lattice, or vacancies. Such point defects distort the crystal lattice locally. Common impurities in diamonds are N, B or H atoms which are incorporated in the diamond bulk during the production process. Diamond can be classified after the amount of N which can be found in the lattice, with type IIa diamond being the best quality material, which is nearly N free and has very good electronic properties. Element 6 Ltd., Great Britain, specifies electronic-grade single-crystal diamond material with less than 5 ppb N-impurities [57].

One-dimensional or line defects are places where a crystal plane stops within the crystal.

Grain boundaries are two-dimensional defects. They form where two crystal grains with different orientation meet. The electronic quality of diamond depends strongly on the density of these grain boundaries as they act like charge trapping centers.

Bulk defects are three-dimensional. These are regions where many defects or graphite inclusions can be found and foreign atoms cluster. Especially graphite inclusions change the electronic properties of a diamond significantly. When bulk defects extend through the whole thickness of the crystal, the diamond cannot be used as detector anymore, as it will not sustain the voltage. On the other hand, when bulk defects are induced in a controlled way, 3D diamond detectors can be built [58].

Crystal defects have a certain mobility which can be thermally enhanced. One takes advantage of this defect-mobility in the purification processes of, for instance, Si mono-crystals and also at the thermal treatment, or annealing, of crystals with radiation-induced damage, which is also practice for diamond sensors [23].

5.2 Diamond Synthesis and Materials

Apart from natural diamond, which is very limited in size and often suffers from high impurity densities [59], two types of artificial diamond are available nowadays, high pressure high temperature (HPHT) diamond and chemical vapor deposition (CVD) diamond.

The natural synthesis of diamond is mimed in the HPHT method. Here graphite is converted into diamond in an environment of 1500 - 2000°C and 50 - 100 kbar supported by suitable catalysts. The first artificial diamond was synthesized with this method in the 1950s [60, 61, 62]. The artificial diamonds resulting from this technique are in general not suited as electronic-grade material for detector applications, due to the relatively high N concentration (yellowish color) and high crystal defect densities.

In contrary, the plasma-assisted CVD technique allows to grow diamond on a suitable seed. The principle of this method is based on chemical reactions occurring in a gas phase above a solid surface and consequently deposition of material onto this surface. Methane (CH_4) is generally

used as Carbon supply for the diamond growth in this technique and in combination with Hydrogen gas (H_2) it provides the reactants in the gas phase. Atomic Hydrogen in the plasma reduces Methane to Carbon or reactive radicals like CH_3, which eventually deposit on the cooled surface of the seed. In addition atomic H etches graphite from the surface, prevents the built up of polymers and keeps the diamond lattice stable by termination of the surface. Detailed information on the diamond growth can be found in References [63] and [64].
Besides the chemical conditions in the reaction chamber, the seed that is used for the diamond growth governs the quality of the resulting diamond and hence its electronic properties.

- Homo-epitaxial growth: Here diamond is used as a seed for the CVD growth
    1. pCVD diamond: For the synthesis of poly-crystalline chemical vapor deposition (pCVD) material, diamond nano crystals or poly-crystalline diamond are used as substrate. The resulting diamond bulk contains grain-boundaries where crystals, growing from different seeds, eventually meet. For applications as grinding material this is advantageous, as it has a self-sharpening effect. However, the electronic properties of this material are less favorable as these boundaries act like charge trapping centers for free charge carriers. For spectroscopic applications this material is not suited [65]. Still it has been proven that this material is well suited for beam-loss monitoring [66, 67], beam conditions monitoring, for single MIP particles [68] and up to 10^9 particles per pulse [69] and time of flight measurements [70] in accelerator environments.
    2. sCVD diamond: For the synthesis of high quality single-crystal chemical vapor deposition (sCVD) diamonds the substrate of choice is usually a surface-treated HPHT diamond with a <1 0 0> orientation [71]. The sCVD diamond is separated from the HPHT substrate after the growth by a laser-cutting technique and polished to the desired thickness and surface smoothness. High quality electronic grade diamonds are nowadays grown in this way. The area of these diamonds is restricted to about 4.5 x 4.5 mm^2, caused by the restricted size of the HPHT seeds. The thickness of the available substrates is typically 500 μm.
- Hetero-epitaxial growth: Here a substrate with a diamond like crystal structure is used as seed. In recent years a big effort has been made in order to obtain large area CVD diamonds in good quality with this method. At the University of Augsburg, Germany, sCVD material was for the first time successfully grown with this method using an Iridium layer as seed [72, 73]. This material, transitionally called Diamond on Iridium (DOI), has not yet reached the quality of homoepitaxially grown sCVD diamond, as the two- and one-dimensional crystal defect density still needs to be reduced. However this material is a promising candidate for future detector applications, and should eventually meet the requirements for spectroscopic applications. One DOI substrate was tested[1] with the Diamond Mosaic-Detector, which is described in the second and third part of this thesis, for its applicability for (n,α) cross-section measurements.

---

[1] Courtesy Matthias Schreck, Univeristy of Augsburg, Germany

5.3 Electronic Properties of Diamond

Diamond is an insulator in terms of conductance. For detector applications it is more suitable to classify it as wide band gap semiconductor. The band gap of diamond is 5.47 eV [74], which results in a free charge carrier density at room temperature of less than 10^3 cm^{-3}. This makes diamond a very low-noise detector material and a potential candidate for detector applications in high temperature environments. Measurements at 200° C ambient temperature have already been reported [75]. On the other hand, also its application at cryogenic temperatures of 1.6 K has been proven [26].

The dielectric constant of diamond is $\varepsilon_r = 5.7$, which is advantageous for measurements, as the capacitance for a given detector-geometry is lower than for most other semiconductor materials, like Si with $\varepsilon_r = 11.9$. For the typical geometry of a sCVD diamond sensor, with 500 μm thickness and 4 x 4 mm^2 electrodes, the capacitance calculates to C = 1.6 pF. The time constant, which limits the bandwidth of a system inversely, is linearly dependent on the input capacitance. Hence, the smaller the capacitance, the faster the system. On the other hand, the response of charge sensitive electronics is dependent on the input capacitance, where the signal-to-noise ratio (SNR) worsens with increasing capacitance.

The intrinsic resistivity of a sCVD diamond can exceed 10^{16} Ωcm [76]. With a bias voltage of 1 V/μm the leakage current is less than 10^{-12} A, for high-quality crystals. Crystal defects can lower the resistivity of diamond up to an electrical shortcut, which would be the case for graphite inclusions which extend through the whole thickness of the diamond bulk.

The low-field mobility μ_0 of electrons (e$^-$) and holes (h$^+$) at room temperature was measured by various groups. For natural diamonds $\mu_{0,e^-} = 2500$ and $\mu_{0,h^+} = 2100$ cm^2/Vs are reported [77, 78, 79], where it should be noted that $\mu_{0,e^-} > \mu_{0,h^+}$. For CVD diamond the published values extend over a wide range with 1300 cm^2/Vs $\leq \mu_{0,e^-} \leq$ 4500 cm^2/Vs and 2050 cm^2/Vs $\leq \mu_{0,h^+} \leq$ 3800 cm^2/Vs. Furthermore, according to Isberg in Reference [74], the mobility of charge carriers varies substantially with the quality of the crystal. Two authors, Pernegger [80] and Pomorski [81], report higher values for the mobility of holes in diamond.

Due to the discrepancy of the reported values, the drift velocity v_{dr} in a 500 μm sCVD diamond was measured with the transient-current-technique with α particles. The data was fitted with the function used by Pernegger et al. [80], with the two parameters μ_0 and the saturation velocity v_s

$$v_{dr} = \frac{\mu_0 E}{(1 + \frac{\mu_0 E}{v_s})}. \tag{5.1}$$

In this work the values $\mu_{0,e^-} = (1530 \pm 160)$ cm^2/Vs and $\mu_{0,h^+} = (2660 \pm 160)$ cm^2/Vs are used for the low-field mobility, resulting from this measurement and being consistent within the range of reported values. The corresponding saturation velocities are $v_{s,e^-} = (1.12 \pm 0.05) \cdot 10^5$ m/s and $v_{s,h^+} = (1.29 \pm 0.03) \cdot 10^5$ m/s for electrons and holes, respectively. The measured drift velocities as a function of the electric field for e$^-$ and h$^+$ are shown in Figure 5.3.

The energy to create an electron-hole pair in diamond is predicted to be $\epsilon = 11.6$ eV/e-h from theoretical calculations [82]. The published experimental values vary in a range of 11.1 - 24 eV. For IIa natural and HPHT diamond 13.1 eV/e-h were reported [83, 84]. Pernegger et al. [80] report (17.6 ± 2.7) eV/e-h for CVD diamond and Kaneko reported (16.1 ± 0.5) eV/e-h [85]. Pomorski reported (12.86 ± 0.05) eV/e-h [23]. In this work the value $\epsilon = 13.6$ eV/e-h [63] is used as a reference.

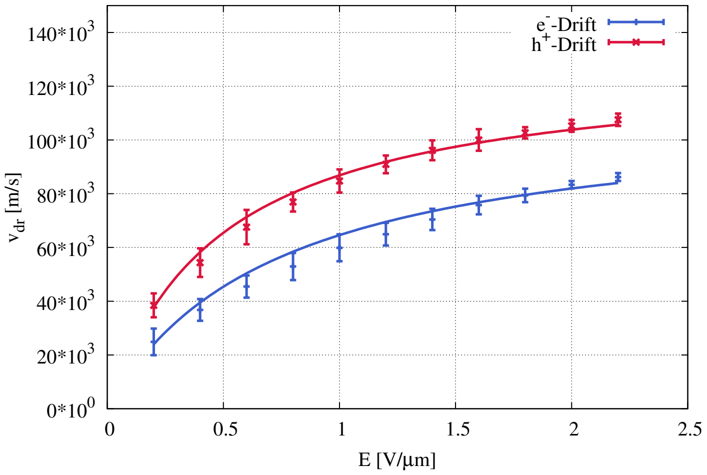

Figure 5.3: Measurement of the drift velocity v_{dr} *in sCVD diamond. The data was fitted using Equation 5.1 for the parameters* μ_0 *and* v_s*. The resulting low-field mobility is* $\mu_{0,e^-} = (1530 \pm 160)$ cm^2/Vs *and* $\mu_{0,h^+} = (2660 \pm 160)$ cm^2/Vs *for electrons and holes respectively. For the saturation velocities* $v_{s,e^-} = (1.12 \pm 0.05) \cdot 10^5$ m/s *and* $v_{s,h^+} = (1.29 \pm 0.03) \cdot 10^5$ m/s *resulted from the fit for electrons and holes respectively.*

In Table 5.1 the electronic properties of diamond are summarized. The values for each property, which are used in this work, are given in the third column.

Table 5.1: Electronic properties of diamond, the range of published values are listed as well as the values which are used as reference in this work.

Property	Published Values	Used here
Band gap [eV]	5.47	5.47
Dielectric constant ε_r	5.7	5.7
Intrinsic resistivity [Ωcm]	up to 10^{16}	10^{16}
Electron mobility μ_{0,e^-} [cm^2/Vs]	$1300 \leq \mu_{e^-} \leq 4500$	1530
Hole mobility μ_{0,h^+} [cm^2/Vs]	$2050 \leq \mu_{h^+} \leq 3800$	2660
Energy to create e$^-$-h$^+$ pair ϵ [eV]	11.1 - 24	13.6
MIP stopping power [eV/μm]	36	36

5.4 Signal Creation in Diamond Detectors

The signal creation in a diamond sensor is described in the following by deriving the electric field in a parallel plate capacitor and calculating the current using the Shockley-Ramo theorem. Finally, the theoretical pulse shapes are compared with measurements.

5.4.1 Electric Field in a Diamond Sensor

The equivalent circuit diagram to a diamond sensor is a current source in parallel with a parallel-plate capacitor. The analysis of the detector can be seen as having three levels.
First, there is the regime dominated by the bias field, which is typically between 0.5 V/μm and 1 V/μm.
Second, there is the regime that includes the static electric field from space charge (Q_{sc}) [80]. Space charge is typically caused by impurities, radiation damages or trapped charges from a recent irradiation.
Finally, there is the regime that includes the self space-charge arising from the mobile charge carriers created by the passage of an ionizing particle. Unless there are many co-incident ionizing particles (or we are looking for very small effects), the influence of the self space-charge is weak and can be neglected.
If a space charge is homogeneously distributed in the volume V of the diamond bulk, it will induce $-Q_{sc}/2$ on each electrode and the space charge density becomes $\varrho_{sc} = Q_{sc}/V$. The applied bias voltage (HV) to the sensor induces an areal charge $\sigma_0 = Q_0/A$ on the surfaces of the electrodes, with A the area of the electrodes. The integrated charge through the sensor is then given by

$$\begin{aligned} Q(0) &= Q_0 - \frac{Q_{sc}}{2} \\ Q(0 < x < d) &= Q_{sc} \\ Q(d) &= -Q_0 - \frac{Q_{sc}}{2}. \end{aligned} \tag{5.2}$$

The electric field $\mathbf{E}$ is obtained using the macroscopic form of Gauss's law

$$\nabla \mathbf{D} = \rho \tag{5.3}$$

with the electric displacement field $\mathbf{D} = \varepsilon \mathbf{E}$ as a product of the absolute permittivity ε and $\mathbf{E}$ and the charge carrier density ρ. The absolute permittivity is given by $\varepsilon = \varepsilon_0 \varepsilon_r$ the product of the vacuum permittivity ε_0 and the relative permittivity or dielectric constant ε_r of the material. For a parallel-plate capacitor, the problem is unidimensional and the electric field intensity can be expressed by

$$E = \frac{1}{\varepsilon} \int \rho \, \mathrm{d}x. \tag{5.4}$$

When integrating over the charge distribution 5.2, the electric field distribution inside the diamond sensor ($0 < x < d$) can be obtained

$$E(x) = \frac{1}{\varepsilon A} \left(Q_0 - \frac{Q_{sc}}{2} + \frac{Q_{sc} A}{V} x \right). \tag{5.5}$$

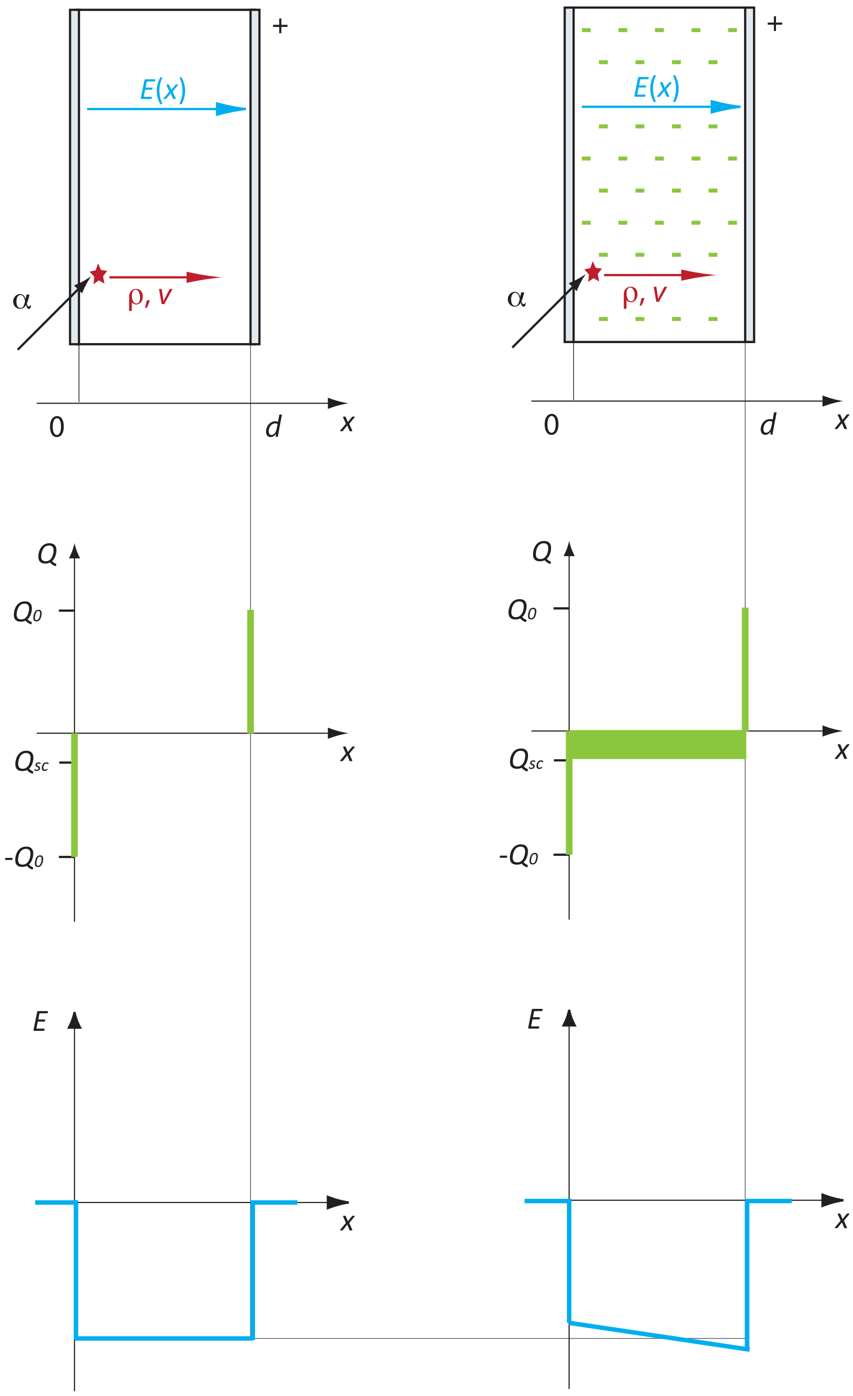
+
E(x)
α
ρ, v
0
d
x
Q
Q0
Qsc
-Q0
x
E
x
+
E(x)
α
ρ, v
0
d
x
Q
Q0
Qsc
-Q0
x
E
x

Figure 5.4: Schematics of a diamond detector under positive bias voltage with thickness d, without (left) and with homogeneously distributed negative space charge Q_sc *in the bulk (right). The electric field results directly from the charge distribution and influences the shape of the current pulse which is induced by the* α *particle.*

The charge distribution and the electric field distribution is illustrated in Figure 5.4 for a neutral diamond on the left and a diamond with homogeneously distributed, negative space charge in the bulk on the right.

5.4.2 Induced Current from Ionizing Particles

When an ionizing particle is entering the diamond sensor, free charge carriers, namely electrons (e^-) and holes (h^+) are created. A charge cloud with charge density $\varrho_{ion}(x, y, z, t)$ forms along the path of the particle. If an electric field is applied, the charges are moving through the diamond bulk to the respective electrode, following the Lorentz force

$$\mathbf{F} \;=\; q \cdot [\mathbf{E} + (\mathbf{v} \times \mathbf{B})]. \tag{5.6}$$

Since self space-charge forces are weak, the uniform bias field and the field from trapped charges (if present and uniform) will dominate and a uni-dimensional model can be assumed. Hence, for a parallel-plate capacitor, with $E = U/d$, where U is the applied voltage and d the thickness of the capacitor and in absence of a magnetic field ($\mathbf{B} = 0$) the above expression simplifies to

$$F \;=\; q \cdot \frac{U}{d}. \tag{5.7}$$

Schockley [86] and Ramo [87] have expressed the instantaneous current I induced on the electrodes of a vacuum tube by a moving charge q as

$$I \;=\; q \cdot \frac{v_{dr}}{d}, \tag{5.8}$$

with the drift velocity v_{dr} and the thickness of the device d. This so called Shockley-Ramo theorem states that the current can be expressed in an electrostatic way at each moment of charge movement.

When neglecting the self space-charge field, v_{dr} can be expressed as a function of the electric field, $v_{dr} \;=\; \mu E$, by introducing the mobility μ of charge carriers in a material. With this expression the current becomes a function of E,

$$I \;=\; \frac{q}{d} \mu E. \tag{5.9}$$

Dividing this expression by the active area of the sensor and using $\varrho_{ion}(t)$, yields an expression for the current density $i(t)$,

$$i(t) \;=\; \varrho_{ion}(t) \mu_{ion} E. \tag{5.10}$$

The current is a superposition of the electron and the hole movement, where $\varrho_{ion}(t)\mu_{ion}$ represents the sum, $\varrho_{ion}(t)\mu_{ion} = [\varrho_{e^-}(t)\mu_{e^-} + \varrho_{h^+}(t)\mu_{h^+}]$.

In real diamonds, crystal defects in the form of impurity atoms, dislocations, stacking faults and grain boundaries can be found. These defects act like charge trapping centers or can enhance the recombination of free charge carriers. Due to the possible loss of charge carriers along their path through the bulk, their lifetime τ_{ion} is reduced, which has an influence on the current

$$i(t) \;=\; \varrho_{ion}(t) \mu_{ion} E \exp\left(-\frac{t}{\tau_{ion}}\right). \tag{5.11}$$

For ideal crystals τ_{ion} is infinite and the current density is not affected by the exponential term anymore. In pCVD materials the effect of the exponential term is dominant and charges recombine or get trapped during their drift. In DOI sensors a different life time of charge carrier types can be observed, where $\tau_{h^+} > \tau_{e^-}$ [88].
For spectroscopic applications it is mandatory that the life time of the charge carriers is much larger than the drift time, $\tau \gg t_d$, in order to allow the full charge collection. The Shockley-Ramo theorem implies that the collected charge at the electrode is equivalent to $q \cdot x_0/d$, where x_0 is the drift path of the free charge carrier with charge q. Only the simultaneous creation of e^-h^+-pairs and their respective movement to the opposite electrodes guarantees the effective charge drift over the full length d and hence the full charge collection, which is a requirement for spectroscopic measurements. For this reason, pCVD material is not appropriate for spectroscopy [65]. The full charge collection corresponds to the number of e^-h^+-pairs.

5.4.3 Pulse Shapes in Diamond Detectors

The current-pulse shape is caused by the ionization profile in the diamond sensor, which depends on the particle type, its energy and the dimensions and properties of the diamond material. Furthermore, the shape of the current-pulse in an ideal sCVD diamond detector reflects in turn the ionization profile. This is a unique feature of diamond detectors and allows particle identification by pulse-shape analysis (PSA). It can be used for background rejection in mixed particle fields [89]. In the following, the current-pulse shapes are given for α particles, MIP particles and neutron interactions in CVD diamond sensors.

Partial Penetration of a Charged Particle Assuming the situation indicated in Figure 5.4, an α particle with $E_\alpha = 5.5$ MeV enters a 500 μm thick diamond sensor, an ideal single crystal, through the ground electrode. A positive electric field (1 V/μm) is applied to the sensor and the signal is read out via the HV side of the detector.
The range of the α particle is 14 μm. The total kinetic energy of the α will be deposited in the diamond bulk and free charge carriers will be created. The total amount of created electron-hole pairs N_{eh} can be calculated with the pair creation energy in diamond $\epsilon = 13.6$ eV to

$$N_{eh} = \frac{E_\alpha}{\epsilon} = 4.04 \cdot 10^5.$$

This corresponds to a charge of $Q_{ion} = 65$ fC. A bar of charge can be assumed as ionization profile for each of the charge carriers. The maximum drift path d_{max} for holes will be 14 μm, while it is 500 μm for the electrons. With the typical drift velocities v_{dr} at 1V/μm of electrons and holes in diamond, the maximum drift times t_{max} can be calculated:

	v_{dr} [m/s]	d_{max} [μm]	t_{max} [ns]
e$^-$	$6 \cdot 10^4$	500	8.3
h$^+$	$8.5 \cdot 10^4$	14	0.165

The drift times are obtained under the assumption that the charge carriers are instantaneously accelerated to their constant drift velocity, at the time of their creation. The time to accelerate an electron with an electric field of 1 V/μm to the drift velocity of $6{\cdot}10^4$ m/s is 0.3 ps. The assumption of an instantaneous acceleration is hence correct in a first approximation, where the self-space charge of the created charge cloud is neglected as well as the effect of the crystal lattice on the motion of the charge carriers.

As it only takes 165 ps for the holes to arrive at the cathode, the current pulse will be dominated by the drift of the electrons through the diamond bulk. The shape of the current pulse will be rectangular and negative, with a very short additional peak caused by the hole drift. If space charge is present in the diamond bulk, the rectangular shape would rather be rhombic, as indicated in Figure 5.4.

According to the Shockley-Ramo theorem, see Equation 5.8, the area of the pulse is proportional to the deposited charge in the diamond. The number of created electron-hole pairs corresponds to a charge of 65 fC, which is the expected area of the current signal. With $t_{max} = 8.3$ ns, the maximum current is expected to be 7.8 μA, or 0.4 mV when measuring in a 50 Ω system.

In Figure 5.5 the corresponding theoretical shape is shown in comparison with an average signal,

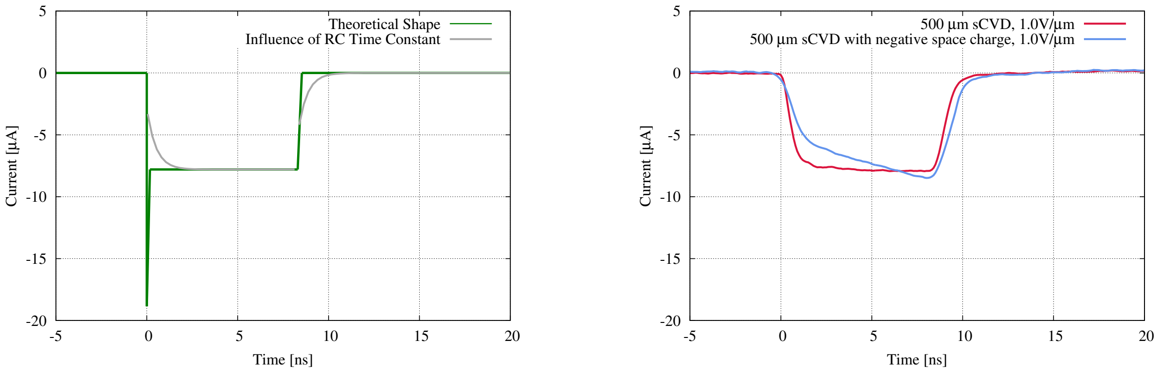

(a) Theoretical shape in green with the influence of the RC time constant in grey.

(b) Measured signal of sCVD diamond sensors without (red) and with (blue) negative space charge.

Figure 5.5: Comparison of the theoretical and measured pulse shapes for a signal created by a ^{241}*Am* α *in a 500* μ*m sCVD diamond sensor, which is operated at* $E = 1$ *V/*μ*m, when* e^-*-drift is dominating the signal.*

recorded with a 500 μm sCVD diamond detector and a ^{241}Am α source. The influence of the *RC* time constant, which is of the order of a few hundred pico seconds, to the theoretical shape is indicated as well in Figure 5.5(a). The deviation of the measured pulse shape from a perfect rectangle is dominated by this electric time constant. The signal recorded with a sCVD diamond sensor with negative Q_{sc} in the bulk is also illustrated in Figure 5.5(b), where the rhombic shape can be seen.

The separation and diffusion of the created charge cloud influences as well the shape of the current pulse [90]. Only the outer part of the charge cloud will see the electric field in the sensor in the very beginning, while the inner part will be shielded. As the charge cloud drifts apart, an increasing number of charges will be accelerated to the drift velocity by the applied electric field E_x. During this time the current pulse will increase until all charges have reached the drift velocity. Hence the rise time of the current pulse is related to the separation of the charge cloud. During the drift, an elongation of the charge cloud occurs caused by the particle density gradient in the cloud. Because of this diffusion, the fall time of the current pulse is longer than the rise time.

In order to avoid recombination, the separation of the e^-- and h^+-clouds has to happen faster than the recombination time constant, which was reported to be ≤ 20 ns [91]. This requires a high electric field for spectroscopic applications, typically $E \geq 0.5$ V/μm.

If the α particle in Figure 5.4 is injected from the HV side of the detector and the diamond is biased with positive voltage, the drifting of the holes would be dominating the signal. The measured pulse would be again rectangular, but with a smaller FWHM and a higher maximum amplitude, corresponding to the higher drift velocity of the holes in diamond and the constant amount of deposited charge by a 5.5 MeV α particle. A measured average signal is illustrated in red in Figure 5.6(a). The properties of diamonds can hence be studied when measuring the current pulse, which is called a transient-current technique measurement (TCT measurement).

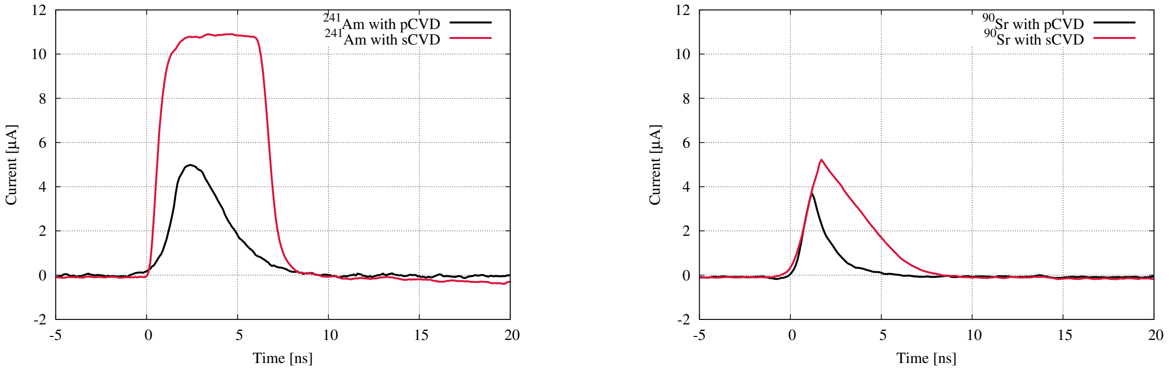

(a) Average signals recorded with particles partially penetrating the detector (α from ^{241}Am). The h^+-drift is read out.

(b) Average signals recorded with particles traversing the detector (β from ^{90}Sr).

Figure 5.6: Measured pulse shapes in CVD diamond detectors. The 500 μm thick detectors are operated at $E = 1$ V/μm. The reduced efficiency of the pCVD material (black) can be seen in both cases. The signal is triangular, even for α particles, and has an exponential decay. The area of the signals is significantly smaller than the the area of the sCVD pulses (red).

Passage of an ionizing Particle The pulse shape changes when a charged particle is traversing the diamond perpendicular to the electrodes. The created charge cloud is extended from one electrode to the other and electrons as well as holes are absorbed on the corresponding side from the very beginning. This results in a triangular pulse shape as free charge carriers are permanently absorbed by the electrodes. For a minimum ionizing particle 36 e-h pairs are on average created per μm. The area of the pulse corresponds to the charge of $N_{eh} = 18\ 000$ e-h pairs in a 500 μm thick diamond and the expected area of the average signal recorded is 2.9 fC.

Average signals recorded with a ^{90}Sr source can be seen in Figure 5.6(b) for a sCVD and a pCVD detector in comparison. The β particles from this source traverse a 500 μm diamond and can be classified as MIP particles. The signal shapes for both diamond detectors are triangular. The signal from the pCVD detector is smaller, which indicates a reduced charge collection efficiency. In addition, the falling edge of the pCVD signal is exponential rather than linear. This indicates that free charge carriers are trapped on the way to the electrodes.

In pCVD material, also the measurement of α particles yields an exponential pulse shape due to the loss of free charge carriers during the drift. This is illustrated in Figure 5.6(a), where the signal recorded with a pCVD detector is compared to the rectangular signal recorded with a sCVD detector.

Generation of ionizing Particles in the Volume of the Diamond Sensor When a diamond detector is operated in a high-energetic neutron beam, the ionizing particles are created at random places inside the diamond bulk via nuclear reactions [53]. In this case pulses dominated by the e$^-$-drift will be measured as well as pulses dominated by the h$^+$-drift and a superposition of the two, from particles that are stopped in the diamond sensor. In addition, triangular pulse shapes will be measured when the ionization track is extending throughout the diamond thickness.

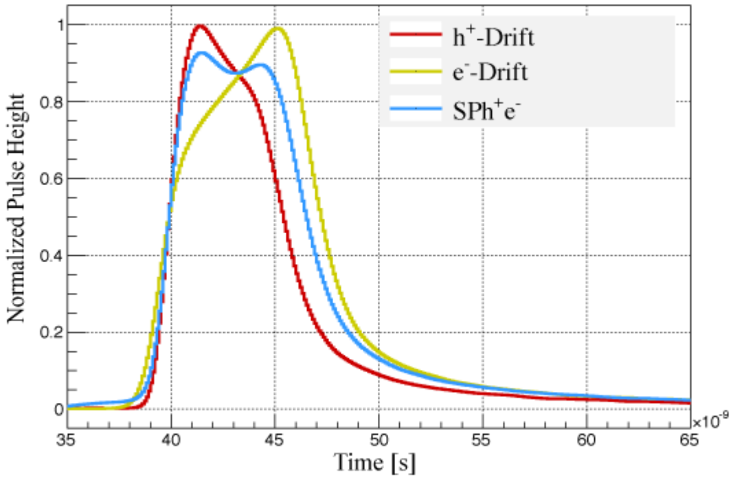

Figure 5.7: Rectangular pulse shapes measured in a 14 MeV neutron beam. Signals dominated by the hole drift (red) as well as signals dominated by the electron drift (yellow) can be observed. The superposition of the two (blue) can be observed when the ionizing particle is created in the center of the detector [92].

In Figure 5.7 rectangular pulse shapes measured with a 500 μm thick sCVD diamond detector in a 14 MeV neutron beam are shown [53, 92]. The detector in use had negative space charge in the bulk. Signals which are dominated by the e$^-$-drift are hence expected to have a positive slope at the crest, while a negative slope is expected when the h$^+$-drift dominates. Pulses were selected according to the slope of the crest.

As a result, the pulse shape illustrated in red is dominated by the h^+-drift and the nuclear reaction happened close to the positive electrode of the detector. The average signal illustrated in yellow is dominated by the e^--drift, which is confirmed by the wider pulse shape, being consistent with the smaller drift velocity of e^- in diamond. When the nuclear reaction takes place in the center of the detector, a superposition of the two signal shapes can be observed, as indicated in blue.

Chapter 6

Electronics

In order to make single particles measurable with a diamond detector, the signals have to be electronically amplified. For the study of detector physics, where the shape of the current pulse is relevant, a current amplifier is used. For spectroscopic applications, where the ionization charge is the relevant quantity, a charge amplifier is favourable.
In this Chapter, the basic principles of these two types of amplifiers are presented before a brief introduction to the concepts of time and energy resolution and the quantities which influence the latter. Finally the calibration of electronics is presented.
In the case where a high particle fluence hits the detector, the amplification is not needed anymore and the signal can be read out directly from the diamond detector [70]. In high-radiation environments, for example the HiRadMat facility at CERN, the output of the detector rather has to be attenuated [69]. But also for this type of measurement, the influence of the RC time constant on the signal has to be taken into account, which will be introduced below.

6.1 Electronic Time Constant

The equivalent circuit diagram of a diamond detector is a current source with the detector capacitance C_d and the input impedance R_i of the measuring system in parallel, see Figure 6.1. This system has a RC time constant [49] which is relevant for the quality of the current measurement

$$\tau \;=\; R_i C_d \;=\; \frac{1}{2\pi f_u}, \tag{6.1}$$

where f_u is the upper cut-off frequency. For the typical geometry of a sCVD diamond sensor, with 500 μm thickness and 4 x 4 mm^2 electrodes, the capacitance calculates to

$$C \;=\; \varepsilon \frac{A}{d} \;=\; 1.6 \text{ pF}. \tag{6.2}$$

This is the capacitance of the diamond sensor. Including stray capacitances from the detector layout, the total capacitance is typically in the order of 10 pF. The RC time constant in a 50 Ω

system is $\tau = 0.5$ ns and $f_u = 318$ MHz. This limits the rise time t_r of a signal (10% - 90% of the pulse) to

$$t_r \;=\; 0.35 \cdot 2\pi\tau \;=\; 1.1 \text{ ns}. \tag{6.3}$$

The effect of this time constant on the rectangular current pulse of the diamond sensor was shown in Figure 5.5(a). The rectangular pulse induced by the α particle becomes exponential on the rising and falling edge. The width of the signal must be larger than 5τ, in order to reach 99% of the amplitude. If the signal is faster, a measurement error of the amplitude as well as the area will be the consequence. Therefore it is important for precise current measurements that the electronic time constant is much faster than the signal.

The time constant of the detector does not have an effect on the precision of measurements with charge amplifiers.

6.2 Current Amplification

The circuit diagram of a diamond detector being operated with a current amplifier is shown in Figure 6.1. The input impedance of a current amplifier is $R_i = 50\ \Omega$, which is the common standard in RF technology.

The input current i_d is linearly amplified by a current amplifier,

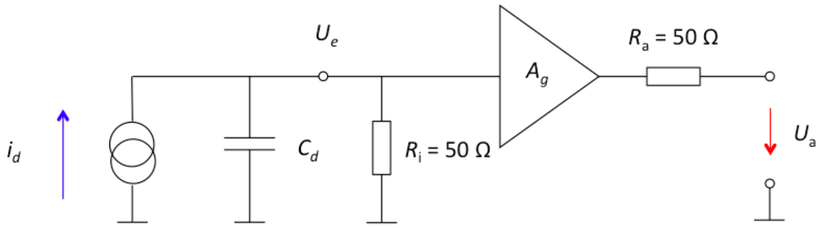

Figure 6.1: Equivalent circuit diagram of a diamond detector with capacitance C_d operated with a current amplifier in a 50 Ω system.

$$U_a \;=\; A(f) \cdot U_e \;=\; A(f) \cdot i_d \cdot 50\Omega, \tag{6.4}$$

where U_a is the output voltage of the amplifier. The current amplifier is characterized by its transfer function $A(f)$, which is ideally constant between the lower (f_l) and the upper (f_u) cut-off frequency, where the transfer function drops by -3 dB. $A(f)$ is typically given in dB,

$$A(f) \;=\; 20 \cdot \log_{10} \frac{U_a(f)}{U_e(f)} \text{ dB}. \tag{6.5}$$

The difference between the two cut-off frequencies defines the bandwidth B of the amplifier, $B \;=\; f_u - f_l$. The rise-time of a current amplifier is related to the bandwidth via the relation

$$t_r \;=\; \frac{0.35}{B}. \tag{6.6}$$

An example of a transfer function of an AC coupled current amplifier is shown in Figure 6.2.

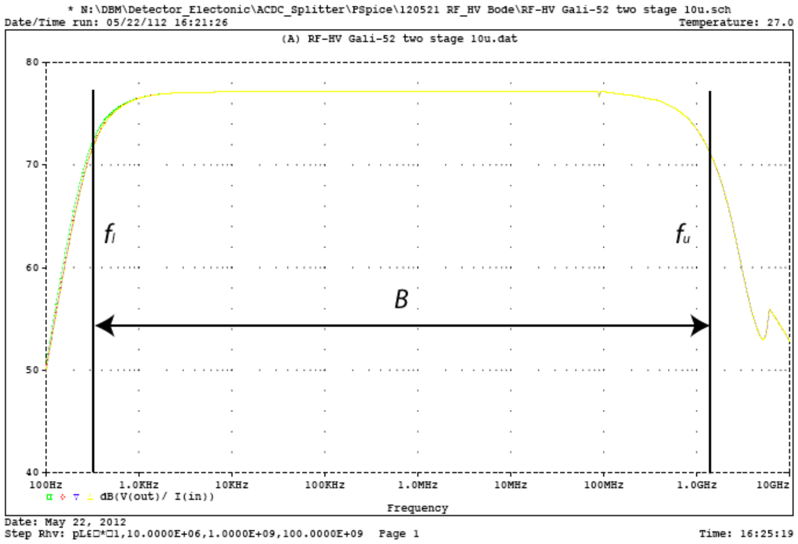

Figure 6.2: Simulated transfer function of the Cividec C2 current amplifier, picture from [93]. The cut-off frequencies f_l and f_u define the bandwidth B of the amplifier.

6.3 Charge Amplification

For spectroscopic applications charge amplifiers are used, as the achievable energy resolution is higher than for the current amplification. The induced charge in the detector Q_{in} is linearly amplified to an output voltage U_a

$$U_a = A \cdot Q_{in} = \frac{Q_{in}}{C_f}, \tag{6.7}$$

where C_f is the feedback capacitance of the charge amplifier and the gain A is given in mV/fC. The gain as well as the electronic noise of the charge amplifier is dependent on the capacitive load at the input of the amplifier. With increasing input capacitance the gain is usually decreasing and the noise is increasing.

The circuit diagram of a diamond detector with a charge amplifier is shown in Figure 6.3. The feed-back capacitance C_f integrates the charge and discharges over the feed-back resistor R_f with the time constant $\tau = R_f \cdot C_f$. In classical instrumentation amplifiers τ is in the order of μs and beyond. The output signal of the charge amplifier is a convolution of the integration and the discharging of C_f. In order to avoid an influence of the discharging on the output, the width of the input signal should be much smaller than the integration time constant of the charge amplifier itself.

In order to have a faster response, an additional shaping stage can be introduced after the charge amplifier, which provides a standard pulse shape, e.g. semi-Gaussian, where the maximum amplitude is proportional to the input charge.

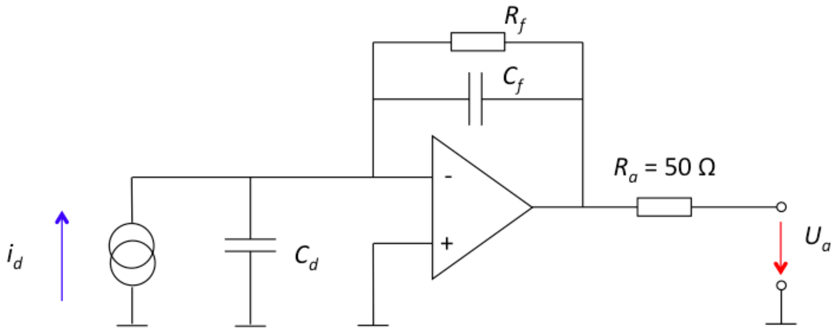

Figure 6.3: Equivalent circuit diagram of a diamond detector with capacitance C_d operated with a charge amplifier with feed-back capacitance C_f and resistor R_f in a 50 Ω system.

6.4 Noise and Resolution

The thermal motion of the charge carriers induce noise in electrical circuits. The first measurements and the theoretical background of this phenomenon were published in 1928 by Johnson [94] and Nyquist [95]. The noise voltage is dependent on the bandwidth B, the resistance R and the ambient temperature T of the system

$$U_0 = \sqrt{4k_BTBR}, \tag{6.8}$$

where k_B is the Boltzmann constant. U_0 corresponds to the open-circuit voltage of an equivalent voltage source, see Figure 6.4. This noise influences the resolution of the measurement, both in time and energy. The induced noise voltage on the measuring system U_L is given by

$$U_L = U_0 \cdot \frac{R_L}{R_L + R_i}, \tag{6.9}$$

where R_i is the detector resistance and R_L the impedance of the measuring system. The contribution of a diamond detector, with $R_i \geq 10^{14}$ Ω, to the noise level in a typically 50 Ω measuring system is hence negligible.

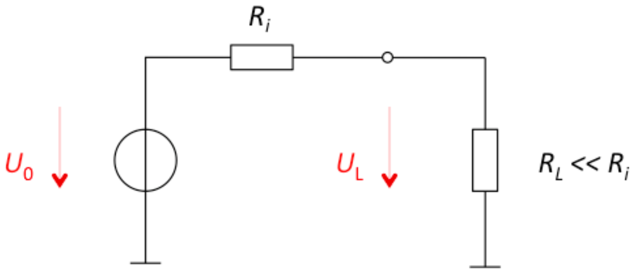

Figure 6.4: Equivalent circuit diagram of a voltage divider, which corresponds to a detector with resistance R_i read out with an oscilloscope with input impedance R_L.

Resolution in Energy Various factors influence the energy resolution of an experiment. In general the energy resolution can be written as [96]

$$\frac{dE}{E} = \frac{A}{\sqrt{E}} \oplus \frac{B}{E} \oplus C \tag{6.10}$$

where $\oplus$ indicates a quadratic sum. In the following the factors contributing to the different terms are discussed. The actual energy resolution of a measurement setup is calibrated with radioactive sources and with electronic calibration respectively.

1. Stochastic term $\frac{A}{\sqrt{E}}$: This contribution is related to the ionization process in the detector. The primary ionization follows the Poisson statistics, hence the uncertainty of the created charge carrier pairs N_{eh} is given by $\sqrt{N_{eh}} \propto \sqrt{E}$. The intrinsic energy resolution is in general better than the statistical expectation by a factor 2 to 3, which can be respected by introducing a Fano-factor $F \leq 1$ [97]. The uncertainty given by the Poisson distribution represents the maximum contribution of the ionization process to the energy resolution of the experiment.

2. Noise term $\frac{B}{E}$: This term summarizes the contribution of the electronic chain of the measurement. Two factors have to be considered:

   - Analogue noise: This is related to the baseline noise of the amplifier da. As the mean amplitude of a measured signal A is proportional to the measured deposited energy in the detector, the energy resolution is given by the amplitude resolution of the electronics

     $$\frac{dE}{E} = \frac{da}{A} = \frac{1}{\mathrm{SNR}}, \tag{6.11}$$

     where SNR is the signal-to-noise ratio. As a 'rule of thumb', for SNR ≥ 10 the signal can reliably be distinguished from the noise.
     The noise of the amplifier is, according to Equation 6.8, dependent on the bandwidth of the system. Current amplifiers have in general a larger bandwidth than charge amplifiers, which have therefore a better energy resolution. For charge amplifiers the noise level rises with increasing input capacitance, which worsens the resolution. This can be optimized with the design of the detector.

   - Quantization noise: The analog-to-digital converter (ADC) of the DAQ system limits the energy resolution of the experiment, dependent on the number of ADC-bits N_{bit} and the full range A_{fr} of the measurement

     $$da_{\mathrm{ADC}} = \frac{A_{fr}}{\sqrt{12} \cdot (2^{N_{bit}} - 1)}. \tag{6.12}$$

     For spectroscopic measurements the usage of a high-resolution ADC is preferable.

   The amplitude resolution of an experiment can be enhanced by means of pulse shape fitting and refined pulse integration methods. The application of digital filters (e.g. FIR filters) to the data can enhance the resolution, dependent on the amplitude of the signals, up to a factor 4 [98].

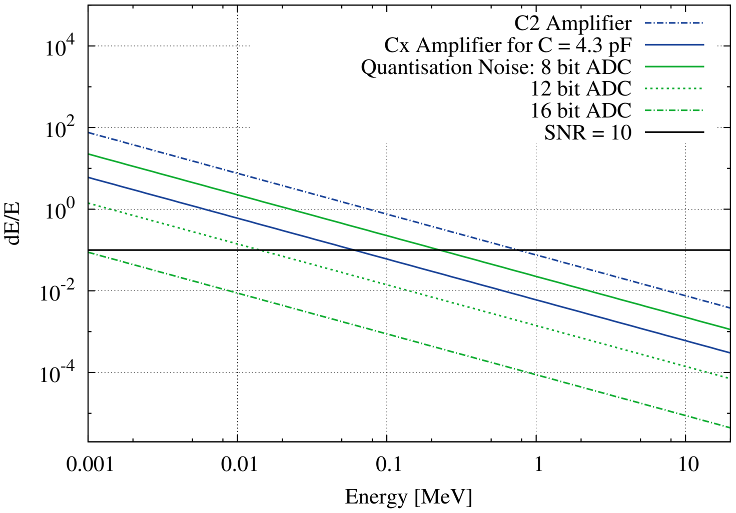

Figure 6.5: Different factors influencing the energy resolution of an experiment. The contribution of the used electronics is shown on the example of the Cividec C2 2 GHz current amplifier and the Cividec Cx spectroscopic charge amplifier [99]. The influence of different ADCs is drawn in green. For $\Delta E/E \leq 0.1$, equivalent to SNR $\geq$ 10, a reliable measurement can be performed.

In Figure 6.5 the contribution to the energy resolution of electronics and ADC are shown for particle energies 1 keV $\leq$ E $\leq$ 20 MeV. The influence of the ADC on the energy resolution for different numbers of bits are shown in green. The two types of amplifiers with which the DM-D was operated are shown in blue. For diamond detectors of 150 μm thickness the Cividec C2 2 GHz current amplifier can reliably be used, with SNR $\geq$ 10, for particle energies E $\geq$ 600 keV. The Cividec Cx spectroscopic amplifier is suited for particle energies above 80 keV, given an input capacitance of $C = 4.3$ pF. The energy resolution of this amplifier worsens with increasing capacitive load.

3. Constant term C: Systematic uncertainties are summarized in the constant term to the energy resolution. The efficiency of the detector and the experimental setup, like the source of the particles or different materials and their homogeneity on the path of the particles to the detector, minimize the achievable resolution. Some of these effects, for example the thickness of the electrodes on a diamond detector, can be quantified by means of Monte-Carlo simulations.
   More difficult to judge are imperfections in the experimental setup, like varying thickness of the detector or the electrodes, and border-effects, where an incident particle hits the diamond detector on the edge. In this case, only part of the energy of the incident particle will be deposited in the active volume of the detector.
   The respective uncertainty of such effects on the final error of the measured cross-section can be minimized when measuring the desired cross-section with respect to a standard one, as was the case for the measurement with the DM-D at n_TOF. The ^{59}Ni(n,α) cross-section was measured with respect to ^{6}Li(n,α).

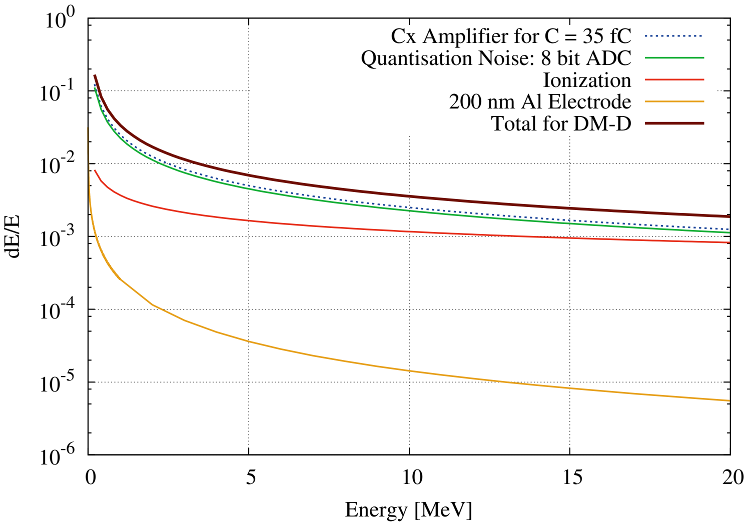

Figure 6.6: Different factors influencing the energy resolution of the measurements with the DM-D. The input capacitance on the Cividec Cx amplifiers was about 35 fC. The data was recorded with an 8 bit ADC. The statistical uncertainty coming from the ionization process in the diamond detector (red) and the effect of the Al-electrodes of the DM-D (yellow) are less important than the electronics and the ADC.

In Figure 6.6 the different contributions to the energy resolution for the measurements with the DM-D are shown for the energy interval of interest 1 MeV $\leq$ E $\leq$ 20 MeV. An 8 bit ADC-DAQ was used for all measurements. The input capacitance on the Cx amplifiers during the measurement at n_TOF was about 35 pF, dominated by the cables connecting the detector in the vacuum chamber to the amplifiers via feed-throughs. The energy resolution for the measurement at n_TOF was equally limited by the electronics and the DAQ. The statistical uncertainty of the ionization process in the diamond sensors and the effect of the 200 nm Al electrodes play a minor role. The resulting energy resolution for the DM-D, under the assumption of a 100% efficiency of the diamond sensors, is shown in dark red. The resolution of the measurement was enhanced by the offline data analysis, which used a pulse shape fitting routine. An energy resolution of $dE = 35$ keV was achieved.

Resolution in Time The arrival time of the signal has to be determined precisely at time-of-flight measurements. The position of maximum slope of the rising edge is used, which is in Gaussian-like pulses typically at 50% of the maximum amplitude. For constant arrival times a time jitter occurs, which is related to the base-line noise. The relation between this time jitter and the base-line noise is given by

$$dt \;=\; t \cdot \frac{dA}{A} \;=\; \frac{t}{\mathrm{SNR}}, \tag{6.13}$$

where $\frac{A}{t}$ is the slope of the signal. The time resolution enhances with increasing SNR, thus with increasing amplitude and decreasing base-line noise or with increasing slope. With refined offline

pulse shape analysis methods, the time resolution can be enhanced.
In order to avoid limiting effects by the ADC, a sufficiently high sampling frequency and bit resolution has to be used. For CVD diamond detectors a time resolution of $dt = (14.7 \pm 1.7)$ ps was achieved at the CNGS facility at CERN [70]. In this case the limiting factor was the 8-bit amplitude resolution of the ADC and not the diamond detector.

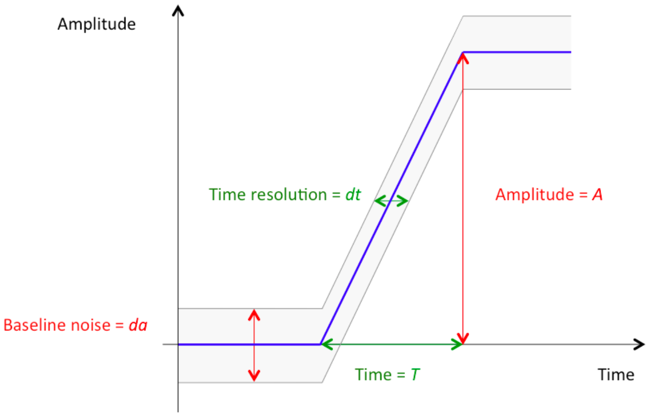

Figure 6.7: Rising edge of a signal; the noise level da is equivalent to the amplitude resolution and influences the time resolution dt of the measurement.

6.5 Calibration of Electronics

For precise measurements it is necessary to know the influence of the electronics to the measurement results. Knowledge about linearity, dynamic range, gain, noise and the influence of other parameters, like the input capacitance to a charge amplifier, is necessary. Therefore an electronic calibration of the amplifiers has to be performed.

Current Amplifier The calibration of a current amplifier is performed with a calibration current pulse. The pulse shape should be as close as possible to the physical detector signal. In Figure 6.8 a schematic of the calibration setup is shown. A voltage step U_{cal} from a pulser is differentiated on a forming capacitance C_{cal}. The resulting pulse serves as the reference. The amplifier input signal is attenuated.
For this calibration it is most important that the rise time of the voltage jump is very fast, with $t_r < 200$ ps for diamond detectors, and that the step has a linear shape. Steps with oscillations are not suited for the calibration of current amplifiers.
The baseline noise and the gain are measured together with the rise-time of the amplified pulse. The rise time of the current amplifier gives according to Equation 6.6 the upper cut-off frequency f_u. The linearity of the amplifier is measured by varying the attenuation.
This calibration allows to characterize the current amplifier for the application with a specific detector. A full characterization requires the measurement of the transfer function.

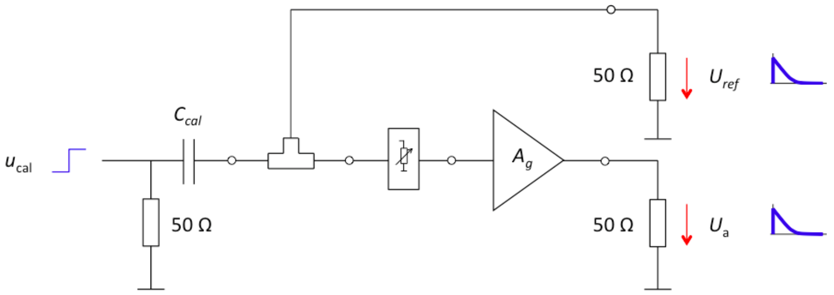

Figure 6.8: Schematics for the calibration of a current amplifier. The fast voltage jump U_{cal} is differentiated on a forming capacitance C_{cal}. The resulting pulse shape is measured as a reference. After attenuation, the current pulse is used for calibration.

Charge Amplifier Charge amplifiers are calibrated with a calibration charge Q_{cal}. In Figure 6.9 the schematics for this calibration is shown. A voltage step U_{cal} on a calibration capacitance C_{cal} gives the calibration charge

$$Q_{cal} \;=\; C_{cal} \cdot U_{cal}. \tag{6.14}$$

U_{cal} and C_{cal} have to be precisely know. The rise time of the voltage jump does not need to be as fast as for the current amplifier, but should be matched to the time constant of the charge amplifier.

Dividing the maximum amplitude of the amplifier output signal U_a by Q_{cal} gives the gain in

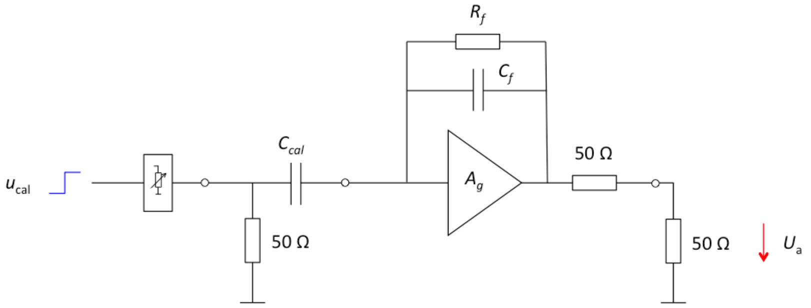

Figure 6.9: Schematics for the calibration of a charge amplifier. The voltage step U_{cal} and the capacitance C_{cal} define the calibration charge Q_{cal}.The amplitude of the output signal compared to Q_{cal} gives the gain of the charge amplifier.

mV/fC. As the response of a charge amplifier is dependent on the capacitive load, the characterization should be performed at the working point. To measure the amplitude linearity of the amplifier, different attenuations are introduced before the capacitance. C_{cal} should be directly connected to the amplifier input, in order to avoid additional capacitive load. The baseline noise, the timing properties and the gain are measured at each step.

The Cividec Amplifiers The fast current amplifier and the spectroscopic charge amplifier from Cividec Instrumentation GmbH were electronically calibrated. The results are listed below. The calibration of the individual amplifiers used for the measurement with the DM-D at n_TOF is given in Chapter 8.

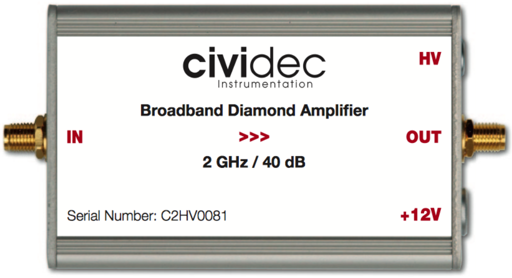
cividec
Instrumentation
HV
Broadband Diamond Amplifier
IN
>>>
OUT
2 GHz / 40 dB
Serial Number: C2HV0081
+12V

Cividec C2
Broadband amplifier.

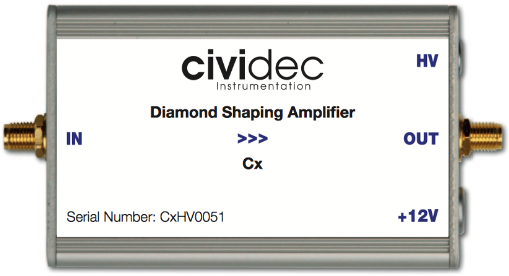
cividec
Instrumentation
HV
Diamond Shaping Amplifier
IN
>>>
OUT
Cx
Serial Number: CxHV0051
+12V

Cividec Cx
Spectroscopic shaping amplifier.

Gain	40.9 dB
Polarity	Non-inverting, bipolar
Linear output voltage range	±1 V
RMS noise	2.5 mV
f_u	2 GHz
f_l	1 MHz
t_r	185 ps
FWHM	250 ps

Gain	8 mV/fC
Polarity	Inverting, unipolar
Linear output voltage range	+2 V
ENC noise	(300 + 40/pF) e^-
SNR (@ 4.3 pF)	14.1/fC
Pulse shape	Gaussian
t_r	92 ns
FWHM	180 ns

Part II

The Diamond Mosaic-Detector

In this second part of the thesis the Diamond Mosaic Detector (DM-D), which was build in the framework of this PhD, is introduced.
The design of the detector, considering all design constraints, and the production process of the detector are described in the first chapter.
The calibration of the electronics, which was adapted to the needs for the measurement at n_TOF, is described in the second chapter.
The current-over-voltage behaviour of the individual diamond diodes, which were mounted in a 3 x 3 mosaic on the detector, and the characterization of the sensors with α sources are given in the third chapter.
The concluding chapter summarizes this second part and gives information on the outcome of the characterization of the DM-D and whether the design constraints were fulfilled with the final detector.

Chapter 7

Design and Production

The Diamond Mosaic-Detector (DM-D) was developed for (n,α) cross-section measurements at n_TOF. Due to the necessity of using thin samples and as (n,α) reactions often feature small cross-sections, the detector was to be placed intercepting the neutron beam.

Single-crystal chemical vapor deposition (sCVD) diamond was chosen as detector material for its spectroscopic properties, radiation hardness, its insensitivity to γ-rays and its robustness. Diamond detectors do not induce noise, can be operated at room temperature and without shading, which significantly simplifies the detector layout. The absence of dopants yielding exothermic (n,cp) reaction channels, like ^{10}B, was an additional argument to use diamond as detector material. In ^{12}C the first neutron-induced reaction channel yielding a charged particle opens only at high neutron energies ($E_n > 6$ MeV), which is favourable for measurements in a neutron beam.

The advantage of diamond detectors, where background rejection can be performed using pulse-shape analysis, was not used with the DM-D, but is currently investigated for future applications in (n,cp) measurements [89].

The design constraints for the DM-D were the following:

- Adapt the active area of the detector to the size of the sample for the cross-section measurement (15 mm diameter for the ^{59}Ni sample).
- Minimize the material budget in the neutron beam.
- Avoid material that can be activated in the neutron beam (e.g. Au).
- Ensure high-resolution α spectroscopy up to an energy of $E_\alpha = 20$ MeV.
- Ensure that the sample in front of the detector is easily exchangeable.
- Ensure a 2 GHz RF-shielding.
- Ensure the vacuum compatibility of the detector.

As the maximum available size for sCVD diamond diodes is 4.7 mm x 4.7 mm, a mosaic had to be constructed out of several diodes, to increase the detectors active area. In Figure 7.1 a close-up picture of the front side of the DM-D, which was facing the neutron beam during the experiment, is shown. The detector consists of eight sCVD and one DOI diamond diodes, arranged in a 3 x 3 array. The detector channels, as seen by the neutron beam, were named in the following way:

DIAM8 sCVD 4.1 x 4.1 x 0.15 [mm^3]	**DIAM1** sCVD 4.5 x 4.8 x 0.15 [mm^3]	**DIAM9** sCVD 4.0 x 4.0 x 0.15 [mm^3]
DIAM3 sCVD 4.4 x 4.4 x 0.15 [mm^3]	**DIAM4** sCVD 4.4 x 4.4 x 0.15 [mm^3]	**DIAM5** sCVD 4.4 x 4.4 x 0.15 [mm^3]
DOID DOI 4.6 x 4.6 x 0.15 [mm^3]	**DIAM2** sCVD 4.7 x 4.4 x 0.15 [mm^3]	**DIAM6** sCVD 3.8 x 3.8 x 0.15 [mm^3]

The individual sizes of the diamonds and the respective material are listed below the names. The total active area of the DM-D is 169 mm^2, a square of approximately 13.2 mm x 12.8 mm. The DOI diode was included to test whether this material is suited to be used for (n,cp) measurements at n_TOF, as this material is the only promising candidate for future large area spectroscopic diamond detectors.

The sample for the cross-section measurement is mounted using the positioning pin and pressed against the printed circuit board (PCB)-structure using two clamps.

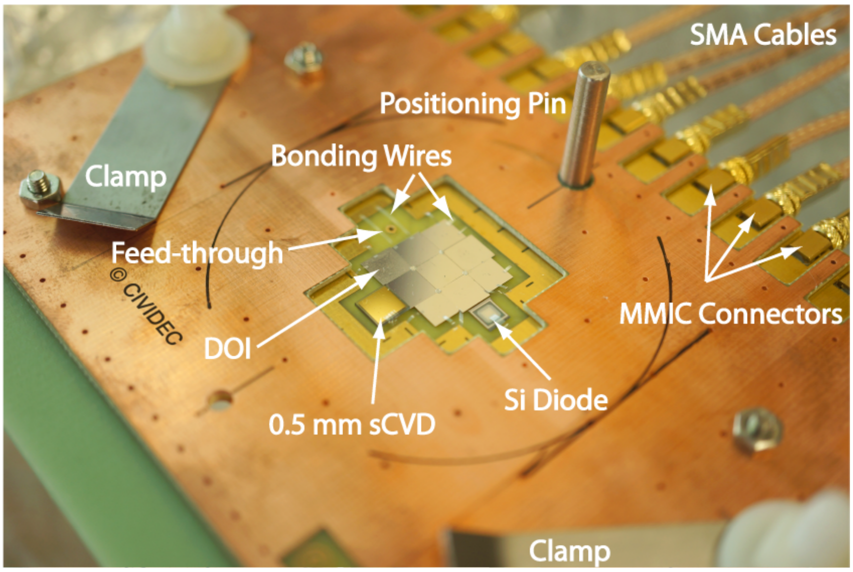

Figure 7.1: The Diamond Mosaic-Detector.

An additional 500 μm sCVD diamond and a 100 μm Si diode were mounted, to perform background measurements in the n_TOF neutron beam. In Table A.2 detailed information (size, material, ID) is given for all diodes in their geometrical arrangement on the DM-D.

The detailed design description and the production process of the DM-D can be found in the following sections.

7.1 The Diamonds

The sCVD diamond substrates were produced by Element Six Inc. [57]. The specified crystal orientation is $\{100\}$ on the faces and $< 110 >$ on the edges with a $\pm 3^{\circ}$ crystallographic orientation. The specified impurities are N < 5 ppb and B < 1 ppb.
The diamond thickness was chosen to be 150 μm, in order to provide α-spectroscopy up to an α-energy of 20 MeV and still enhance the signal-to-background ratio in the neutron beam. The diamond substrates were polished by Diamond Detectors Limited (DDL) [100], with an arithmetic average roughness of $R_a < 5$ nm. The dimensions of all the diamonds can be seen in Table A.2.
Some of the diamonds had chipped-off edges or cracks due to the polishing to the specified thickness, as is shown in Figure 7.2. Due to time and availability constraints, the received set of 9 sCVD diamonds by DDL was used for the DM-D. One of the substrates broke along a crack during metallization and was later replaced by the DOI diode, which was planned to be positioned on the left hand side of DIAM3, on the spare place of the main DM-D PCB.

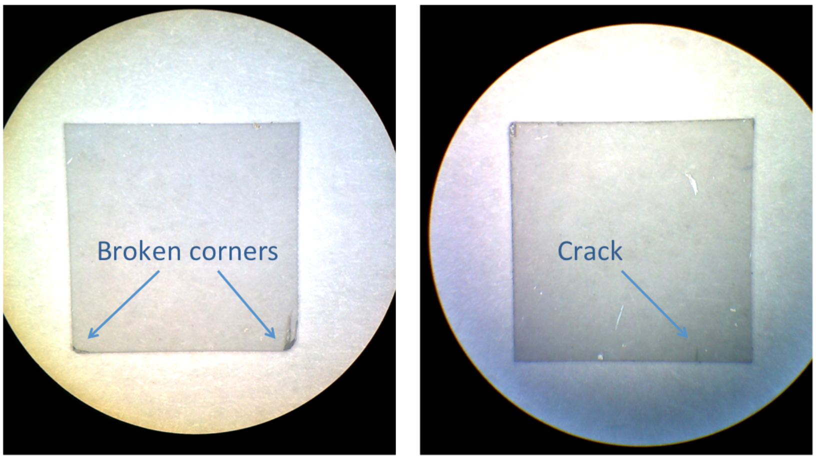

Figure 7.2: Two Diamonds as received by DDL, photos taken under the microscope (x10). Some of the diamonds had chipped off corners or cracks.

7.2 Metallization of the Diamonds

The diamond substrates were metallized at the Laboratoire Capteurs Diamant at CEA Saclay [101] in collaboration with M. Pomorski.
The diamond substrates were cleaned and metallized with 200 nm Al. Aluminium was chosen to avoid an activation of the detector in the neutron beam, to minimize the energy loss of α-particles in the electrodes and to avoid additional resonant background from capture reactions in the electrode material during the measurement in the neutron beam. The thickness was chosen

to be 200 nm to ensure that a bonding connection can be made with the electrodes. The resulting diamond diodes were glued and bonded to a PCB structure.
In the following the three steps of the metallization process are briefly discussed.

1. Cleaning Before the metallization, the surface of the diamonds needs to be cleaned. Organic layers and possible graphite layers have to be removed by a treatment with acids, in order to ensure a good diamond-metal connection.
The diamond substrates for the DM-D were first left in a boiling, saturated $H_2SO_4 + KNO_3$ solution for two hours. This removes organic layers on the surface by oxidation and etches graphite. To remove any recrystallized KNO_3, the diamonds were once again put into pure, boiling H_2SO_4. The diamonds were subsequently treated with boiling $3HCl+HNO_3$, which is strongly oxidizing and chlorates the surface, to support the diamond-metal connection. Finally the diamonds were rinsed with deionized water and dried with Ar gas in the clean room.

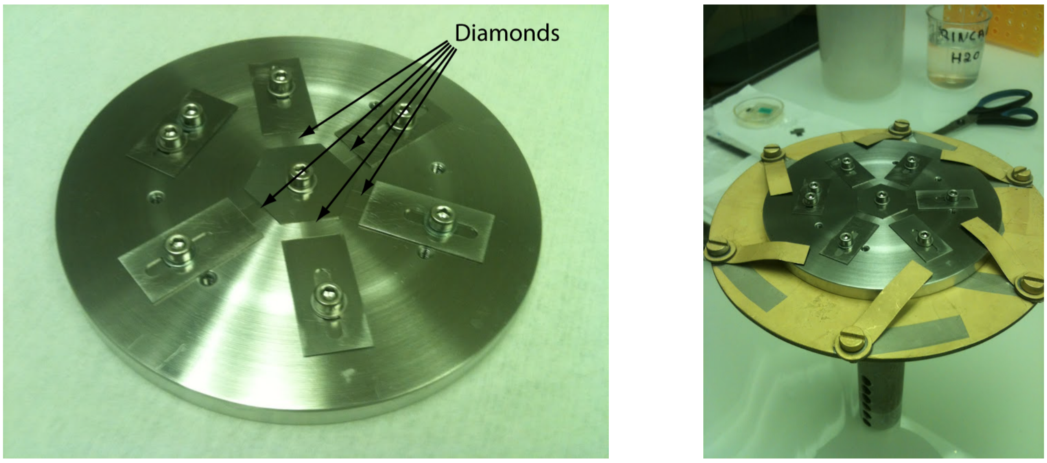

(a) DIAM1 - DIAM5 mounted for metallization.

(b) Final setup for the e^--beam machine.

Figure 7.3: Mounting of DIAM1-DIAM5 for metallization.

2. Metallization The diamonds were metallized in an e^--beam machine with pure Al as target. In order to have the full area of the diamond diodes as active area of the DM-D, the diamonds needed to be fully metallized on both sides before the Lithography. A special holder for the mounting in the e^--beam machine was designed where the diamond substrates are clamped between two slightly angled faces, to ensure a maximum possible exposure of the diamond area to the Al vapor during metallization. The holder was constructed at the EN-STI-TCD workshop at CERN, see Figure 7.3(a).
In Figure 7.3(b) the final setup on the sample holder for the e^--beam machine is shown. This support was mounted up-side-down in the machine. The evaporation of Al was performed at a pressure of less than 10^{-8} mbar. In a second step, the diamonds were turned around in the clean room and metallized on the second side. The 8 sCVD diamonds and the DOI diamond

were metallized in two separate runs.

3. Photolithography After the metallization, a photolithography was performed for each of the diamonds on one side, in order to produce a diamond diode which can be used as a detector. This process allows to remove unwanted layers of material following a geometrical pattern, by using a light-sensitive resin and an optical-mask.

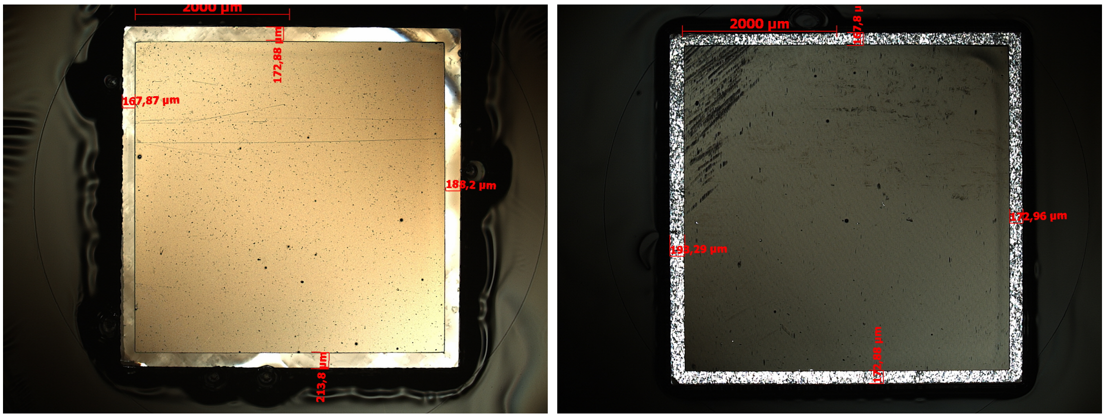

(a) DIAM5.

(b) DOI.

Figure 7.4: Diamonds after the lithography, both pictures were taken with a cross-polarizer.

For the photolithography of the DM-D diodes, the resin NLOF2000 was used. This resin is used for the negative process, where the resin exposed to UV light hardens and the part that is shadowed during the exposure is removed by the developer and the metal underneath is etched away.

The electrodes were made in such a way that an unmetallized border of about 200 μm was left to the edge of the diamonds. If the resulting diode had a leakage current that exceeded 1 nA at HV = 1 V/μm, the lithography was performed once again, with an increased distance to the edges. DIAM1 and DIAM2 were cleaned and re-metallized after the first Lithography, as the leakage current of the resulting diodes was too high for a stable operation as a detector. In Figure 7.4 the resulting electrode for DIAM5 and DOID can be seen exemplary. The pictures were taken with crossed polarizers under the microscope.

7.3 PCB Design

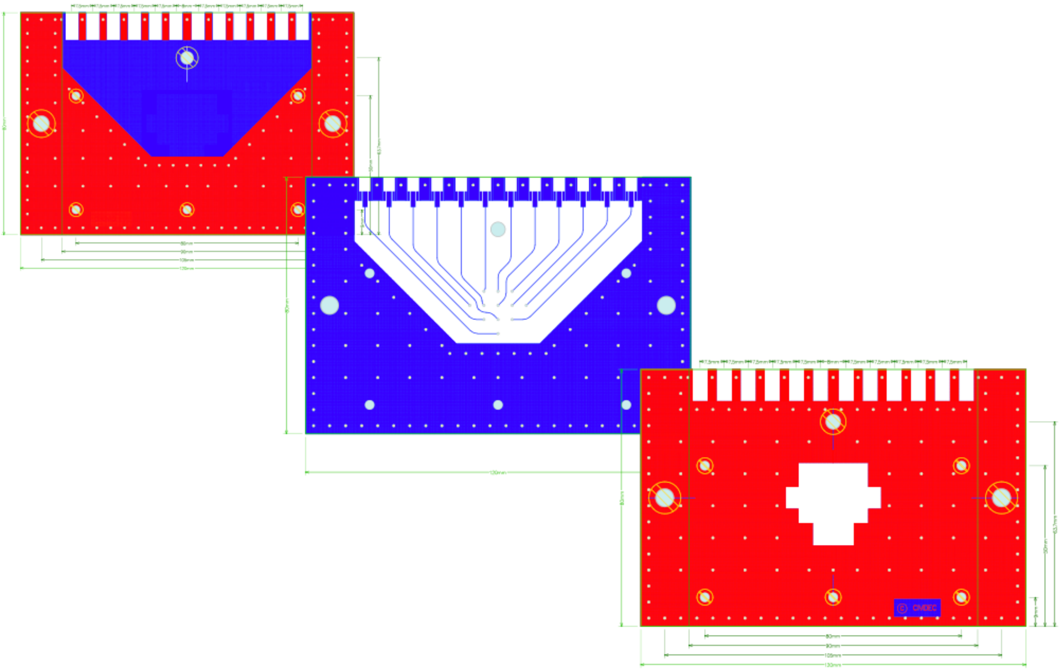

Figure 7.5: Technical drawings of the three PCB plates of the DM-D[1]*, which are screwed together via the indicated holes. The colors indicate the metallization on the back (blue) and front (red) side. The back PCB on the left has recesses for MMIC connectors and is unmetallized on the front side, where it touches the read-out lines of the main PCB. The main PCB in the middle is shown only from the back side to show the read-out lines and the soldering pads for the MMIC connectors. The front PCB, which acts as a spacer between the diodes and the sample has recesses for the MMIC connectors and a hole in the middle for the diodes and the bonding wires. It is fully metallized on both sides.*

The printed circuit board structure for the DM-D was designed under the following considerations:

- Minimum material budget in the neutron beam.
- Minimum capacitance of the channels in order to optimize for the SNR of the spectroscopic amplifiers.
- Impedance of the read-out lines Z = 50 Ω.
- RF-shielding for the read-out with a 2 GHz current amplifier.
- Possibility to position the sample in close geometry to the diodes, avoiding a short circuit and not influencing the capacitance of the channels.
- Mechanical stability.

---

[1] Courtesy of G. Ehrlich-Joop

A stack of 3 PCBs, which is tightly screwed together, was chosen to ensure all of the above mentioned points. For the design of the detector, special care was taken to ensure a good radio-frequency (RF) shielding up to 2 GHz. A compromise had to be found for the first two points, as the capacitance decreases with increasing thickness of material.

The main (middle) PCB, on which the diodes were mounted, is 0.5 mm thick. It is metallized with 5 μm Ni, 17 μm Cu and coated with 10 nm Au, in order to ensure the bondability. This PCB has a feed-through for each of the diodes and individual read-out lines on the rear side, see Figure 7.5. The diodes were mounted on the front side of the PCB. The fully metallized sides of the diodes, which were facing the sample, were interconnected to ground on the front side of this PCB. The bias voltage is applied on the rear side via the read-out line. 50 Ω MMIC coaxial connectors are used to connect cables or directly the amplifier.

The back PCB is 0.5 mm thick and metallized with 35 μm Cu. It acts as shielding for the read-out lines and has no metallization in the part of the front side, where it touches the read-out lines of the main PCB. The main PCB in close contact with this back PCB makes a Faraday cage which provides a 2 GHz RF-shielding.

The front PCB is 1 mm thick and fully metallized with 35 μm Cu. It is needed as spacer between the diodes and their bonding wires and the sample, which is pressed against this PCB. It has a hole in the middle for the diodes and bonding wires, see Figures 7.1 and 7.5, as well as recesses for the MMIC connectors.

7.4 Mounting

The diodes were glued and bonded at the CERN bonding laboratory. 75 μm thick Staystick Thermoplastic re-workable adhesive was used as glue for the diodes. This glue is mouldable when heated up and solidifies when cooled down to room temperature.
Square pieces of glue, matched to the size of the feed-throughs, were positioned on the PCB, see Figure 7.6(a), and adjusted whilst heating up. The diodes were positioned on the PCB and fixed to their position whilst heating up and putting pressure on their surface, see Figure 7.6(b). Then the diodes were bonded on the front side, see Figure 7.6(c). The diode in the middle of the PCB was connected to the neighbouring diodes by small pieces of glue on the corners, to ensure a good grounding on the front side of the detector.

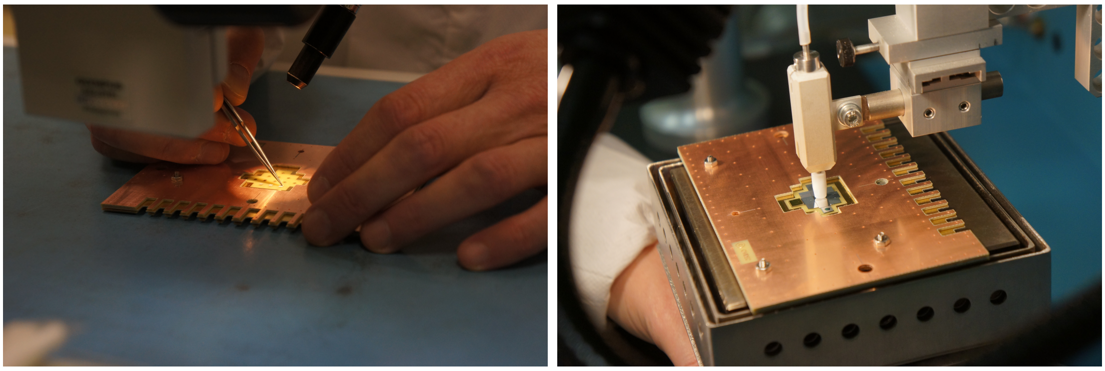

(a) Positioning of the glue.

(b) Positioning of the diodes under pressure whilst heating up the glue.

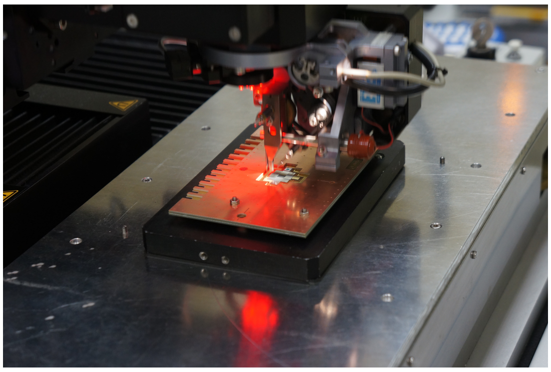

(c) Bonding of the diodes to the PCB.

Figure 7.6: Glueing and bonding of the DM-D.

Chapter 8

Characterization of the dedicated Electronics

For the measurements at n_TOF, spectroscopic shaping amplifiers by CIVIDEC Instrumentation GmbH (CIVIDEC Cx-Series) were used for all channels with sCVD diodes (channels named DIAM). The amplifiers are unipolar, with a linear amplification for positive output and negative input respectively, up to a maximum output voltage of +2 V. This requires a positive bias voltage for the DM-D, corresponding to e^- read-out. The gain of the amplifiers, with $A \approx 8$ mV/fC, were optimized for a measurement of a maximum deposited energy of $E_{max} = 20$ MeV in diamond diodes, which corresponds to a deposited charge of $Q_{in} = 240$ fC.
The DOI diode (DOID channel of the DM-D) only showed spectroscopic properties for the read-out of holes. This diode was therefore operated with negative voltage, which prevented the use of the spectroscopic shaping amplifiers. The DOID was amplified with a bipolar, 2 GHz broadband current amplifier by CIVIDEC Instrumentation GmbH (CIVIDEC C2-Series).
All amplifiers were calibrated individually, following the procedure described in Section 6.5, prior to the measurements. The individual gains were used in the data analysis of the experiments.
During the measurement at n_TOF the DM-D was used inside a vacuum chamber, with cables of approximately 20 cm length and a vacuum feedthrough before the amplifiers. The resulting capacitances for the DM-D channels were in the range of 33.9 pF - 36.8 pF.
The configuration of the DM-D channels are listed in Table 8.1, arranged as the DM-D is seen from the neutron beam. The bias voltage, the measured capacitance, the name of the individual amplifier and the corresponding gain are given for each channel.

Table 8.1: Bias voltage, capacitance and corresponding amplifier for each channel of the Diamond Mosaic-Detector during the measurement at n_ TOF.

DIAM8 HV = 60 V Capacitance = 34.3 pF Amplifier: CIVIDEC CxHV0040 Gain = 8.01 mV/fC	**DIAM1** HV = 75 V Capacitance = 34.8 pF Amplifier: CIVIDEC CxHV0033 Gain = 8.09 mV/fC	**DIAM9** HV = 150 V Capacitance = 33.9 pF Amplifier: CIVIDEC CxHV0041 Gain = 8.01 mV/fC
DIAM3 HV = 150 V Capacitance = 35.1 pF Amplifier: CIVIDEC CxHV0035 Gain = 7.80 mV/fC	**DIAM4** HV = 150 V Capacitance = 36.1 pF Amplifier: CIVIDEC CxHV0036 Gain = 8.05 mV/fC	**DIAM5** HV = 150 V Capacitance = 36.2 pF Amplifier: CIVIDEC CxHV0037 Gain = 8.05 mV/fC
DOID HV = -150 V Capacitance = 36.8 pF Amplifier: CIVIDEC C2HV0091 Gain = 40.9 dB	**DIAM2** HV = 150 V Capacitance = 36.1 pF Amplifier: CIVIDEC CxHV0034 Gain = 7.89 mV/fC	**DIAM6** HV = 120 V Capacitance = 35.7 pF Amplifier: CIVIDEC CxHV0038 Gain = 8.08 mV/fC

Spectroscopic Shaping Amplifiers The CIVIDEC Cx-amplifiers provide a Gaussian pulse shape with a full width at half maximum of FWHM = 180 ns. The amplifiers are unipolar and inverting with a linear range of +2 V. The response of the amplifier is dependent on the capacitive load, where the noise increases with increasing input capacitance. The SNR therefore decreases as a function of the capacitive load.

The SNR per 1 MeV deposited energy in diamond as a function of the capacitive load for the Cx-amplifiers is shown in Figure 8.1. Due to the use of long cables inside the vacuum chamber, the working point for the DM-D channels was around 35 pF. At this working point the SNR/MeV = 40, which gives an energy resolution of $dE = 25$ keV in diamond and a minimum trigger level of 250 keV. In spectroscopic measurements, particle spectra which are 3σ apart are usually distinguishable. The SNR for the measurements with the DM-D allows hence the discrimination of particle spectra which are 75 keV apart. The closest lines in the ^{59}Ni measurement were separated by 670 keV (α and triton of ^{6}Li), which confirms that the SNR is more than sufficient for a reliable cross-section measurement. The average pulse shapes of all used Cx amplifiers for $Q_{cal} = 23.5$ fC are displayed in Figure 9.2(a). The rise-time (10%-90%) of the Gaussian pulses is $t_r = 92$ ns. The time resolution dt, which is defined by

$$dt = \frac{t_r}{SNR}, \tag{8.1}$$

is $dt = 2.3$ ns at 1 MeV deposited energy. This is by far sufficient for measurements at n_TOF, where the neutron energy is determined by the arrival time of the signal. The neutron energy resolution dE_n for the measurements with the DM-D is dominated by the resolution function at

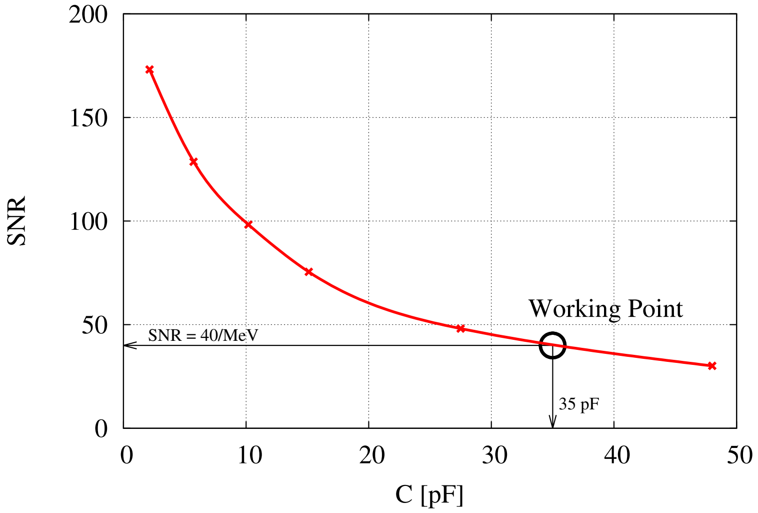

Figure 8.1: SNR per 1 MeV deposited energy in diamond as a function of the input capacitance C for the CIVIDEC Cx-amplifiers. The working point of the DM-D is indicated at 35 pF, where SNR = 40/MeV. The calibration charge was Q_{cal} = 12 fC, which corresponds to 1 MeV in diamond.

n_TOF. The amplifiers have a negligible effect on dE_n.
The linearity of the used Cx-amplifiers is shown in Figure 9.2(b). The individual gains, matched to the capacitive load of the respective channel, are listed in Table 8.1.

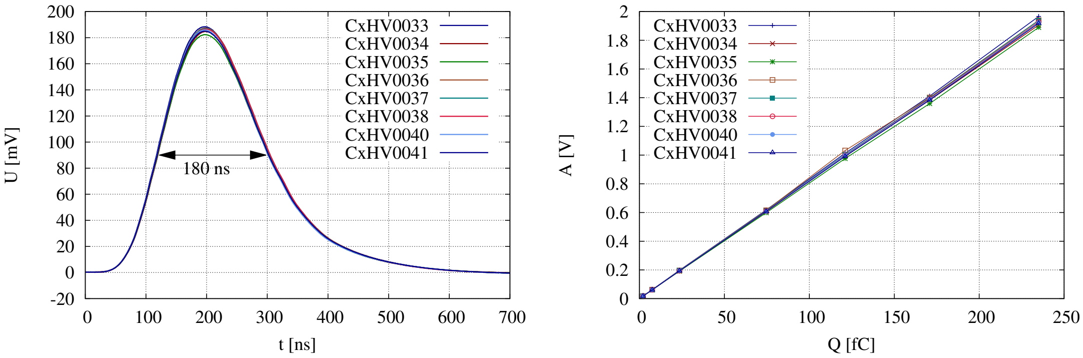

(a) Average pulse shape for $Q_{cal} = 23.5$ fC.

(b) Linearity of the amplifiers.

Figure 8.2: Characterization of the CIVIDEC CX-amplifiers used with the DM-D.

Broadband Current Amplifier The CIVIDEC C2 current amplifier was calibrated with a fast pulser, providing a voltage step with a rise time of 230 ps. The step was differentiated on a forming capacitance of 3.3 pF, providing a rise time of the calibration pulse of $t_{r,cal} = 287$ ps. Figure 8.3 shows the calibration measurement performed with a digital oscilloscope. The voltage step is displayed on the top in black. The differentiated calibration pulse in red was attenuated with 40 dB. It is directly comparable with the output of the current amplifier in blue.

The noise level of the amplifier is $\sigma = 2.5$ mV. This gives a minimum trigger level for 150 μm diamonds of 760 keV deposited energy. This is sufficient for the measurements performed at n_TOF, where the particle energies of interest were above 1 MeV. The corresponding energy resolution allows to easily distinguish the expected particle spectra at the ^{59}Ni measurement. The SNR of this amplifier is not dependent on the capacitive load and linearly dependent on the amplitude of the recorded signals.

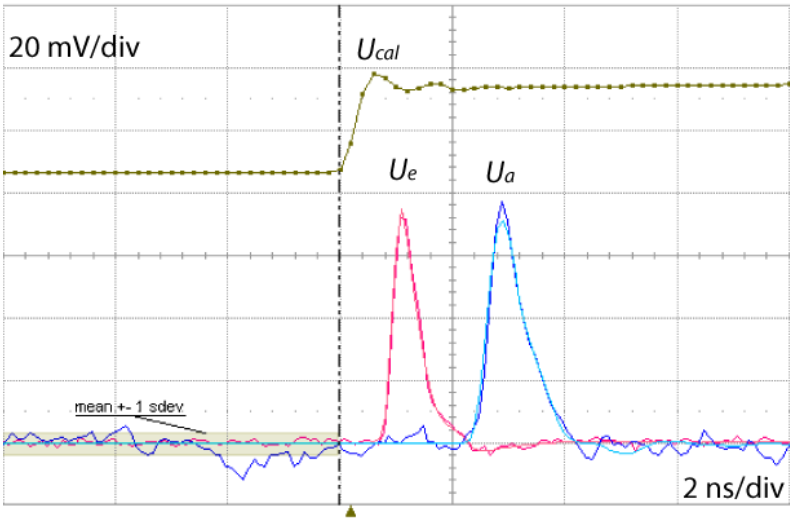

Figure 8.3: Calibration of the CIVIDEC C2 broadband current amplifier.

The rise time of the amplifier is $t_r = 385$ ps and the pulse has a width of FWHM = 766 ps, measured with a digital oscilloscope with a nominal analogue bandwidth of 2 GHz. With these timing properties a measurement at n_TOF at the highest neutron energies is possible. It allowed the measurement of the γ-flash which was presented in Figure 2.8, where the footage of the proton beam in the experimental area was recorded.

The gain of the amplifier is 112, corresponding to 40.9 dB and being well suited for a measurement of single α particles in the MeV range. The amplifier has a linear amplification in the output voltage range from -1V to +1V.

Chapter 9

Characterization of the DM-D Channels

The DM-D was primarily built for α-spectroscopy. But also other particles, given sufficient energy, can escape the sample when measuring in a neutron beam. The following reaction products were measured during the ^{59}Ni(n,α)^{56}Fe campaign at n_TOF with the DM-D:

Reaction	Particle Energy [MeV]
^{59}Ni(n,α)^{56}Fe	$E_\alpha = 4.76$
^{6}Li(n,α)^{3}H	$E_\alpha = 2.06$
	$E_t = 2.73$

The particle energy corresponds to the maximum kinetic energy of the reaction products. In the ^{6}Li(n,α)^{3}H reaction, the tritons (^{3}H) are higher in energy and hence their signals are used for the determination of the neutron flux.

In order to understand and determine the range of energies for which the DM-D offers spectroscopic performance, the deposited energy dE of light particles in a diamond of 150 μm thickness is shown as a function of the particle energy E in Figure 9.1. The total kinetic energy will be deposited in the volume of the diamond by α-particles up to an energy of 22 MeV, tritons up to 9 MeV and protons up to 6 MeV. The quoted energies are the respective upper limits for spectroscopic measurements with the DM-D. Electrons can be measured spectroscopically up to an energy of 200 keV with the DM-D.

The lower limit for a spectroscopic measurement is given by the noise level, which is 25 keV for the DIAM-channels of the DM-D, see Section 8. When a threshold trigger is used for the measurement, the lower limit increases with a reliable trigger level of 5σ to E_{th} =125 keV.

Prior to the measurement at n_TOF the diamonds of the DM-D were tested for their current-over-voltage behaviour. The charge gain as a function of the electric field was measured with a sealed ^{241}Am source and the energy resolution of the different channels was measured with an unsealed α source, containing four different radioactive isotopes. The charge yield per 1 MeV deposited energy, as a function of the penetration depth of all charged particles measured with

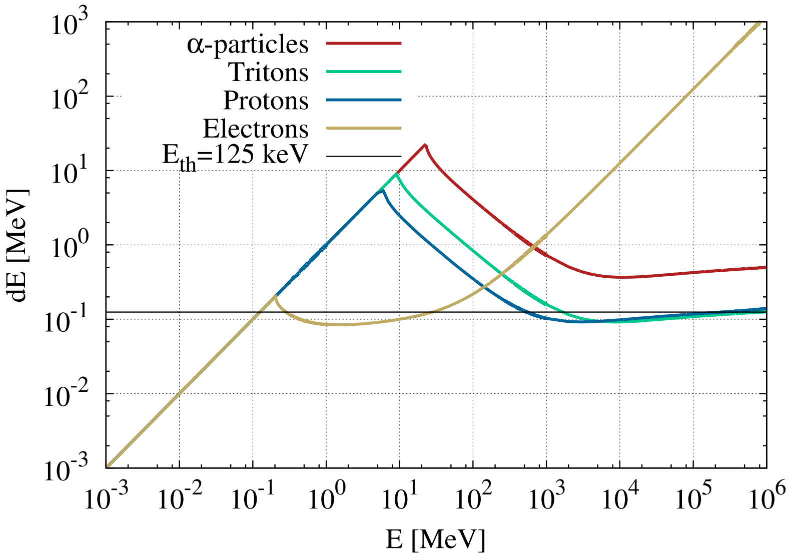

Figure 9.1: Geant4 simulation[1] *of the deposited energy of different particles in 150 μm diamond. α-particles of up to 22 MeV and tritons of up to 9 MeV will deposit their total kinetic energy in the diamond. The threshold energy $E_{th} = 125$ keV corresponds to the lowest possible trigger level for a measurement with the DM-D.*

the sCVD diodes was finally obtained. The results of the different measurements are given in the following subsections.

9.1 Current over Voltage Behaviour

The resistivity of diamond is R $\geq 10^{16}$ Ωm, thus, according to Ohm's Law, the expected leakage current at 150 V (i.e. 1V/μm for the DM-D) is of the order of pA. However, material impurities and defects can reduce the resistivity and therefore lead to an increase of the leakage current. Surface effects, such as graphite layers and imperfections of the metallization influence additionally the current over voltage behaviour. In general, as an unwritten rule, if $I \leq 1$ nA, a diamond sensor can be operated reliably as a detector.

In Figure 9.2 the measured dark-current I as a function of the electric field E is shown for all diamond sensors of the DM-D. The corresponding linear plots (Butterfly-curve) are shown in Table A.3. The nominal operating voltage for the DM-D was 150 V, corresponding to an electric field of 1 V/μm.

The diodes DIAM1 and DIAM8 had a leakage current for negative voltages, that exceeded the expected value of $I \leq 1$ nA by 2-3 orders of magnitude. Therefore they were operated at 0.5 and 0.4 V/μm respectively during the experiments. After a few days of operation, DIAM6 also

---

[1] Courtesy of P. Kavrigin, CIVIDEC Instrumentation

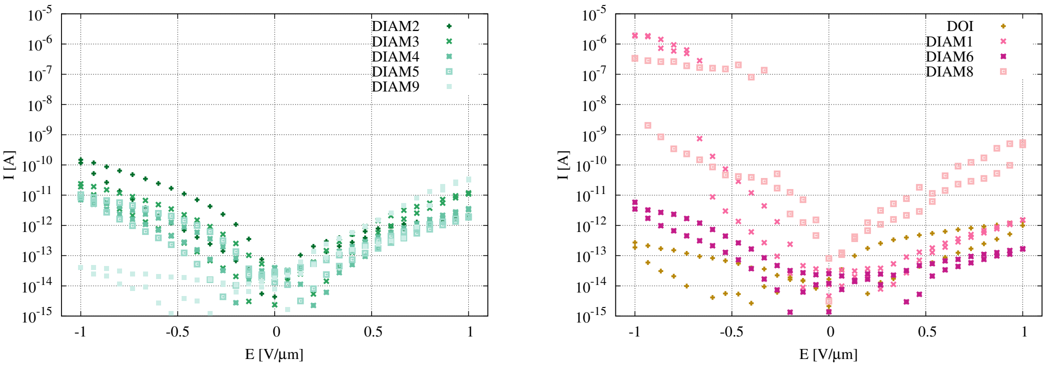

Figure 9.2: Dark current as a function of the electric field, for the different sensors of the DM-D. All diodes in the left panel were biased with +1 V/μm during the measurements. The DIAM diodes represented in the right panel were operated at a reduced bias voltage. The DOID was operated biased with -1 V/μm.

showed an increased leakage current. The voltage was reduced to 0.8 V/μm for this channel.
All other diodes were operated at 1 V/μm during the experiment, see Table 8.1. All DIAM channels were operated with positive voltage, corresponding to the e^- read-out of the diamond diode, in order to have a linear amplification behaviour by the used electronics. The DOID channel was operated with negative voltage in order to read-out the holes and use the spectroscopic properties of the material. For this channel a bipolar CIVIDEC C2 current amplifier was used for the measurements.

9.2 Calibration with α Particles

9.2.1 Saturation Curve

To investigate whether the sCVD diodes were fully saturated at the operating voltage, the charge yield as a function of the applied voltage was measured for all DIAM channels. The measurement was performed with a sealed ^{241}Am α-source in air.
In Figure 9.3 the resulting saturation curves can be seen, which differ in between the diodes in both, the initial gradient and the charge saturation values. The smallest gradient corresponds to DIAM6, which does not even reach saturation at 1 V/μm. This potentially reduces the spectroscopic properties of this diode, which was confirmed by the measurement of the energy resolution. All other diodes reach saturation already at about 0.4 V/μm. Due to the high leakage current, the charge yield of DIAM1 could only be measured up to 0.5 V/μm. The steep slope at low electric field indicates that this diode is sufficiently saturated at 0.4 V/μm.
The variety of charge saturation values indicates that the charge-gain of the diodes is not constant but rather dependent on the specific sensor.

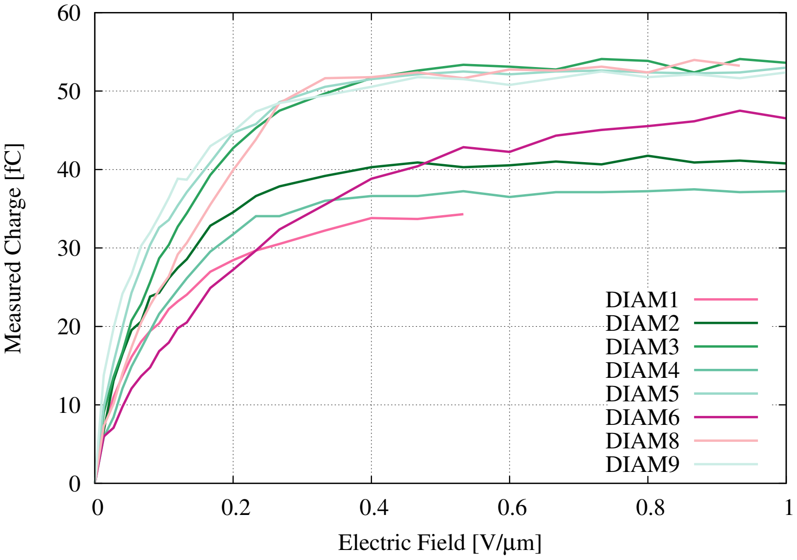

Figure 9.3: Saturation curves for all DIAM sensors of the DM-D. Due to the high leakage current, DIAM1 was only measured up to an electric field of 0.5 V/μm. DIAM6 does not reach saturation below 1 V/μm.

9.2.2 Energy Resolution

The DM-D was calibrated with an α-source containing four different α-emitters, see Table 9.1. The source, a stainless steel disk with the radioactive isotopes equally distributed over a circle of 19 mm diameter, was positioned uncollimated in front of the DM-D with a distance of approximately 2 mm to the diamond diodes. The diodes were fully irradiated with the outgoing α-particles. The calibration was performed under vacuum (p $= 10^{-6}$ mbar) using the CIVIDEC Cx spectroscopic charge amplifiers listed in Table 8.1.

A FLUKA simulation has been performed for the calibration-setup, to verify the expected particle spectra. The resulting spectrum of deposited energy in the diodes was converted in deposited charge using an ionization energy in diamond of $\epsilon = 13.6$ eV. No energy resolution has been applied to the FLUKA results. The simulation confirms that the satellite peaks of ^{239}Pu, ^{241}Am and ^{244}Cm are not expected to be distinguishable, due to the close geometry of sample and diodes and because the α particles were not collimated.
In Figure 9.4 the results of this simulation (first spectrum on the top) is compared to the measured spectra with the DIAM-channels. The electric field at which each of the diodes was operated is

---

[2] Source: CERN-RP#4236RP

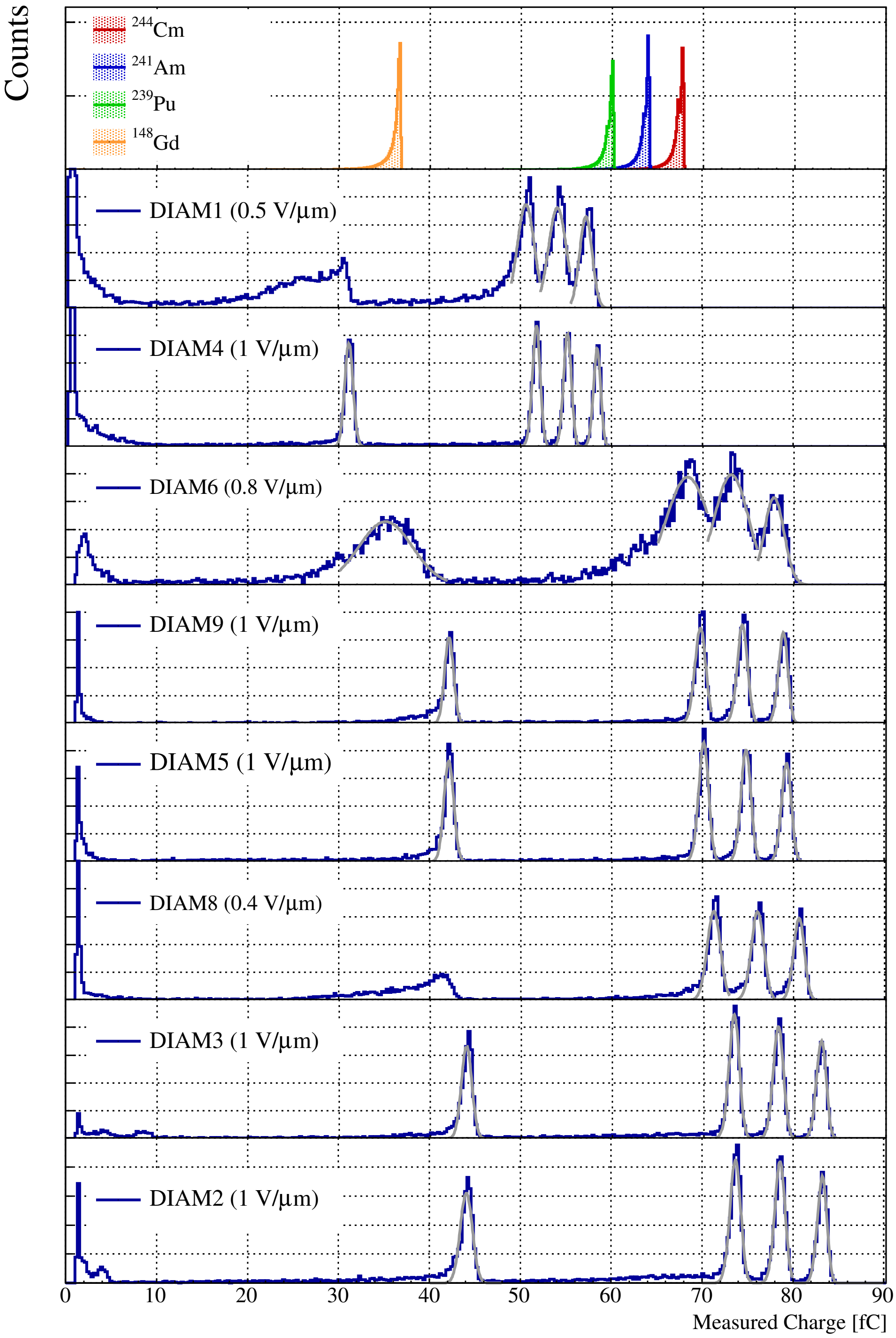

Figure 9.4: Calibration of the DIAM channels with the 4α*-source. On top the results of the FLUKA simulation for the calibration setup, assuming* $\epsilon = 13.6$ *eV, can be seen. The diodes show various charge gains and differ in resolution, see Table A.1. The Gaussian fits to the different peaks are drawn in gray.*

Isotope	Activity [kBq]	Uncertainty [%]	Half life [y]	E_α [MeV]	Intensity [%]
^{148}Gd	1.167	3.24	75±3	3.183	100
^{239}Pu	1.057	3.24	$(2.411\pm0.003)\cdot10^4$	5.105	10.6
				5.143	15.1
				5.156	73.2
^{241}Am	1.186	3.24	432.7±0.5	5.443	12.8
				5.486	85.2
^{244}Cm	1.190	3.23	18.11±0.02	5.763	23.6
				5.805	76.4

Table 9.1: Isotopes contained in the α-source[2] *which was used to calibrate the DM-D.*

given in the corresponding legends. The peaks corresponding to α from the different isotopes were fitted with Gaussian functions respecting the multiple lines for ^{239}Pu, ^{241}Am and ^{244}Cm. The results of each of these fits are listed in the Appendix in Table A.1.

In Table 9.2 the absolute energy-resolution dE in keV for each sensor and all α peaks is listed.

Diode	^{148}Gd dE [keV]	^{139}Pu dE [keV]	^{241}Am dE [keV]	^{244}Cm dE [keV]
DIAM1	n.a.	93	97	67
DIAM2	47	38	37	31
DIAM3	41	36	37	33
DIAM4	46	40	40	36
DIAM5	40	37	38	35
DIAM6	261	178	140	79
DIAM8	n.a.	50	48	39
DIAM9	36	42	39	33
Average ($\overline{dE}$)	78.5	64.3	59.5	44.1

Table 9.2: Resulting energy resolution dE in keV from the Gauss fits to the peaks corresponding to the individual isotopes. In general, the resolution improves with increasing particle energy. For the ^{148}Gd peak of DIAM1 and DIAM8 the approximation of a Gauss distribution is not applicable (n.a.).

DIAM2 has with $dE = 31$ keV at the ^{244}Cm peak the best energy resolution. For DIAM1 and DIAM8 a Gaussian fit to the ^{148}Gd-peak is not applicable (n.a.), hence a value for the energy resolution cannot be given for $E_\alpha = 3.2$ MeV. The energy resolution is affected for the diodes operated with reduced electric field (DIAM1, DIAM6 and DIAM8). The resolution of DIAM6 is with $dE = 79$ keV at the ^{244}Cm peak the lowest of all DIAM diodes.

The charge gain of the diodes differs, independent of the applied electric field, amongst the diodes. Two of the eight diodes, DIAM1 and DIAM4, yield significantly less charge than the others. This was also the case for DIAM2 before it experienced a sudden gain shift during the measurement at n_TOF, see Section 11.3.1. The 4α-calibration was performed after this gain shift.

In Figure 9.5 the spectrum recorded with the DOI diode can be seen in comparison with the

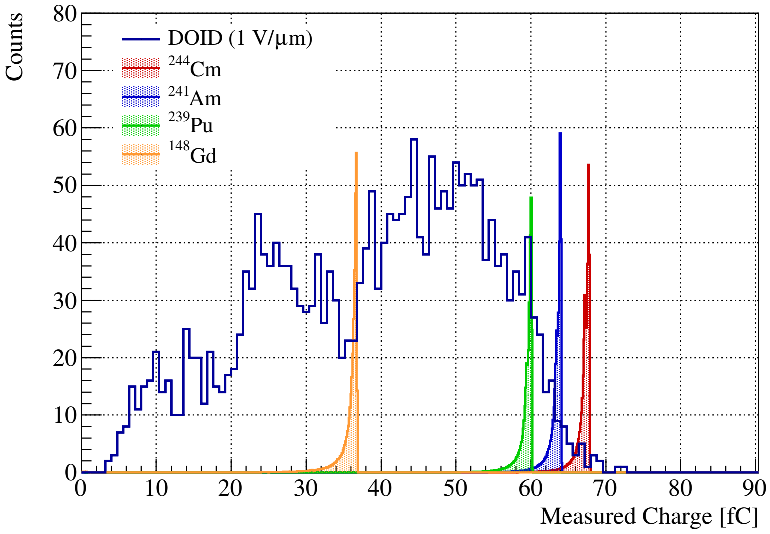

Figure 9.5: Calibration of the DOID channel with the 4α-source, in comparison with the simulated spectrum. There are no distinguishable peaks visible in the DOID spectrum, hence an energy resolution cannot be given for this diode.

simulation. The resolution of this diode is not sufficient to resolve the four individual peaks and can hence not be quantified.

Due to the poor resolution, the data recorded with this diode was not included in the cross-section evaluation for ^{59}Ni(n,α)^{56}Fe. In the experimental spectrum, the α and tritons from the ^{6}Li(n,α)^{3}H reaction could not be distinguished, which prevented a reliable neutron fluence measurement, see Section 12.1 and Table A.4.

9.2.3 Charge Yield of the sCVD Diamonds

The charge yield per 1 MeV deposited energy was determined from the measurements with the unsealed α source and the particle spectra recorded during the ^{59}Ni measurement at n_TOF for all DIAM channels of the DM-D. The charge yield differed between the diodes and a dependency on the penetration depth of the incoming charged particle was observed for the individual diodes. The mean energies, according to FLUKA simulations, the range and the type of the charged particles are listed in Table 9.3.

The measured particle spectra of deposited charge were correlated with the spectra resulting from the FLUKA simulations for the experimental setup, see Figure 9.6. The resulting charge yield in [fC/MeV], corresponding to the value at the minimum χ^2, is shown in Figure 9.7 as a function of the particle's penetration depth for all DIAM channels. The error bars indicate the confidence interval for the correlations [48].

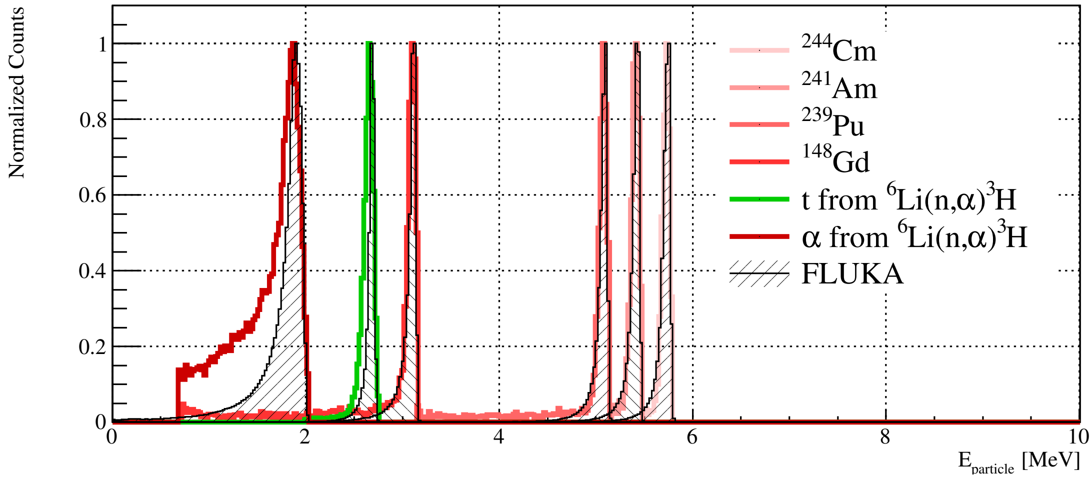

Figure 9.6: Calibration of the particle spectra recorded with DIAM4. The experimental spectra, in color, are correlated by varying the charge yield with the spectra resulting from the FLUKA simulations for the 4α-calibration and the sample measurement.

Table 9.3: Range and energy E of the different charged particles measured with the DM-D.

Reaction or Isotope	Range [μm]	Energy [MeV]	Particle Type
^{6}Li(n,α)t	3.8	1.89	α
^{148}Gd	6.3	3.11	α
^{239}Pu	12.4	5.09	α
^{241}Am	13.6	5.43	α
^{244}Cm	14.8	5.75	α
^{6}Li(n,t)α	21.7	2.68	t

The charge yield for penetration depths above 12 μm is constant within the error margins for all

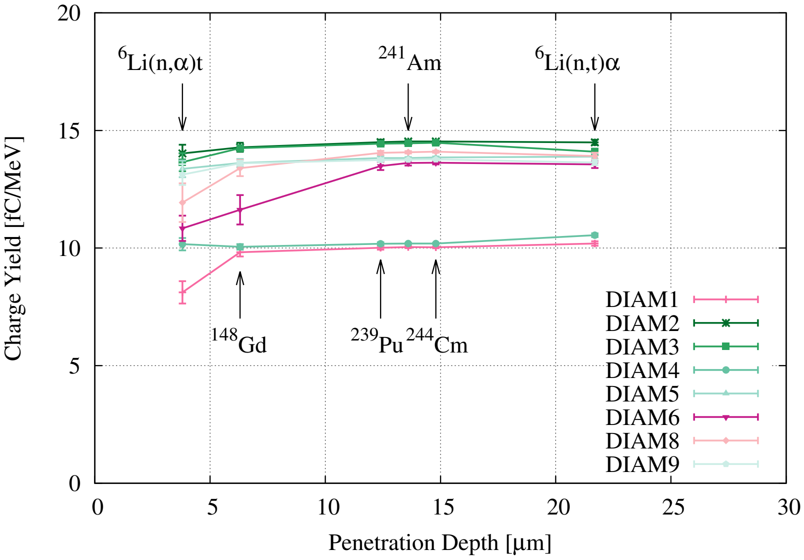

Figure 9.7: Charge yield as a function of the particle's penetration depth for all sCVD diodes of the DM-D. The error bars indicate the confidence interval of the estimated charge yield from the correlation between experimental data and FLUKA simulations.

diodes. A trend towards reduced charge yields is visible for smaller ranges, especially for diodes operated at $E \leq 1$ V/μm, which are displayed in red. This must be related to the recombination of free charge carriers. An inhomogeneous electric field distribution over the thickness of the diodes due to polarization or an increased density of crystal defects close to the surface might be the cause. In diodes which are operated close to the critical electric field, which is the field at which charge saturation is just reached (0.4 V/μm for most DIAM diodes), a local reduction of E would become clearer visible than for diodes operated with high electric field. This is the reason why, for high-precision spectroscopic measurements, an electric field in diamond detectors well above saturation is mandatory.

The average charge yield of DIAM1 and DIAM4 is significantly lower than for the other diodes. This could be related to the metallization of the diodes. After the measurement at n_TOF all diodes were re-metallized in an industrial process with a Ti-Pt-Au (100 nm Ti, 120 nm Pt, 250 nm Au) electrode. The diodes were calibrated with a sealed ^{241}Am source after the re-metallization, where a comparable charge yield in the range of 13.5 fC/MeV - 14.5 fC/MeV was measured for the diodes.

Chapter 10

Conclusions on the Diamond Mosaic-Detector

The Diamond Mosaic-Detector was built for (n,α) cross-section measurements in the n_TOF neutron beam. The detector consists of a mosaic of 8 sCVD diamond diodes and one DOI diode. Various design constraints were to be respected for the detector.

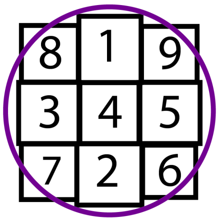

The size of the detector was to be matched to the ^{59}Ni sample used with the DM-D, which had a diameter of 15 mm. A sketch of the DM-D with the ^{59}Ni sample used for the cross-section measurement is shown on the right hand side. The DM-D covers about 95% of the samples surface. For a universal detector for (n,α) measurements at n_TOF, the active area should be increased to a diameter of 35 mm, which would cover the full beam size at n_TOF.
The DM-D allows to easily position a sample in close geometry to the diamond sensors. The capacitance of the DM-D channels remains unchanged when the sample is attached to the PCB structure of the detector. The design of the detector provides a proper RF shielding for 2 GHz read-out.
The DM-D was operated in vacuum at 10^{-6} mbar, which confirms its vacuum compatibility.
The DM-D can be used for spectroscopic measurements of various charged particles in the following energy ranges:

Particle	Energy range
α	125 keV $\leq E_\alpha \leq$ 22 MeV
triton	125 keV $\leq E_t \leq$ 9 MeV
proton	125 keV $\leq E_p \leq$ 6 MeV
electron	125 keV $\leq E_{e^-} \leq$ 200 keV

The upper limit is defined by the thickness of the diamond sensors. The lower limit is restricted by a reliable trigger level of 5σ of the noise of the used electronics. When using the DM-D in a smaller vacuum chamber and hence using shorter cables, this lower limit could further be reduced. The energy resolution was restricted to $dE = 25$ keV, taking the properties of the spectroscopic charge amplifiers and the capacitance of the individual channels into account.

At the calibration with a multiple α source the best energy resolution was achieved for DIAM2 with $dE = 31$ keV at $E_\alpha = 5.8$ MeV. For the DM-D channels which were operated with lower electric field than 1V/μm the energy resolution was reduced. A detailed analysis of the measured energy resolution can be found in Tables 9.2 and A.1. The energy resolution increased for higher particle penetration depths, which indicates that crystal defects accumulate close to the polished diamond surfaces.

The charge gain of the diodes differed between the diamond sensors. This was apparently related to the metallization of the diodes. The diamond substrates were re-metallized after the measurement at n_TOF and finally showed comparable charge gains in the range of 13.5 fC/MeV - 14.5 fC/MeV.

The nominal bias voltage for the operation of the DM-D was 1 V/μm. DIAM1 and DIAM8 were operated at 0.5 V/μm and 0.4 V/μm respectively, due to an increased dark current, observed in the IV-curves at negative voltages. DIAM6 was operated at 0.8 V/μm, as the dark current increased during operation. All other channels were operated at 1 V/μm, where negative voltage was used for the DIAM channels (corresponding to e^- read-out), which were amplified with unipolar CIVIDEC Cx spectroscopic charge amplifiers. The DOID channel was operated at positive voltage, in order to read out the holes and use the spectroscopic properties of this material. The DOID was operated with a bipolar CIVIDEC C2 2 GHz current amplifier.

The amplifiers used with the DM-D were electronically calibrated prior to the measurements. The gain of the spectroscopic charge amplifiers, about 8 mV/fC, were matched to the capacitance of the individual DIAM channels based on this calibration. The amplifiers, which provide a standard Gaussian pulse shape, have a linear amplification up to a deposited energy of 20 MeV in the diamond detectors, being matched to the application at n_TOF. The current amplifier used with the DOID channel had a gain of 40.9 dB and a linear behaviour for output voltages $-1\text{V} \leq U \leq +1\text{V}$.

For the material budget in the neutron beam a compromise had to be found respecting the acceptable capacitance of the DM-D channels, a reliable RF shielding up to 2 GHz and the minimization of the PCB material. The material budget would be best minimized using one large area spectroscopic diamond, which is not available to date. Such a diamond diode could be positioned in the neutron beam, with the support material only at the edges of the neutron beam. Such a detector design was successfully tested with a pCVD diamond sensor at n_TOF in 2011 [65], but the pCVD diamond material, due to the lack of spectroscopic properties, has proven not to be suited for (n,α) measurements.

The DOI diode was included in the DM-D to test this material for its applicability for (n,α) cross-section measurements. This material is the only available potential candidate for large area spectroscopic diamond detectors to date. The used DOI diode did not have sufficient spectroscopic properties to resolve the four peaks of the α source. An energy resolution can hence not be defined for this diode. The data recorded with this diode during the measurement at n_TOF was consequently not included in the evaluation of the ^{59}Ni cross-section. The advances with this diamond material should still be followed for eventual future applications in the field of (n,cp) cross-section measurements.

Part III

Proof of Principle

The DM-D was used to measure the ^{59}Ni(n,α)^{56}Fe cross-section at n_TOF. The aim of the measurement was to determine the integral of the dominant resonance in this reaction at $E_n = 203$ eV and to compare it to the previous measurements by Harvey [2] and Koehler [3]. The sample for the measurement consisted of a thin layer of ^{59}Ni coated with a thin layer of ^{6}LiF. The signals coming from the ^{6}Li(n,α)^{3}H reaction were used to determine the beam interception factor (BIF).

Besides the measurement with the sample, also a measurement with the sample backup-foil was performed to determine the background from the sample backing in the ^{59}Ni measurement. An additional measurement with only the DM-D positioned in the neutron beam was performed to determine the background coming from the detector.

The experimental setup is described at the beginning of Chapter 11. The sample specifications are given followed by the description of the different measurements which were performed during the ^{59}Ni campaign. Finally the gain stability of the DM-D is discussed in this Chapter.

In Chapter 12 the data analysis process from raw data to the final cross-section is described. The raw data analysis routine is described and limitations for the reliability of the data at high neutron energies are given. The background of the DM-D in the neutron beam is analyzed, followed by the TOF to E_n calibration, for which the resonant background coming from different materials on the DM-D was used. The analysis conditions and efficiency corrections are given before the final cross-section as the result of the measurement.

Conclusions on the outcome of the cross-section measurement in comparison to previous measurements of the ^{59}Ni(n,α) cross-section are given in Chapter 13.

Chapter 11

^{59}Ni(n,α)^{56}Fe Measurement at n_TOF in 2012

The ^{59}Ni(n,α)^{56}Fe campaign at n_TOF took place in the period 15. October - 9. November 2012. Details on the experimental setup, the sample and the measurements which were performed during the campaign are given in the following sections.

11.1 Experimental Setup at n_TOF

At the spallation target the choice of neutron moderator in 2012 was borated water, and therefore the in-beam photon background was dominated by γ from the reaction ^{10}B(n,α)^{7}Li*, where the residual nucleus de-excites by emitting a photon with $E_{\gamma} = 478$ keV. In addition, the neutron fluence at low neutron energies was reduced in comparison to the configuration with deionized water as neutron moderator.

The DM-D was positioned in the experimental area of n_TOF, at about 183 m from the spallation target, inside a vacuum chamber, 78 cm downstream the exit window of the n_TOF neutron flux monitor (SiMon). All measurements were performed under vacuum with a maximum pressure of $p_{max} = 10^{-5}$ mbar. The setup for the measurement in the experimental area at n_TOF is shown in Figure 11.1.

Each channel of the DM-D was connected to a hermetic 50 Ω SMA feed-through in the lid of the vacuum chamber by a 50 Ω SMA cable of approximately 20 cm length. The capacitance of each channel, the bias voltage during operation, the corresponding amplifier and the related gain are given in Table 8.1. The gain of the spectroscopic charge amplifiers was about 8 mV/fC. With a capacitive load of approximately 35 pF from the DIAM channels, a SNR of 40/MeV was reached. The nominal voltage of 1V/μm was applied only to six of the nine diodes, due to the high leakage current of the remaining three diamond sensors. The reduced electric filed applied to the latter resulted in a reduction of the energy resolution, which was however sufficient to distinguish the relevant particle spectra for the cross-section measurement. In contrary, the data recorded with

the DOI diode was not included in the cross-section evaluation, as the particle spectra could not be well distinguished with this diode.
The amplifier output was connected to the 8 bit flash-ADC cards of the n_TOF data acquisition system (DAQ) [38] by 20 m long, 50 Ω BNC cables. The data was sampled with 250 MS/s for all DM-D channels with a sCVD diode, where the amplifiers provided a Gaussian pulse shape with FWHM = 180 ns. The DOI channel, which was read-out with a 2 GHz current amplifier, was sampled with 2 GS/s. With 8 MB memory from the DAQ, a time window of 32 ms and 4 ms was recorded for the sCVD diodes and the DOI channel respectively, at each trigger coming from the PS. This corresponds to a minimum neutron energy of $E_n = 0.17$ eV for all DIAM channels, and $E_n = 11$ eV for the DOID, respectively.
The full range of the flash-ADC for each channel was set between 0.2 V and 1 V, adjusted to the individual gain of each channel and with focus on a maximum possible energy resolution for 5 MeV α emitted in the ^{59}Ni(n,α)^{56}Fe reaction.

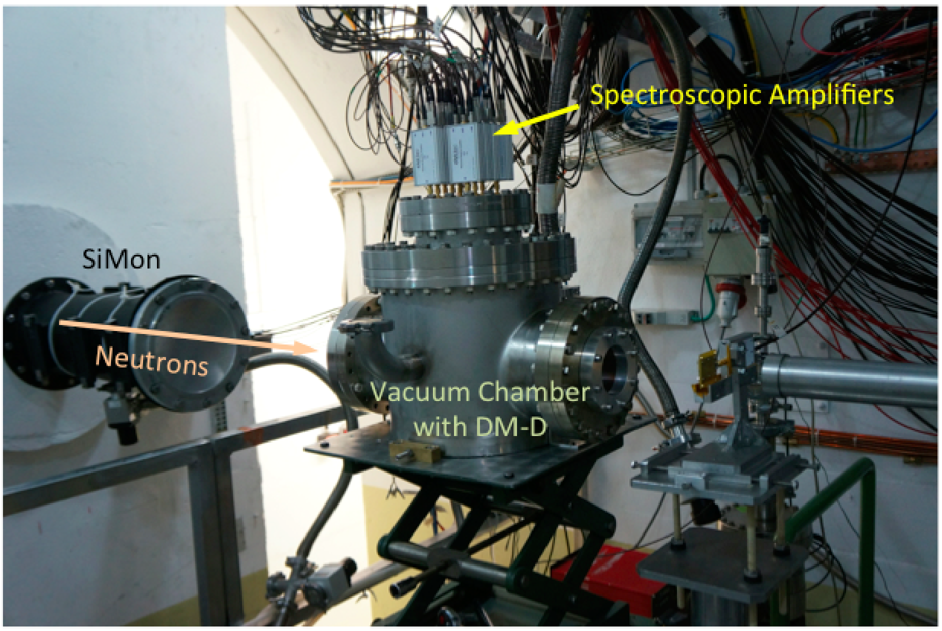

Figure 11.1: Experimental setup at n_TOF during the ^{59}Ni(n,α) measurement campaign

11.2 The Sample

For the measurement of (n,cp) reactions the sample has to be thin enough to allow the reaction products to exit the sample without significant energy loss in the material. For the ^{59}Ni(n,α)^{56}Fe cross-section measurement at n_TOF a 100 nm thick metallic ^{59}Ni deposit, which was electroplated on a 25 μm Pt foil and coated with 400 nm of ^{6}LiF, was used. The ^{59}Ni and

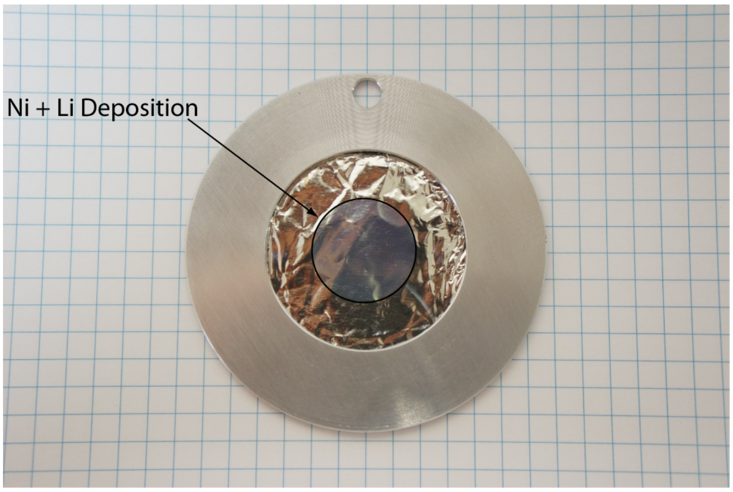

Figure 11.2: Photograph of the sample used for the ^{59}*Ni(n,*α*)*^{56}*Fe cross-section measurement at n_TOF in 2012. The circular material deposition with 15 mm diameter can be seen in the center of the foil.*

Table 11.1: Specifications of the sample; the reaction to be measured is listed as well as the maximum energies of the reaction products which can reach the detector (α *...* ^{4}*He nucleus, t ... triton =* ^{3}*H nucleus, p ... proton =* ^{1}*H nucleus).*

Sample	Mass [μg/cm^2]	Enrichment [%]	Thickness [μm]	Form	Reaction	Particle Energy [MeV]
Pt backing			25	metallic	background	
^{59}Ni	91 ± 2.5	95.0 ± 0.2	0.102	metallic	^{59}Ni(n,α)^{56}Fe ^{59}Ni(n,p)^{59}Co	$E_\alpha = 4.76$ $E_p = 1.82$
^{6}Li	104 ± 2.5	95.6 ± 0.2	0.394	LiF	^{6}Li(n,α)^{3}H	$E_\alpha = 2.06$ $E_t = 2.73$

^{6}LiF deposition is 15 mm in diameter. The Pt foil, 55 mm in diameter, was fixed on an Al ring of 1 mm thickness and an inner diameter of 30 mm, see Figure 11.2. The same sample was used for the measurements at ORELA in 1975 [2] and 1999 [3] and was provided by Karlsruhe Institute of Technology for this measurement at n_TOF. The sample specifications are listed in Table 11.1.

The neutron fluence, which is measured with a reaction where the cross-section is considered standard, has to be known for the evaluation of the reaction cross-section. Ideally the sample offers the possibility to measure both the cross-section and the neutron fluence at the same time, as this eliminates uncertainties related to the alignment of sample and detector in the neutron beam. At a neutron facility where the neutron fluence is well known, as is the case for the

n_TOF facility [34], equivalently the beam interception factor (BIF) can be determined, which is then used to scale the neutron fluence spectrum. The ^{6}Li(n,α)^{3}H cross-section is considered a standard cross-section up to 1 MeV, hence the ^{6}LiF layer on the sample was used to determine the BIF for the ^{59}Ni measurement.
With the ^{59}Ni layer the ^{59}Ni(n,α)^{56}Fe cross-section was measured. The maximum kinetic energy for the recoil nucleus ^{56}Fe, at thermal neutron energies, is 0.34 MeV, which is too low to exit the sample and hence only the α particles of this reaction, with $E_\alpha = 4.76$ MeV, can be detected.
A FLUKA [102, 103] simulation has been performed for the experimental setup at n_TOF to see the expected particle spectra for the measurement. Both the detector and the sample were included in the simulation, which looked at the energy of the particles entering the DM-D. The primary particles, as listed in Table 11.1, were emitted in the simulation isotropically in the volume of the corresponding layer of the sample. The resulting particle energy spectra entering the diamond were weighed by the thermal cross-section of the corresponding nuclear reaction. The measured cross-sections by J. Harvey [19] were used for the ^{59}Ni cross-sections, with $\sigma(n,\alpha) = 11.4$ barn and $\sigma(n,p) = 1.43$ barn. The thermal cross-section of ^{6}Li(n,α)^{3}H was, with $\sigma(n,\alpha) = 941$ barn, taken from the nuclear data library JEFF-3.1.

The resulting particle-energy spectra at thermal neutron energies can be seen in Figure 11.3, where the energy resolution of the detector has not been considered. The simulation confirms that all but the ^{59}Ni(n,p) reaction can be distinguished from each other when this sample is used for the experiment. The proton energy of $E_p = 1.82$ MeV is smaller than the energy of the reaction products of ^{6}Li(n,α)^{3}H, $E_\alpha = 2.06$ MeV and $E_t = 2.73$ MeV. The cross-section of the corresponding reaction is of the same order of magnitude at the peak of the dominant resonance at $E_n = 203$ eV and three orders of magnitude smaller elsewhere. The experimental proton spectrum is superimposed by the α-spectrum from the ^{6}Li(n,α)^{3}H reaction.

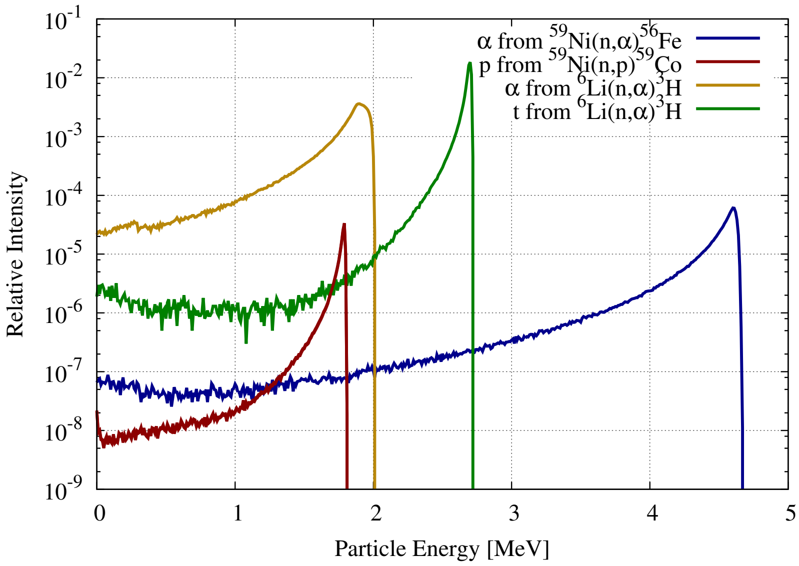

Figure 11.3: FLUKA simulation results for the expected particle spectra. The spectra are weighed with the cross-section of the corresponding reaction at thermal neutron energies.

The used sample hence fulfills all requirements for a reliable ^{59}Ni(n,α) cross-section measurement. For a measurement of the ^{59}Ni(n,p) reaction a sample without the additional LiF layer has to be used and the neutron fluence has to be determined separately.

11.3 Measurements during the ^{59}Ni Campaign at n_TOF

During the ^{59}Ni campaign at n_TOF the following measurements were performed with the DM-D:

- **Ni-59**: The cross-section and the neutron fluence were measured during two weeks with the ^{59}Ni + ^{6}Li sample as a function of the neutron energy. In the amplitude spectra the signals corresponding to α from ^{59}Ni(n,α)^{56}Fe and tritons from ^{6}Li(n,α)^{3}H were selected for the determination of the cross-section and the BIF, respectively.

- **Dummy**: A measurement was performed with the sample back-to-front, to see the background caused by the Pt backing of the sample. The Pt foil was with 25 μm thick enough to absorb the reaction products coming from the ^{59}Ni and ^{6}Li deposition on the opposite side of the foil in this setup. The resulting count rates as a function of the neutron energy were subtracted from the Ni-59 measurement as background for each of the diodes individually.

- **Sample-out**: The background contribution from the DM-D was measured with only the detector positioned in the neutron beam, to understand the limits of the detector for (n,cp) measurements and evaluate possible future upgrades of the detector.

- **Beam-off**: During 3 hours without beam a measurement was performed with the sample mounted in front of the detector, for the environmental background and the radioactive decay of ^{59}Ni with an external (beam-independent) trigger to the DAQ. As expected, there were no signals recorded during this measurement.
  The radioactive decay of ^{59}Ni is with 7 keV X-rays far below the energy threshold of the DM-D. The environmental background at n_TOF is dominated by the natural decay of ^{40}K, of which only the γ of the decay into ^{40}Ar via e^{-}-capture would reach the DM-D positioned in the vacuum chamber. The Beam-off measurement confirmed that, due to the low γ-detection efficiency of diamond and the low ambient background level at n_TOF, only beam related background has to be taken into account for the measurement with the DM-D.

The proton budget and the dates for each of the measurements are given in Table 11.2. The outcome of the different measurements and the data analysis are described in the next chapter.

Table 11.2: Dates, proton budget and the corresponding neutron budget for the measurements performed during the ^{59}*Ni(n,*α*)*^{56}*Fe campaign at n_ TOF in 2012. The number of dedicated TOF pulses, with an intensity of* $7 \cdot 10^{12}$ *protons per pulse (ppp), and the number of parasitic pulses, with* $2 \cdot 10^{12}$ *ppp, are listed as well.*

Measurement	Dates in 2012	TOF Pulses	Parasitic Pulses	Protons $\cdot 10^{17}$ Total	Neutrons $\cdot 10^{11}$ Total
Beam-off	06.11.	0	0	0	0
Ni-59	19.10.-01.11.	110'571	68'500	9.11	1.30
Dummy	17.10.-19.10. & 01.11.-05.11.	48'143	35'500	4.08	0.58
Sample-out	15.10.-17.10 & 07.11.-09.11.	20'715	17'000	1.79	0.26
Total	15.10.-09.11.	179'429	121'000	14.98	2.14

11.3.1 Calibration of the DM-D during the ^{59}Ni Campaign

- On 15., 17. and 19. October 2012 the DM-D was calibrated with a sealed ^{241}Am source. These calibrations were performed in air, as the effect of 2 mm air, which was the distance between the source and the detector, on the broadening of the energy distribution of the α particles could be neglected in comparison to the 1.8 μm Pd-sealing of the source. The calibrations showed that during this period the gain of the diodes was stable.

- On 05. November, the DM-D was calibrated under vacuum with an unsealed α-source containing four radioactive isotopes. A detailed analysis on the outcome of this calibration where the energy resolution of the individual channels was determined is given in Section 9.2.

- During the Ni-59 measurement the diodes were calibrated on-line via the triton peak of the ^{6}Li(n,α)^{3}H reaction. In Table 11.3 the position of the triton-peak for the first and the last ^{59}Ni run and the resulting gain shift for all the diodes are listed in fC. Three diodes experienced a positive gain shift, five diodes a negative gain shift and one of the diodes showed the same gain at the first and the last ^{59}Ni run. For reasons that remain unclear, on 22. October an instantaneous positive gain shift by 21% occurred in DIAM2. The impact of the shift is illustrated in Figure 11.4, which shows the amplitude spectra recorded at the beginning and the end of the measurement.
  The thresholds in the data analysis were adjusted accordingly for DIAM2 after the gain shift. For all other diodes, the gain shift was small enough to be neglected.

Table 11.3: Gain stability of the diodes during the ^{59}Ni runs.

Channel	First ^{59}Ni run Triton-peak [fC]	Last ^{59}Ni run Triton-peak [fC]	Gain Shift [fC]	Gain Shift [%]
DIAM1	28.4	28.0	-0.4	-1.4
DIAM2	32.5	39.3	+6.8	+20.9
DIAM3	39.5	39.5	0	0
DIAM4	29.3	29.1	-0.2	-0.7
DIAM5	38.8	38.0	-0.8	-2.1
DIAM6	38.1	37.6	-0.5	-1.3
DIAM8	38.7	38.2	-0.5	-1.3
DIAM9	37.7	38.5	+0.8	+2.1
DOID	28.4	29.2	+0.8	+2.8

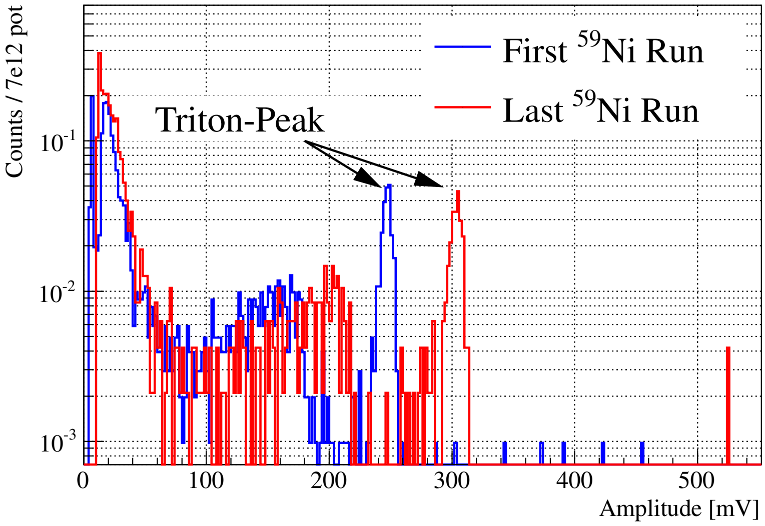

Figure 11.4: Amplitude spectrum of DIAM2 for the first and the last recorded ^{59}Ni run. The gain shift in this diode became apparent via the position of the triton (t) peak of the ^{6}Li(n,α)^{3}H reaction. The gain stability during the ^{59}Ni measurement was monitored for all diodes via the position of the t-peak.

Chapter 12

From Data to Cross-Section

The experimental data (digitized detector signals) for each channel was analyzed offline to obtain the information about the pulse-height with respect to the TOF. A TOF to E_n calibration was performed using the resonances caused by neutron-induced reactions in the in-beam materials. With the obtained E_n-spectra further analysis with selection cuts, background subtraction and efficiency corrections was performed to finally obtain the yield and the cross-section.
The performed data analysis from raw data to the cross-section is described in the following sections.

12.1 Raw Data and Pulse Shape Analysis

For the DIAM channels and the DOID channel a total of 32 ms and 4 ms have been recorded respectively per proton pulse with the n_TOF DAQ. To reduce the amount of stored data, a zero suppression was implemented in the DAQ by using a constant threshold for each of the channels. Hence, only time windows containing a signal, with 1024 samples before and 2048 samples after the threshold crossing, were recorded with the corresponding time stamp from the DAQ system, which was triggered by the CERN-PS accelerator.
In Figure 12.1 an example of raw experimental data without zero suppression is shown. The zoom into the first 90 μs ($E_n > 22$ keV) in Figure 12.1(b) shows the undershoot of the AC coupled charge amplifiers as reaction to the intense γ-flash signal. The constant baseline before the γ-flash is indicated (BL) to guide the eye.
The undershoot may lead, if not properly taken into account, to missing signals or to a wrong determination of the pulse amplitude. For this reason a baseline reconstruction routine was implemented for the undershoot region in the following way:

1. Pulses are found and discarded using the derivative of the recorded data.
2. The resulting gaps are filled with the last baseline value after the discarded signal.
3. A 250 kHz FIR-Filter is applied to smoothen the resulting baseline.

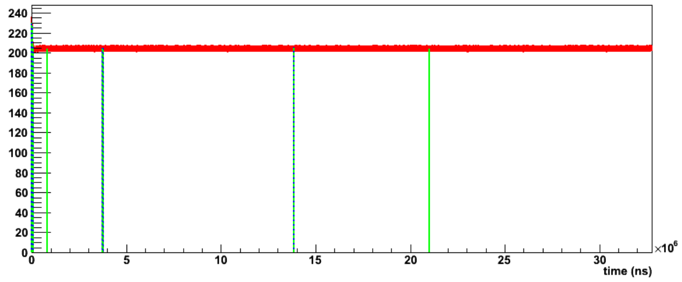

(a) Full time window of about 32 ms, which corresponds to neutron energies 0.17 eV $\leq E_n \leq$ 20 GeV.

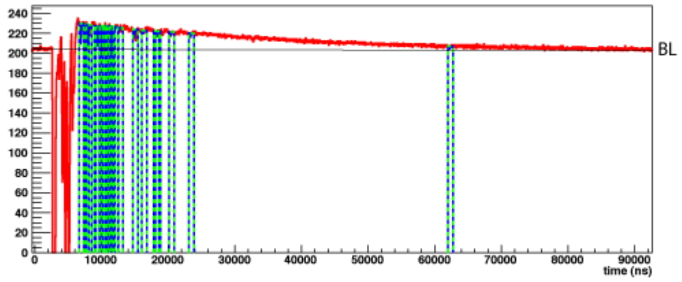

(b) Zoom into the region $E_n \geq$ 20 keV. A baseline reconstruction routine has been implemented to compensate for the undershoot of the AC coupled charge amplifier after the γ-flash.

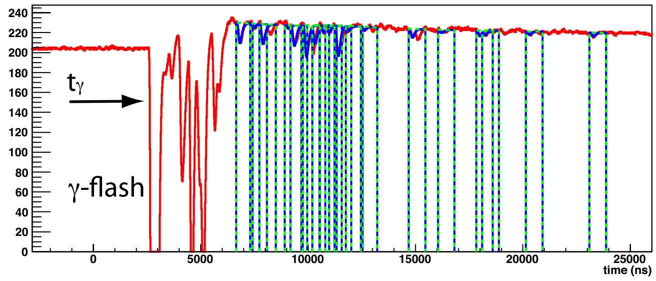

(c) Zoom into the γ-flash region. The routine starts to search for signals 3 μs after the γ-flash. The time intervals where signals were found are marked with green lines.

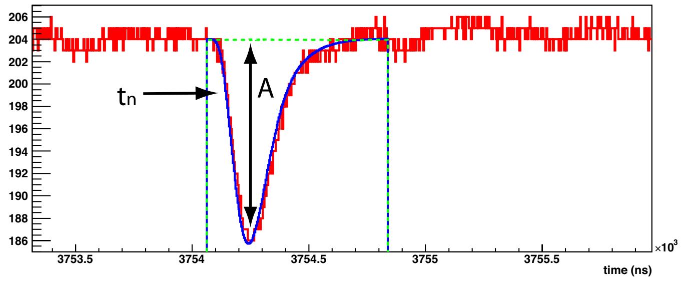

(d) Zoom into a single signal. The reconstructed signal (blue) is used to evaluate the pulse height A and time of arrival t_n.

Figure 12.1: Exemplary experimental data in the raw data analysis program [1].

This procedure reconstructed the baseline most reliably. Other methods, like a parabolic fit to the baseline, were not as reliable due to the high counting rate at short TOF and the fact that the amplitude of the undershoot of the amplifier is dependent on the intensity of the γ-flash signal. Outside the undershoot region, where the counting rate was small, the baseline was obtained by applying a linear fit to the recorded data outside the signals.

The zoom into the γ-flash region, see Figure 12.1(c), shows how the t_γ for the calculation of the TOF according to Equation 2.1 could be determined. For the data analysis of the measurement with the DM-D, the signal of the n_TOF proton pulse intensity detector (PKUP), which has a constant offset of t_{delay} = 700 ns to the γ-flash signal, was used to determine t_γ:

$$t_\gamma \;=\; t_{PKUP} \;+\; t_{delay}. \tag{12.1}$$

The signals are found by the pulse shape analysis routine using a constant threshold. An average and normalized reference signal is then fitted to the data for finding the time t_n and amplitude A of an identified signal, as shown in Figure 12.1(d).

The measurement was optimized to determine the cross-section of ^{59}Ni(n,α) at neutron energies below 300 eV (TOF $\geq$ 0.77 ms) with the maximum possible resolution for the recorded particle spectra. The analysis did not focus on measuring at higher neutron energies, where the signal amplitudes increase with the neutron energy and the baseline undershoot occurs. Therefore:

- Signals with $t_n \leq 6\ \mu$s have not been analyzed, see Figure 12.1(c).
- The DAQ full range of each channel was set according to the gain and optimized for a maximum resolution at TOF = 930μs (E_n = 203 eV). This resulted in a cut-off of the undershoot region for high-intensity pulses (TOF pulses at n_TOF, see Table 11.2). Hence the E_n-range for a reliable spectroscopic measurement was restricted to E_n < 500 keV (TOF $\geq$ 19μs).

With the calibrated flight path via resonant reactions in the background spectrum, the TOF was converted in E_n. For the cross-section evaluation the amplitude spectra were directly used for particle identification. Due to the small counting rate in the region of interest (TOF $\geq$ 19μs), there was no pile-up correction necessary for the resulting particle spectra. For E_n < 500 keV the amplitude spectra have an uncertainty below the expected amplitude resolution (Figure 6.6) due to the effective analysis routine.

At neutron energies above 500 keV the uncertainty increases due to the setup of the DAQ. For TOF < 4μs (E_n > 1 MeV) the probability that signals were not recognized by the analysis routine due to the pile-up of signals is increasing. For cross-section measurements at short TOF with the DM-D, a fast current amplifier should rather be used to prevent uncertainties related to pile-up. For the conversion of the amplitude spectra into deposited charge for the evaluation of the charge yield of the diodes, see Section 9.2.3, the amplitudes were divided by the individual gains of the amplifiers, which were calibrated electronically.

In Figure 12.2(a) the amplitude versus TOF-spectrum for all recorded runs with the ^{59}Ni + ^{6}Li sample for one of the sCVD diodes is shown. In Figure 12.2(b) the TOF is converted into E_n following equation 2.2. The number of recorded signals is encoded in colour. The contribution of the α-particles from ^{59}Ni(n,α)^{56}Fe and the tritons and α-particles from ^{6}Li(n,α)^{3}H can clearly

---

[1] Courtesy C. Guerrero, CERN, E. Mendoza and D. Cano-Ott, CIEMAT, Spain

be seen beside the background contribution from the DM-D. When projecting the spectra on the y-axis, the amplitude or particle spectra are obtained respectively. The projection on the x-axis results in the TOF- and E_n-spectra respectively. The E_n-spectra were normalized to the average proton pulse intensity for dedicated TOF pulses, $7 \cdot 10^{12}$ protons-on-target (pot), for the data analysis.

The long flight path at n_TOF provides a very good neutron energy resolution of $dE/E < 5 \cdot 10^{-4}$ in the neutron energy region of interest for the ^{59}Ni measurement. This allows to resolve narrow resonances in the spectrum. The resonances of Ag and Pt in the background spectrum of the DM-D, which are visible in Figure 12.2 at amplitudes below 100 mV, $10^6 \leq \text{TOF} \leq 10^7$ ns and $1 < E_n < 70$ eV respectively, were used for the TOF to E_n calibration.

The spectroscopic properties of the sCVD diodes in the DM-D allow to reliably distinguish the different reaction products of interest, as is indicated in Figure 12.2. In addition the reactions of interests can be distinguished from the background in the amplitude spectra, which correspond to the deposited charge by the particles in the sensors.

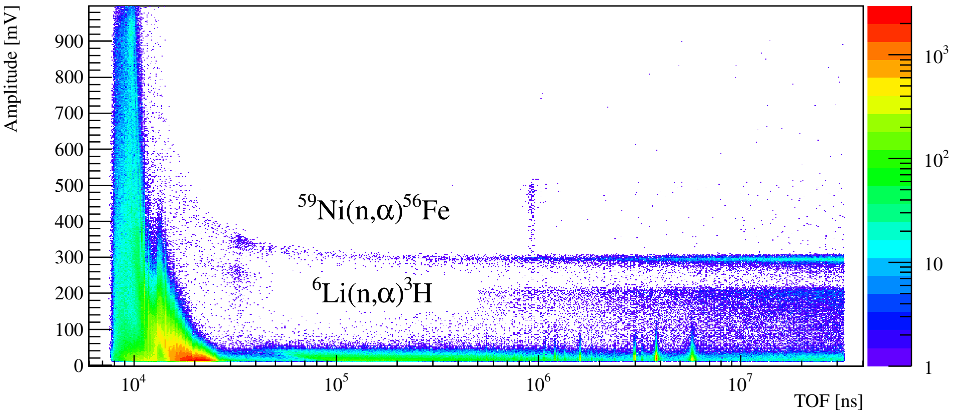

(a) Amplitude versus TOF spectrum for the measurement with the sample.

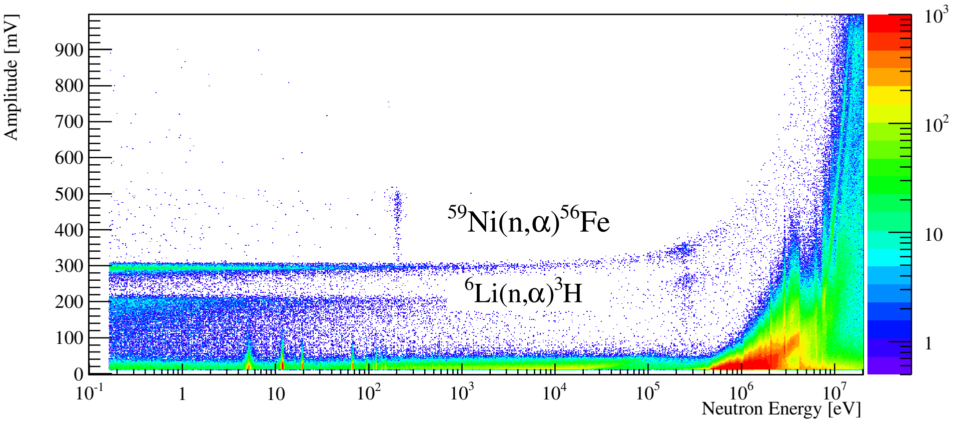

(b) Amplitude versus E_n spectrum for the measurement with the sample.

Figure 12.2: Experimental data from DIAM9.

12.2 Background of the DM-D in the n_TOF Beam

The background contribution of a given material in a neutron beam is related to the material thickness, the cross-section of the nuclear interactions who's reaction products can reach the detector and the detection efficiency for the corresponding reaction products. The approximate material budget of the DM-D intercepting the neutron beam is:

- 1000 μm PCB material.
- 150 μm C: diamond substrates.
- 75 μm Ag: main component of the glue.
- 35 μm Cu: metallization of the back PCB.
- 5 μm Ni: metallization of the main PCB.
- 0.4 μm Al: Metallization of the diodes.
- 0.02 μm Au: metallization of the main PCB.
- Ni+Au from the feed-throughs on the main PCB.

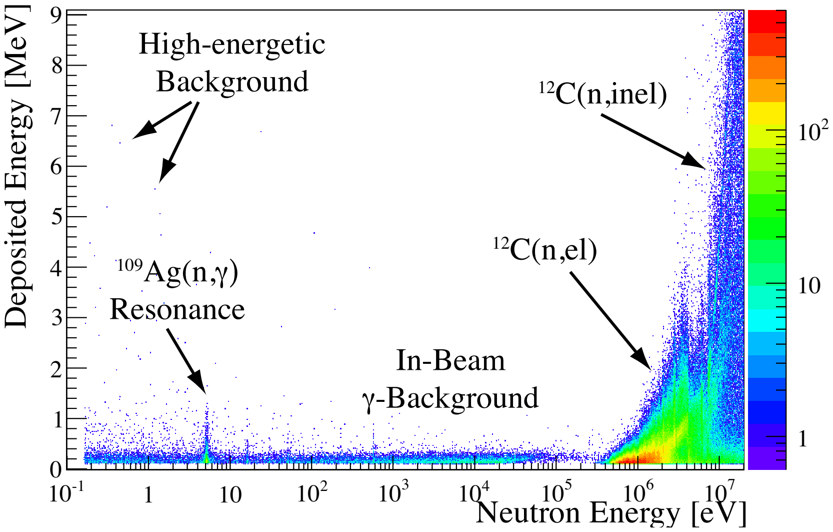

Figure 12.3: Deposited energy over neutron energy for the DM-D in the n_TOF neutron beam, from the Sample-out measurement. The number of recorded signals is encoded in colour.

During the ^{59}Ni campaign at n_TOF, a measurement with only the DM-D positioned in the beam (Sample-out measurement) has been performed. The deposited energy spectrum as a function of the neutron energy of one of the DIAM diodes is shown in Figure 12.3, with the recorded number of counts encoded in color.
The in-beam γ at n_TOF contribute to the spectrum as well as γ from capture reactions in the surrounding materials. Especially the dominant resonance of ^{109}Ag(n,γ)^{110}Ag is visible in the spectrum at $E_n = 5.2$ eV.

Above E_n = 300 keV, the elastic reaction in ^{12}C becomes visible, while the contribution of inelastic nuclear reactions in ^{12}C contribute only at neutron energies above 6 MeV.
In the low E$_n$ region, background signals with a high energy deposition in the detector were recorded. These signals were not observed during the measurement where the neutron beam was turned off, hence they must be related to beam-induced background reactions in the surrounding materials. Due to the poor statistics, the origin of these signals could not be clarified.
In Figure 12.4 the projection of the scatter plot in Figure 12.3 on the neutron energy axis is illustrated. The displayed evaluated nuclear cross-section data for each material was scaled to this background spectrum, to show the contribution of the different materials to the background spectrum.
Neutron capture resonances in the stable isotopes of Ag, the main component of the glue of the diodes, and Cu from the metallization of the PCB's, can clearly be identified. Also the structures in the elastic cross-section of ^{12}C can be identified at high E_n. The in-beam γ at n_TOF contribute to the smooth shape of the background spectrum in the keV region. In the low E_n region, the background has the typical $1/\sqrt{E}$ shape for neutron-induced nuclear reactions without threshold but the contribution of the different materials and reactions cannot be distinguished.

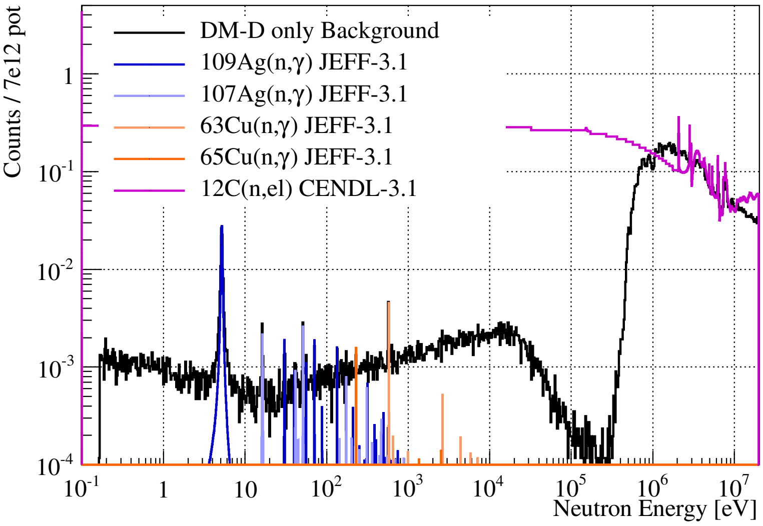

Figure 12.4: Background spectrum of the DM-D in the n_TOF neutron beam. The evaluated neutron cross-section data of the different isotopes is scaled to the spectrum, to show the individual contributions which could be identified. The in-beam γ at n_TOF are the main contribution to the background in the keV region.

12.3 TOF to E_n Calibration

The geometrical flight path L between the spallation target and the detector can be calibrated by analyzing known resonances in the spectrum, coming from neutron-induced nuclear reactions in the in-beam materials. The recorded TOF is thereby compared to the expected neutron energy of the resonances and then L is found by fitting the expected analytical function $E_n = (72.29 \cdot L/t)^2$ from Equation 2.3 to the TOF-E_n data points.
The DM-D contains a significant amount of natural Ag, which is the main substance in the glue for the diodes. The ^{109}Ag(n,γ) reaction causes the big resonance in the spectrum at 5.19 eV, see Figure 12.3. The resonance visible at 16.3 eV is caused by ^{107}Ag(n,γ) reactions. Resonances from capture reactions in ^{63}Cu and ^{65}Cu can as well be identified in the background spectrum of the DM-D. The spectra of measurements with the Pt foil in front of the DM-D show in addition very pronounced resonances of capture reactions in ^{nat}Pt.
In Figure 12.5 the resonance energy of the most pronounced resonances visible in the Dummy-measurement spectrum as a function of the measured TOF can be seen together with the fitting function following Equation 2.3. The obtained geometrical flight path for the DM-D following this calibration is

$$L = 183.11 \pm 0.03 \text{ m}. \tag{12.2}$$

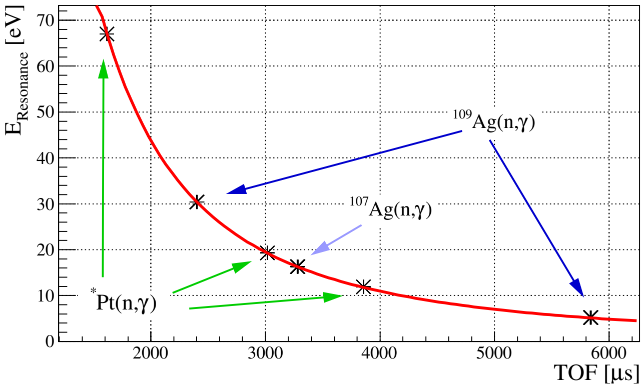

Figure 12.5: TOF to E_n calibration by fitting the non-relativistic expression for the neutron energy as a function of TOF for visible resonances in the background spectrum.

In Figure 12.6 an exemplary E_n-spectrum from the Dummy measurements is shown in comparison with evaluated nuclear data for the capture reactions in Pt and Ag as well as the elastic scattering cross-section in ^{12}C. The recorded TOF-spectra were converted in E_n-spectra with the geometrical flight path given by the above calibration. A zoom into the energy region of the resonances used for the TOF to E_n calibration is illustrated in Figure 12.6(a). Above a few hundred keV neutron energy, the elastic scattering of neutrons on ^{12}C, which is the dominant reaction in this isotope for $E_n \leq 20$ MeV, becomes visible in the diamond detector. Although the data in this E_n region is not as reliable due to the DAQ settings, see Section 12.1, it can be used to check the flight path L. With the obtained flight path the structures resulting from ^{12}C(n,el) at high neutron energies are visible at the expected E_n, see Figure 12.6(b), which confirms the

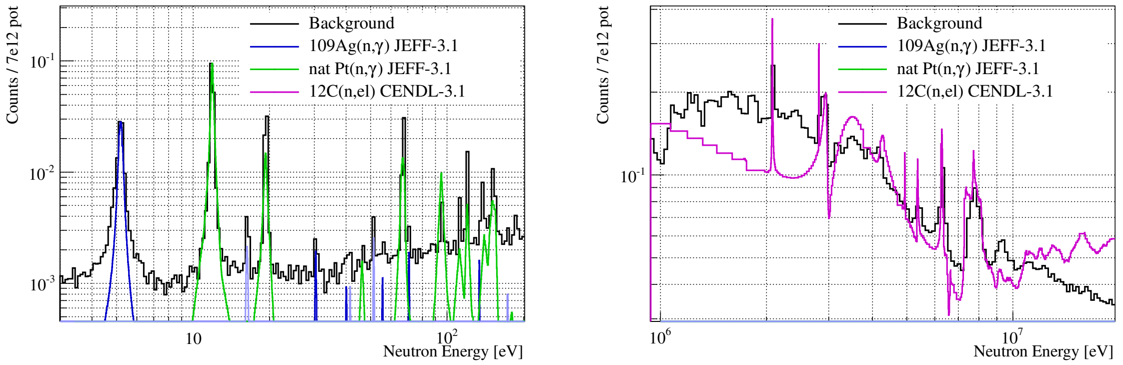

(a) Resonances caused by Ag(n,γ) and Pt(n,γ).

(b) Resonances caused by ^{12}C(n,el).

Figure 12.6: Result of the TOF to E_n calibration and comparison with the different cross-sections related to the resonant background.

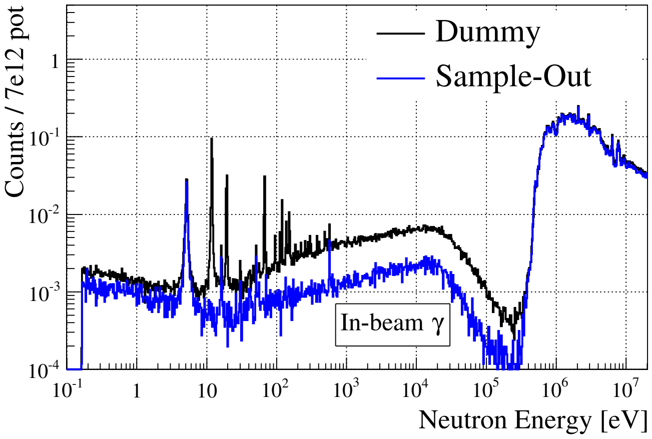

Figure 12.7: Background from the DM-D (Sample-out) in comparison with the Dummy measurement. The contribution of the in-beam γ increases by a factor 3 when the Pt foil is positioned in front of the detector.

TOF to E_n calibration.
When comparing the background spectrum from the Dummy measurement (Pt foil + DM-D backgrounds) with the Sample-out measurement (DM-D background only), see Figure 12.7, the resonances of capture reactions in Pt become visible and the background contribution in the low E$_n$ region increases by a factor 1.5. In addition, the Pt foil seems to enhance the γ-detection efficiency in the diamond detector. The contribution of the in-beam γ with predominantly $E_\gamma = 478$ keV, see Figure 2.4, increases by a factor 3. This indicates that the Pt foil acts like a photon converter, similar to a photo cathode in photo multiplier tubes (PMTs).

12.4 Analysis Conditions and Efficiency Corrections

As discussed before and shown in Figure 11.3, the different reaction products from the ^{6}Li(n,α), ^{59}Ni(n,α) and the background reactions produce signals of different amplitudes. The good energy resolution of the DM-D allows distinguishing between the different reactions of interest by selecting specific ranges of signal amplitude. This is shown in Figure 12.8, where the amplitude intervals for selecting α from ^{59}Ni(n,α)^{56}Fe and tritons from ^{6}Li(n,α)^{3}H for the cross-section and neutron fluence evaluation, respectively, are marked. The experimental data and the respective cuts for all channels of the DM-D can be found in Table A.4.

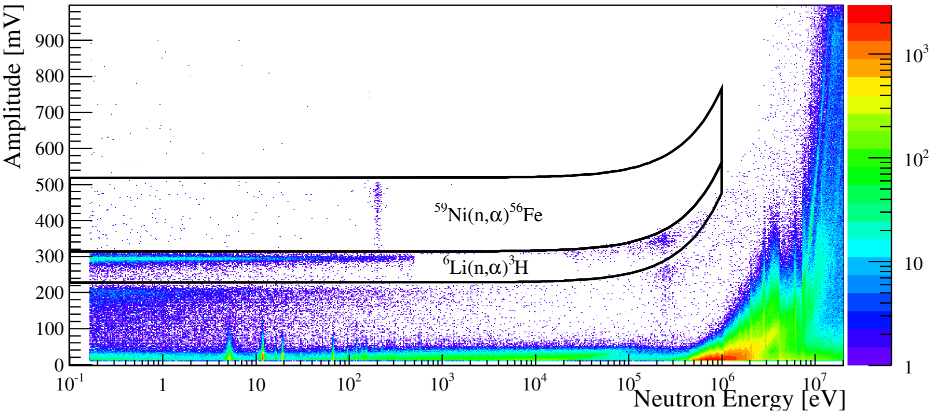

Figure 12.8: Amplitude over E_n for DIAM9 with the amplitude thresholds used to select only α from ^{59}Ni(n,α)^{56}Fe or tritons from ^{6}Li(n,α)^{3}H.

The analysis conditions for the thresholds $f(E_n)$ on the amplitude of the signals have the following neutron energy dependence:

$$f(E_n) = A + B \cdot E_n. \tag{12.3}$$

The constant A is related to the maximum particle energy for negligible neutron energies and the gain of the individual DM-D channel. With increasing neutron energy, the energy of the reaction products and the respective amplitude increases accordingly, which is accounted for by the term $B \cdot E_n$. The same analysis conditions were also applied to the Dummy measurement and the resulting E_n-spectrum was subtracted as background from the E_n-spectrum of the sample measurement. The resulting E_n-spectra from the scatter plot in Figure 12.8 are shown in Figure 12.9 together with the E_n-spectra from the corresponding Dummy measurement.

As some of the signals coming from either α particles from ^{59}Ni(n,α)^{56}Fe or tritons from ^{6}Li(n,α)^{3}H were not included in the data analysis because of these threshold settings, a counting-efficiency correction was applied. In order to test whether the shape of the simulated spectrum for the ^{59}Ni-α agrees with the measurement, the experimental particle spectra of all DM-D channels at the resonance in the interval 190 eV $\leq E_n \leq$ 220 eV were summed and the background subtracted. The particle spectrum outside the resonance, in the energy window 300 eV $\leq E_n \leq$

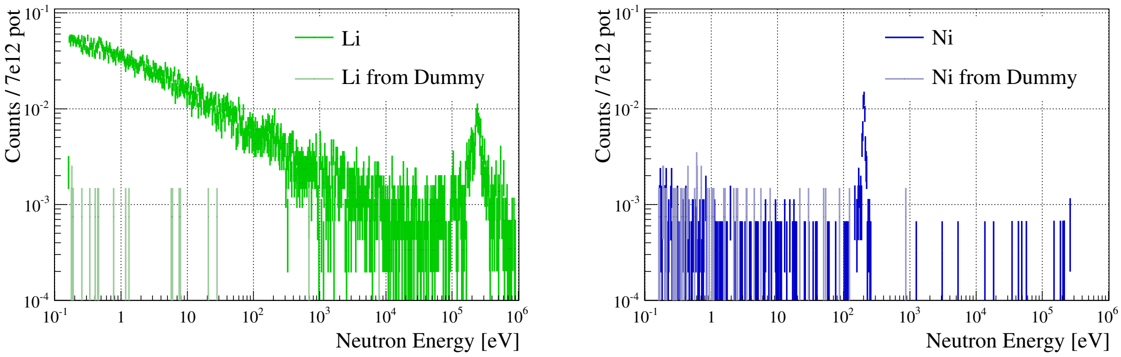

(a) E_n-spectra of tritons from ^{6}Li(n,α)^{3}H. (b) E_n-spectra of α from ^{59}Ni(n,α)^{56}Fe.

Figure 12.9: Comparison of E_n-spectra for the sample and Dummy measurement with DIAM9.

1 keV, was then subtracted from the spectrum at the resonance, to eliminate the contribution of ^{6}Li(n,α)t. The resulting spectrum, which is shown in Figure 12.10, reveals the contribution of ^{59}Ni(n,p)^{59}Co to the particle spectrum at the resonance. Although this experiment was focused on detecting α from (n,α) reactions, here it is demonstrated that it is also well suited for detecting lighter particles such as tritons and even protons with sufficient resolution.

The FLUKA simulation results for ^{59}Ni(n,α)^{56}Fe and ^{59}Ni(n,p)^{59}Co were convoluted with a Gaussian distribution taking into account the average energy resolution of the DM-D of dE = 78.5 keV at the ^{148}Gd peak, see Table 9.2, and compared to the measurement. The shape of the simulated α-spectrum of ^{59}Ni does not agree with the experimental spectrum and can hence not be used to find the efficiency correction as it would underestimate the number of sub-threshold ^{59}Ni-α. Therefore an analytic function had to be found which describes the experimental spectra to a higher accuracy.

A mirrored Landau distribution was found to be best suited to fit the experimental particle spectra [104], in order to compensate for the number of neglected signals due to the applied analysis conditions. This is shown in Figure 12.11 for one of the DM-D channels, where the applied thresholds are shown as vertical lines and the particle spectrum corresponds to the neutron energy interval 0.1 eV $\leq E_n \leq$ 1 keV. The fraction of the area that was cut off with the respective threshold was calculated with these distributions and the E$_n$-spectra were corrected for the loss of counts. The α spectra of ^{59}Ni were corrected by about 10%, while for the triton spectrum from ^{6}Li the corrections were 3%.

The systematic uncertainty of the efficiency correction was estimated by comparing the area of the experimental spectra and the Landau distributions, within the threshold boundaries. The fitting functions to the α-spectra of ^{59}Ni overestimated the experimental result by about 9%. As conservative uncertainty estimation, an overestimation of up to 20% was assumed. The associated uncertainty for the 10% correction to the counting rate is hence 2%, which is small in comparison to the statistical uncertainty of the measurement. The integral of the Landau distributions to the t-spectra of ^{6}Li underestimated the experimental count rate on average by 7%. With a conservative uncertainty estimation of 14%, the contribution for the 3% correction of the experimental count rate is 0.4% in total.

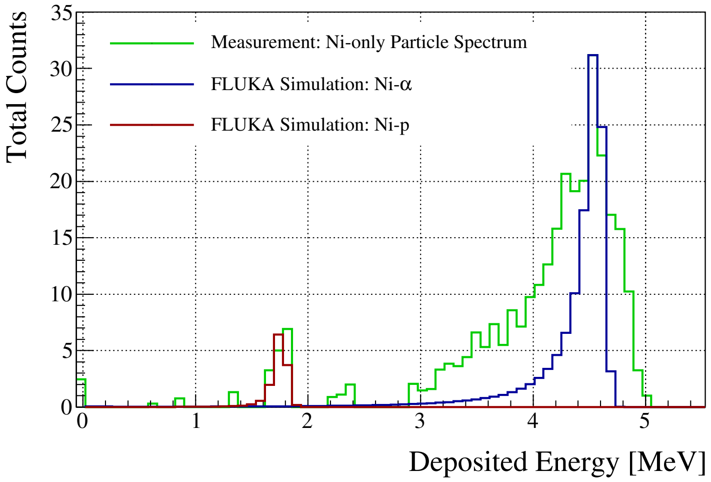

Figure 12.10: Sum of all particle spectra at the resonance (190 eV $\leq E_n \leq$ 220 eV), where the spectra outside the resonance were subtracted. The protons of ^{59}Ni(n,p)^{59}Co are visible at the corresponding energy of 1.8 MeV, and the alphas at 4.8 MeV. The results of the FLUKA simulations were convoluted with the average energy resolution of the DM-D of $dE = 78.5$ keV (^{148}Gd calibration at $E_\alpha = 3.183$ MeV).

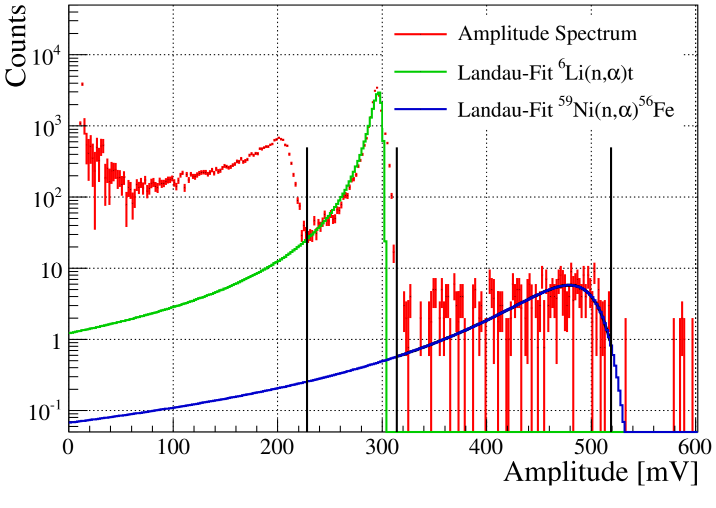

Figure 12.11: Amplitude spectrum of DIAM9 for $E_n \leq$ 1 keV. The set thresholds are indicated as vertical lines. The Landau-fit which was used for the efficiency correction is shown in blue for the α-spectrum of ^{59}Ni and in green for the t-spectrum of ^{6}Li.

Both reaction products of interest, ^{6}Li-tritons and ^{59}Ni-α, can be assumed to be emitted isotropically at the neutron energies of interest, and thus the geometric efficiency is considered about 50%. Due to the very thin layers on the sample, the possible absorption of an outgoing particle in the sample is assumed to be equally likely for both α from ^{59}Ni and t from ^{6}Li and was hence not corrected for, as it cancels out in the analysis. This was confirmed by the FLUKA simulations, which resulted in a total efficiency ε for the experimental setup of 45.7% for both ^{59}Ni-α and ^{6}Li-t, taking the absorption as well as the geometry into account.
In Table A.5 the particle spectra in units of deposited energy, the thresholds and the corresponding Landau distributions for all channels are shown. For the DOID the α and tritons of ^{6}Li(n,α)^{3}H cannot be distinguished well, which prevents a reliable determination of the BIF. Hence the data from this channel was not taken into account for the cross-section evaluation.

12.5 Reaction Yield Calculation and resulting Cross-Section

To obtain the experimental reaction yield, the measured E_n-spectra have to be divided by the neutron fluence. As each detector sees only a fraction of the beam, the so-called Beam Interception Factor (BIF) needs to be calculated for each diode. In order to obtain the beam interception factor (BIF) for each individual diode, the E_n-spectra of the Li-tritons were corrected for the loss of counts due to the analysis conditions and divided by the n_TOF evaluated neutron fluence [33], which gives the experimental Li-Yield (Y_{ex}). The expected reaction yield (Y_{th}), calculated with Equation 3.4, was then compared to the experimental spectrum, see Figure 12.12(a). To calculate Y_{th}, the areal density of the sample, $n_{\mathrm{Li}} = (2.31 \pm 0.06)\cdot 10^{-6}$ ^{6}Li atoms/barn, and the ^{6}Li(n,α)^{3}H cross-section given by the ENDF/B-VII.0 database was used. The ratio Y_{ex}/Y_{th}

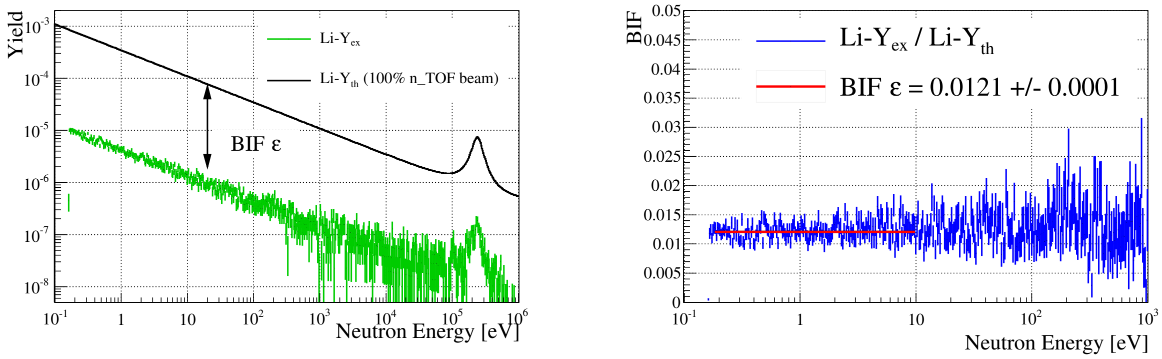

(a) Measured Li-yield (Y$_{ex}$) and expected Li-yield (Y$_{th}$). The ratio gives BIF$\cdot\varepsilon$.

(b) Evaluation of BIF$\cdot\varepsilon$, by a linear fit for $E_n \leq$ 10 eV.

Figure 12.12: Evaluation of the product of beam-interception factor and geometrical efficiency BIF$\cdot\varepsilon$ for DIAM9.

results in the product BIF·ε as a scaling factor for the n_TOF evaluated neutron fluence, see Figure 12.12(b).
The ^{6}Li(n,α)^{3}H reaction is anisotropic at neutron energies above 10 eV [105]. The outgoing tritons show forward peaking, which would lead to an overestimation of the neutron fluence. To avoid this, the linear fit to the ratio Y_{ex}/Y_{th} for BIF·ε was restricted to $E_n \leq 10$ eV. The neutron fluence at n_TOF is known to a high accuracy, as it was measured with various detectors using different reference samples and correlated to FLUKA simulations of the facility for the shape of the fluence spectrum. The determination of the product BIF·ε in the low neutron energy region and scaling the evaluated neutron fluence of n_TOF is hence the most reliable method for the determination of the neutron fluence for this experiment.
The product BIF·ε and BIF·ε normalized to the area of the respective diode (BIF·ε/mm^2) are listed in Table 12.1. The DM-D was apparently not perfectly centered in the neutron beam. The beam spot was shifted to the bottom by 0.8 mm and to the right by 1.9 mm.

Table 12.1: The resulting BIF·ε from the linear fit to the ratio Y_{ex}/Y_{th} and BIF·ε normalized to the area of the respective diode (BIF·ε/mm^2) for all channels of the DM-D. The neutron-beam spot was apparently shifted to the bottom right during the measurement. According to FLUKA simulations, the efficiency ε of the experimental setup is 45.7%.

Channel	**DIAM8**	**DIAM1**	**DIAM9**
BIF·ε	0.0095 ± 0.0001	0.0153 ± 0.0002	0.0121 ± 0.0001
BIF·ε/mm^2	$5.7\cdot10^{-4}$	$7.1\cdot10^{-4}$	$7.5\cdot10^{-4}$
Channel	**DIAM3**	**DIAM4**	**DIAM5**
BIF·ε	0.0140 ± 0.0002	0.0201 ± 0.0003	0.0196 ± 0.0002
BIF·ε/mm^2	$7.2\cdot10^{-4}$	$10.4\cdot10^{-4}$	$10.1\cdot10^{-4}$
Channel	**DOID**	**DIAM2**	**DIAM6**
BIF·ε	0.0147 ± 0.0006	0.0179 ± 0.0002	0.0138 ± 0.0002
BIF·ε/mm^2	$7.0\cdot10^{-4}$	$8.7\cdot10^{-4}$	$9.6\cdot10^{-4}$

To obtain the Ni-yield the E_n-spectra for ^{59}Ni-α were corrected for the loss of counts due to the analysis conditions and divided by the neutron fluence, scaled with the respective BIF·ε. In Figure 12.13 the resulting yield for one channel of the DM-D is shown. The yields from all DIAM channels of the DM-D were finally averaged and rebinned.

To obtain the ^{59}Ni(n,α)^{56}Fe cross-section the thin target approximation was assumed, see Equation 3.6, and the experimental yield was divided by the areal density of ^{59}Ni on the sample, $n_{\mathrm{Ni}} = (8.9 \pm 0.3) \cdot 10^{-7}$ atoms/barn. The determined cross-section is shown in Figure 12.14 in the top panel. In the bottom panel the corresponding statistical uncertainty is illustrated. The resonance at $E_n = 203$ eV could be resolved reasonably well with 100 bins per decade. Outside the resonance the binning was reduced to 2 bins per decade, to achieve an acceptable statistical uncertainty below 20%. The resulting cross-section is compared to previous measurements in the following, concluding Chapter.
For determining the systematic uncertainty of the resulting cross section, the sample specifications and the counting-efficiency correction using the Landau fit to the particle spectra have to be taken into account in addition to the uncertainty of the ^{6}Li(n,α)t cross-section from ENDF/B-

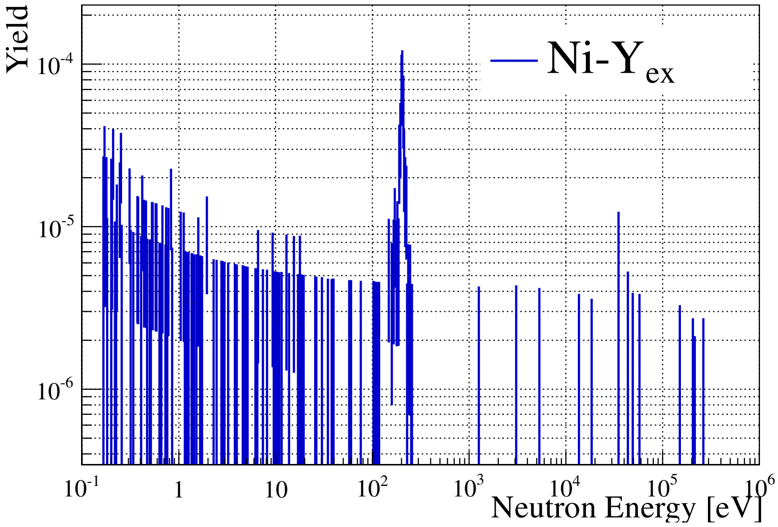

Figure 12.13: ^{59}*Ni(n,*α*)*^{56}*Fe yield for DIAM9.*

Table 12.2: Contributions to the systematic uncertainty of the measurement and cross-section evaluation.

Contribution	Uncertainty
Sample:	
^{59}Ni Mass	2.8%
^{6}Li Mass	2.4%
Correction for Analysis Conditions:	
Counting-Efficiency Correction for ^{59}Ni-α	2%
Counting-Efficiency Correction for ^{6}Li-t	0.4%
^{6}Li(n,α)t Cross-Section:	
ENDF/B-VII.0 for $E_n \leq 0.1$keV	0.3%
Total Systematic Uncertainty	4.2%

VII.0. The magnitude of the different contributions to the systematic uncertainty are listed in Table 12.2. With a conservative estimation, the systematic uncertainty for the resulting ^{59}Ni(n,α)^{56}Fe cross-section is 4.2%, which is at the level of the statistical uncertainty at the peak of the resonance, as seen in Figure 12.14. The uncertainty of the determined cross-section with the DM-D is dominated by the limited count rate of the experiment everywhere else.

The aim of the measurement was to determine the resonance integral of the dominant resonance at $E_n = 203$ eV. To extend the measurement to higher energies and resolve the resonances in the keV region, the integral neutron fluence would have to be at least one order of magnitude higher than at the present, horizontal flight path at n_TOF in this neutron energy region. For the future, vertical flight path at n_TOF an increase of a factor 25 in the neutron fluence is expected from simulations [32]. Although the resolution at this flight path will be a factor 10 worse in comparison to the 200 m flight path, the resonances in ^{59}Ni are found at a quite low neutron energy and thus it is recommended to measure the ^{59}Ni(n,α)^{56}Fe cross-section in the future at this facility. The experimental results in the keV neutron energy region are of particular interest for the astrophysical applications.

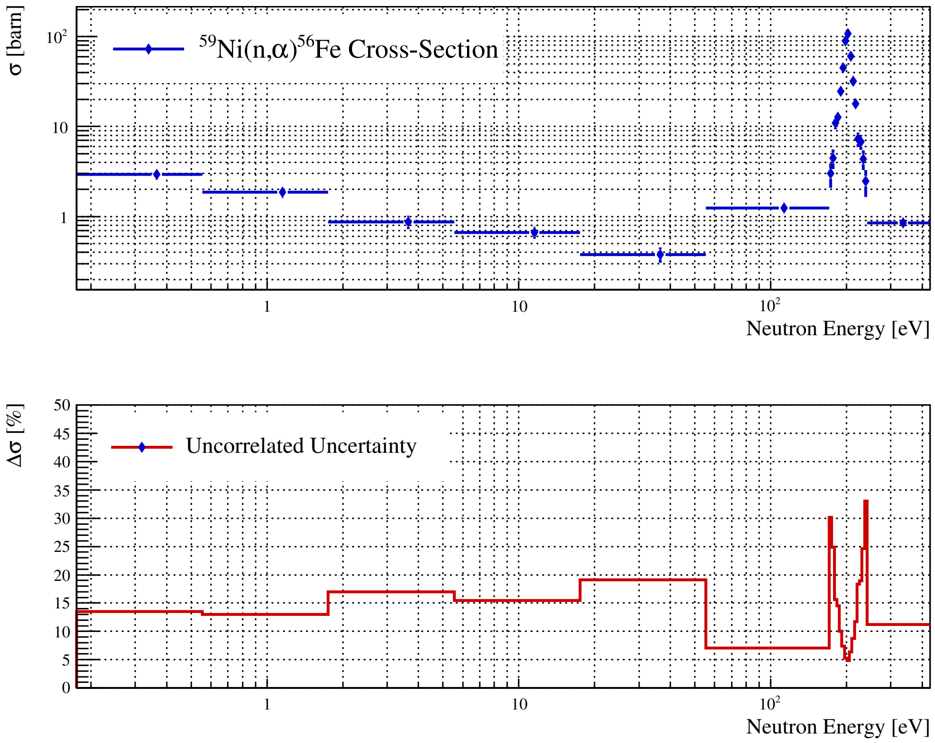

Figure 12.14: ^{59}Ni(n,α)^{56}Fe cross-section measured with the DM-D at n_ TOF, top panel, with the statistical uncertainty for each bin shown in the bottom panel. Following a conservative estimation, the correlated uncertainty is 4.2%.

Chapter 13

Conclusions on the Measurement Results

The aim of the ^{59}Ni(n,α)^{56}Fe cross-section measurement at n_TOF was to determine the integral of the dominant resonance at $E_n = 203$ eV in order to solve the sizable discrepancies observed between the two previously existing data of Harvey [2] and Koehler [3]. In Figure 13.1 the resulting cross-section from the measurement (labelled 'Weiss') is compared to the other measurements and evaluated nuclear data. The cross-sections of Harvey, Koehler and n_TOF at the dominant resonance were integrated in the neutron energy window $170 \leq E_n \leq 240$ eV, giving the following integral values.

Measurement	Resonance Integral ($170 \leq E_n \leq 240$ eV)	Statistical Uncertainty [%]
Harvey 1976	(2143 ± 7)	0.3
Koehler 1999	(1780 ± 11)	0.6
Weiss 2012	(2000 ± 48)	2.4

The resonance integral of the measurement performed at n_TOF lies in between the other two available measurements, which were both performed at the ORELA facility of the Oak Ridge National Laboratory. The same sample was used for all three measurements. With a cross-section 6.7% lower than Harvey and 12.4% higher than Koehler, the present results confirm rather the measurement performed by Harvey. Regarding the cross section values in the evaluated nuclear data files all libraries overestimate the cross-section, by almost 30% with respect to our results, the strength of the resonance. The closest to the existing data is ENDF/B-VI.8, which is just slightly above Harvey's data.

At lower neutron energies the obtained cross-section from the measurement with the DM-D agrees within error margins with the evaluated nuclear data libraries, while the measurement of Koehler lies systematically below the measurement at n_TOF. This is shown in Figure 13.2, where the obtained cross-section is compared to the other measurements and evaluated nuclear data for $0.17 \leq E_n \leq 430$ eV.

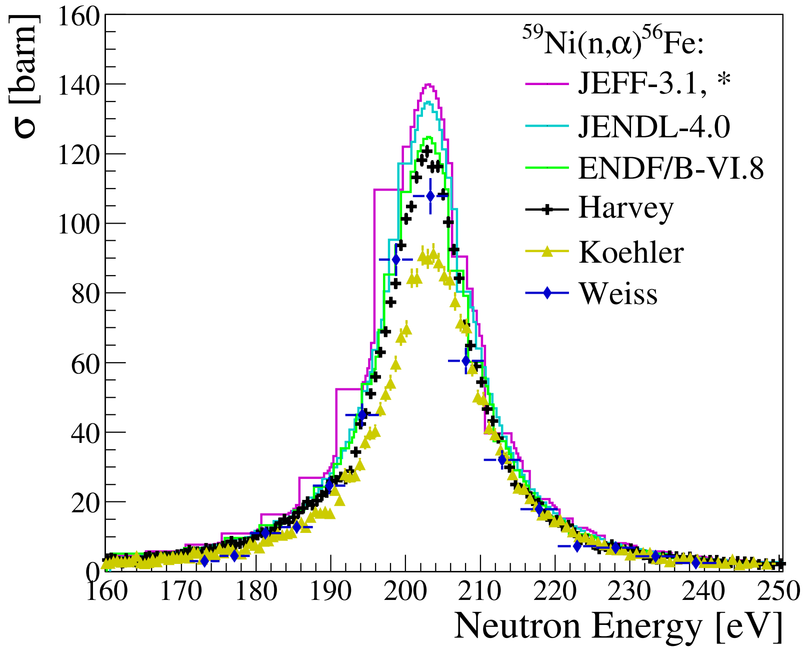

*Figure 13.1: ^{59}Ni(n,α)^{56}Fe cross-section at the dominant resonance, experimental and evaluated nuclear data. The libraries ROSFOND-2010, ENDF/B-VII.1 and ENDF/B-VII.0 are equivalent to JEFF-3.1 *.*

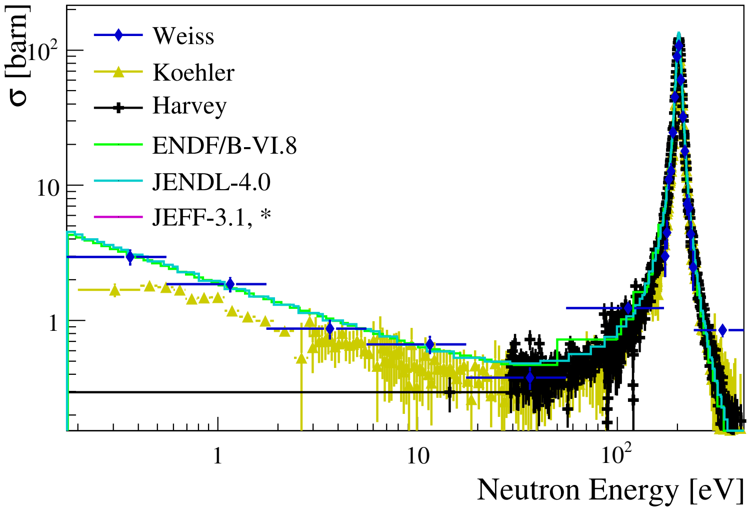

*Figure 13.2: ^{59}Ni(n,α)^{56}Fe cross-section, experimental and evaluated nuclear data. The libraries ROSFOND-2010, ENDF/B-VII.1 and ENDF/B-VII.0 are equivalent to JEFF-3.1 *.*

Part IV

Summary and Outlook

The aim of this PhD project was to introduce a new technology for (n,α) reaction cross-section measurements at the neutron time-of-flight facility (n_TOF) at CERN. The Diamond Mosaic-Detector (DM-D), a spectroscopic, in-beam detector consisting of an array of eight sCVD diamond sensors and one DOI sensor, was built in the framework of this thesis. A close-up picture of the detector is shown in Figure 13.3.

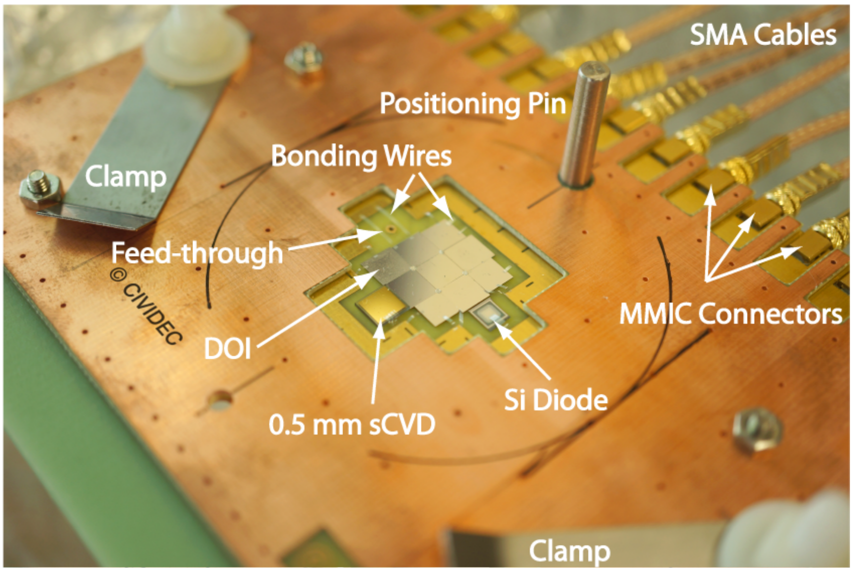

Figure 13.3: The Diamond Mosaic-Detector.

The DM-D can be used for spectroscopic measurements of various charged particles in the following energy ranges:

Particle	Energy Range for Spectroscopy with the DM-D
α	125 keV $\leq E_\alpha \leq$ 22 MeV
triton	125 keV $\leq E_t \leq$ 9 MeV
proton	125 keV $\leq E_p \leq$ 6 MeV
electron	125 keV $\leq E_{e^-} \leq$ 200 keV

where the thickness of the diamond sensors ($d = 150\mu$m) and 5σ of the noise level of the electronics in the experimental setup give the upper and lower limits, respectively. The detector is described in the second part of this thesis with a detailed discussion on the performance.
The ^{59}Ni(n,α)^{56}Fe cross-section was measured with the DM-D at n_TOF in 2012. For the measurement, a metallic Ni sample of 100 nm thickness, which was 95% enriched in ^{59}Ni and coated with 400 nm of ^{6}LiF was used. Due to the high resolution of the DM-D the ^{59}Ni-α and the ^{6}Li-tritons could reliably be selected in the amplitude spectra. An efficiency correction was applied in the data analysis for the implemented thresholds. The resonant background from the measurement of the sample backup Pt-foil was used for the TOF to E_n calibration. The product of beam-interception factor and geometrical efficiency (BIF$\cdot\varepsilon$) was determined with the ^{6}Li spec-

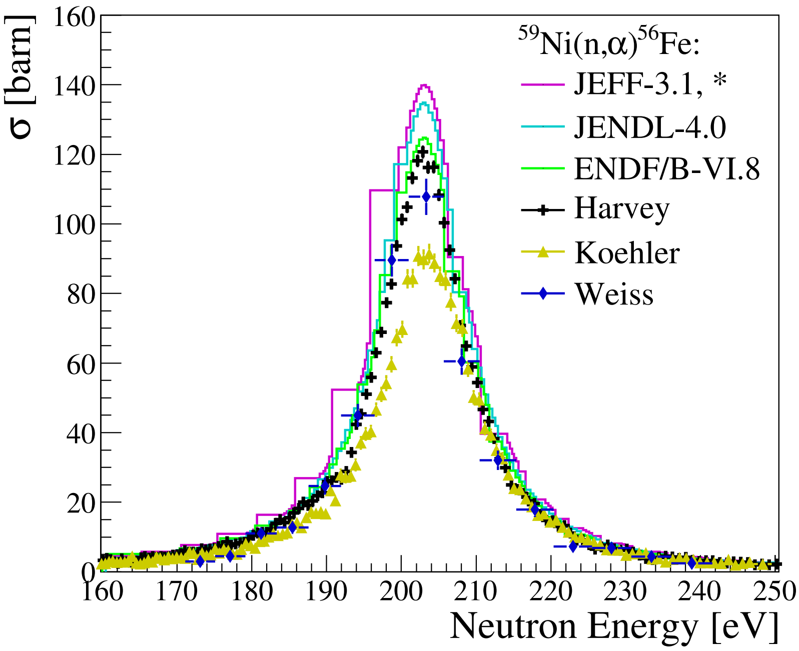

Figure 13.4: ^{59}*Ni(n,*α*)*^{56}*Fe cross-section at the dominant resonance, experimental and evaluated nuclear data. The libraries ROSFOND-2010, ENDF/B-VII.1 and ENDF/B-VII.0 are equivalent to JEFF-3.1 *.*

trum and the n_TOF evaluated neutron fluence was scaled accordingly for the determination of the ^{59}Ni(n,α) reaction yield. The channels of the DM-D were analyzed separately to account for the different gains and resolution of the channels, before the data was merged to obtain the final experimental yield. The thin target approximation was assumed in the final cross-section calculation.

The aim of the measurement was to determine the integral of the dominant resonance at $E_n = 203$ eV in the ^{59}Ni(n,α)^{56}Fe cross-section to clarify the sizable discrepancies observed between previous measurements by Harvey [2] and Koehler [3]. With 6.7% lower than Harvey and 12.4% higher than Koehler, the present results confirm rather the measurement performed by Harvey. The resulting cross-section at the resonance is compared to the previous measurements and to evaluated nuclear data files in Figure 13.4, where the latter all lie above the available measurements. For the experimental data the statistical uncertainties are given. The total systematic uncertainty of the cross-section resulting from the measurement with the DM-D at n_TOF is 4.2%.

The DM-D has proven to be well suited for (n,α) measurements at n_TOF, for reactions where the Q-value is above 1 MeV. This restriction is due to the background originating from capture reactions in the in-beam materials. For a mean alpha energy $E_\alpha \geq 1$ MeV the particle spectra can reliably be distinguished from the background. The measurement with the DM-D at the current horizontal flight path at n_TOF allowed to measure the integral of the dominant resonance of the ^{59}Ni(n,α)^{56}Fe cross-section at $E_n = 203$ eV with a statistical uncertainty of 2.4%. For astrophysical applications the cross-section for 1 keV $\leq E_n \leq$ 300 keV is of particular interest, which requires a higher neutron fluence to the experiment. The vertical flight path at n_TOF (EAR2), which will be operational from July 2014 onwards, will offer a neutron fluence of a factor 25 higher in the keV region. At this facility the strongest resonances in the keV region of the ^{59}Ni(n,α)^{56}Fe cross-section can be measured, and in addition the cross-section can be determined down to thermal energies with better statistical uncertainties. It is hence recommended to repeat the measurement for this reaction at n_TOF EAR2 in the future.

The unique property of sCVD diamond, which shows the ionization profile in the detector current, can be exploited to further improve the background rejection in a spectroscopic measurement. The applicability of such a pulse shape selection for (n,α) measurements is currently investigated in a PhD thesis [89] and the implementation of an online real-time analysis will be implemented in the framework of an additional PhD [106], both at the Vienna University of Technology. The combination of this data analysis with the DM-D would be a very attractive solution for future (n,α) measurements at n_TOF EAR2, where the γ-background is expected to be at least a factor 10 higher than in the current horizontal flight path. In addition, the fast response of the current amplifier that would be used for the pulse shape analysis measurement will be favorable at this shorter flight path of 20 m length.

The lower limit for (n,α) measurements with the DM-D is $E_\alpha \geq 1$ MeV, due to the background contribution from in-beam materials like Ag. A further improvement of the detector would be possible with a large area spectroscopic diamond sensor, where the backup materials of the detector could be removed from the beam. Such a detector design was successfully tested in the past at n_TOF with a pCVD diamond substrate [65]. The DOI material is presently the only potential candidate for a large area spectroscopic diamond and the latest improvements of this material are promising for the eventual future development of a highly transparent diamond (n,α)-detector. With a non-metallic sample backup-foil the lower limit for such a detector could be reduced down to $E_\alpha = 400$ keV.

Appendix A

Data from the Diamond Mosaic-Detector

	^{148}Gd $E_\alpha = 3.183$ MeV (100%)				^{239}Pu $E_\alpha = 5.156$ MeV (73.2%)			
Diode	μ [fC]	σ [fC]	dE/E [%]	dE [keV]	μ [fC]	σ [fC]	dE/E [%]	dE [keV]
DIAM1	Gauss fit not applicable				50.7	0.9	1.8	93.5
DIAM2	44.1	0.7	1.5	47.5	73.8	0.6	0.7	38.2
DIAM3	44.0	0.6	1.3	40.9	73.4	0.5	0.7	36.5
DIAM4	31.1	0.5	1.5	46.3	51.8	0.4	0.8	40.2
DIAM5	42.1	0.5	1.3	40.0	70.2	0.5	0.7	37.0
DIAM6	35.1	2.9	8.3	260.7	68.4	2.4	3.5	177.7
DIAM8	Gauss fit not applicable				71.3	0.7	1.0	49.5
DIAM9	42.1	0.5	1.2	36.5	69.8	0.6	0.8	41.8

	^{241}Am $E_\alpha = 5.486$ MeV (85.2%)				^{244}Cm $E_\alpha = 5.805$ MeV (76.4%)			
Diode	μ [fC]	σ [fC]	dE/E [%]	dE [keV]	μ [fC]	σ [fC]	dE/E [%]	dE [keV]
DIAM1	54.1	1.0	1.8	97.0	57.3	0.7	1.2	66.9
DIAM2	78.6	0.5	0.7	37.3	83.3	0.5	0.5	31.4
DIAM3	78.3	0.5	0.7	36.8	83.0	0.5	0.6	32.6
DIAM4	55.2	0.4	0.7	40.2	58.5	0.4	0.6	35.5
DIAM5	74.8	0.5	0.7	37.6	79.4	0.5	0.6	34.9
DIAM6	73.2	1.9	2.6	140.1	77.9	1.1	1.4	78.5
DIAM8	76.1	0.7	0.9	47.6	80.7	0.5	0.7	38.6
DIAM9	74.4	0.5	0.7	38.8	79.0	0.5	0.6	32.9

Table A.1: Results of the Gauss fits to the peaks corresponding to α form the four isotopes contained in the calibration source. The main α-energy for each isotope with the corresponding intensity is given beyond the isotopes name. For ^{239}Pu, ^{241}Am and ^{244}Cm a summation of multiple Gauss functions, corresponding to multiple E_α, was used as fit function.

Table A.2: The Diamond Mosaic-Detector as seen from the neutron beam. The dimensions of the diodes are given in mm x mm x mm. The 500 µm thick sCVD diamond and the Si diode were intended to be used for additional background measurements.

DIAM8 Diamond ID#: SC01624-2 Dimensions: 4.1 x 4.1 x 0.15 Material: sCVD	**DIAM1** Diamond ID#: SC01266-1 Dimensions: 4.5 x 4.8 x 0.15 Material: sCVD	**DIAM9** Diamond ID#: SC01625-2 Dimensions: 4.0 x 4.0 x 0.15 Material: sCVD	
DIAM3 Diamond ID#: SC01274-2 Dimensions: 4.4 x 4.4 x 0.15 Material: sCVD	**DIAM4** Diamond ID#: SC01444-2 Dimensions: 4.4 x 4.4 x 0.15 Material: sCVD	**DIAM5** Diamond ID#: SC01449-2 Dimensions: 4.4 x 4.4 x 0.15 Material: sCVD	Not used Dimensions: 3.5 x 3.5 x 0.1 Material: Si
DOID Diamond ID#: MFDIA1034 Dimensions: 4.6 x 4.6 x 0.15 Material: DOI	**DIAM2** Diamond ID#: SC01266-2 Dimensions: 4.7 x 4.4 x 0.15 Material: sCVD	**DIAM6** Diamond ID#: SC01457-1 Dimensions: 3.8 x 3.8 x 0.15 Material: sCVD	
	sCVD Diamond ID#: SC01878 Dimensions: 4.6 x 4.6 x 0.5 Material: sCVD		

Table A.3: Current over Voltage behavior of the Diamond Mosaic-Detector. DIAM1 and DIAM8 show a leakage current that is 2-3 orders of magnitude to high for negative voltage.

DIAM8

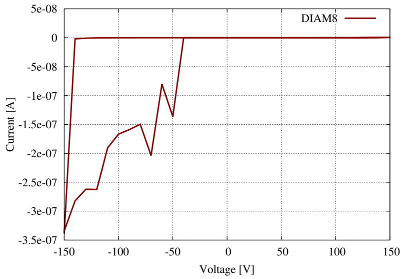

DIAM1

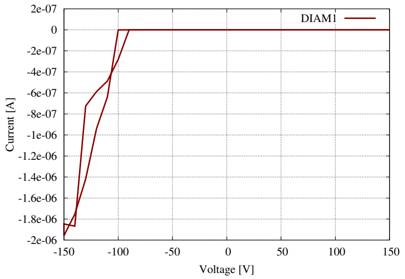

DIAM9

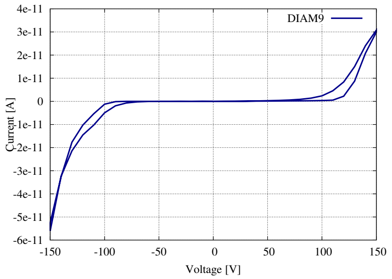

DIAM3

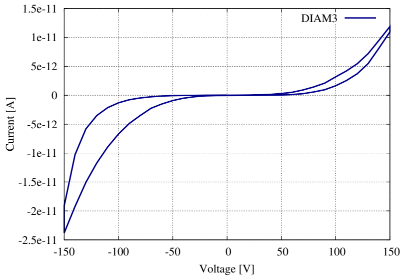

DIAM4

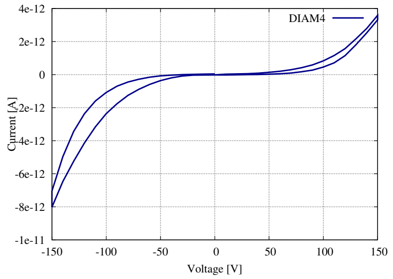

DIAM5

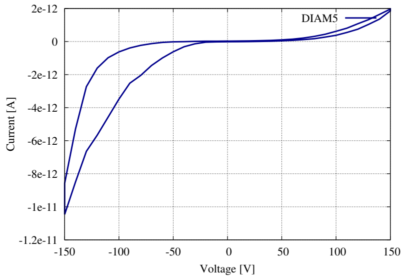

DOID

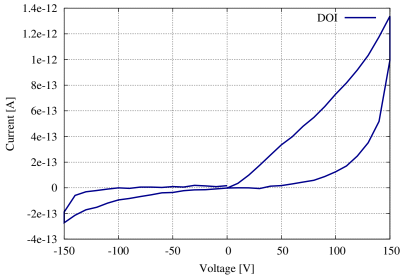

DIAM2

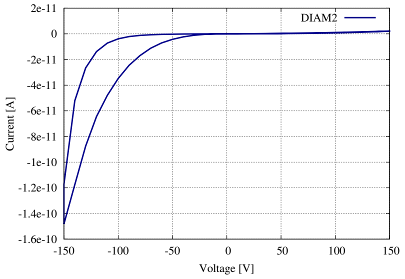

DIAM6

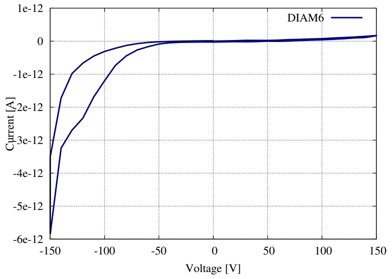

Table A.4: Experimental data recorded with the Diamond Mosaic-Detector during the sample measurement (^{59}Ni, ^{6}Li) at n_ TOF.

DIAM8

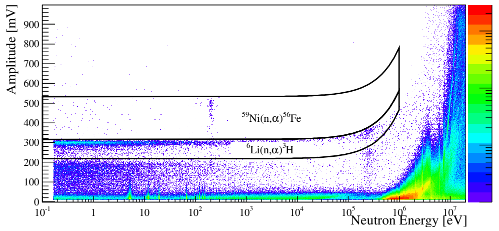

DIAM1

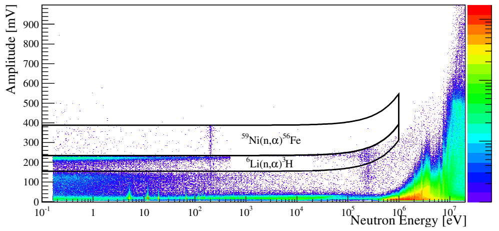

DIAM9

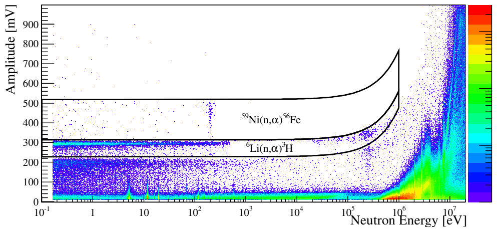

DIAM3

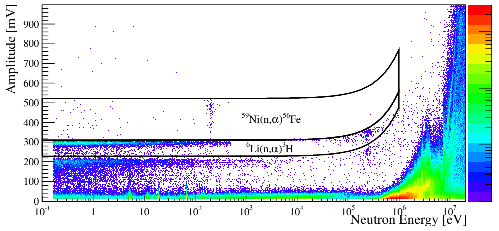

DIAM4

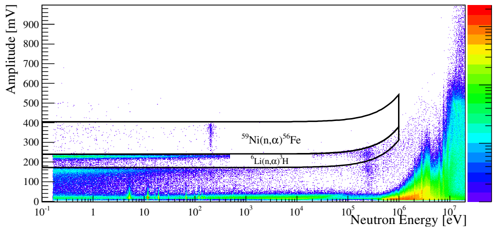

DIAM5

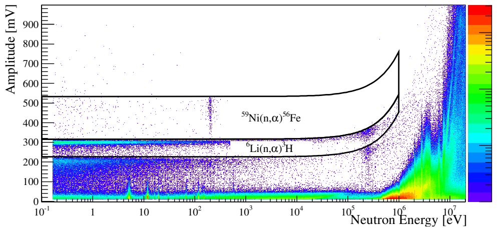

DOID

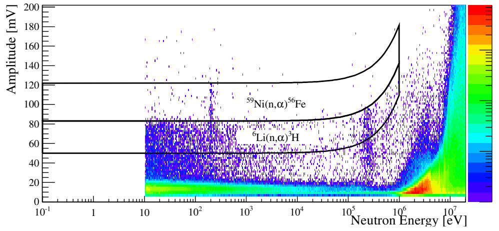

DIAM2

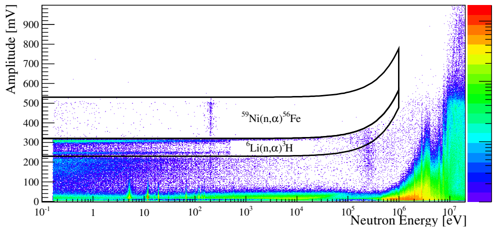

DIAM6

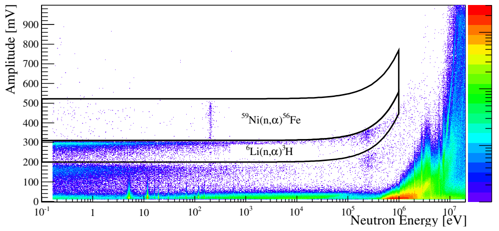

Table A.5: Particle spectra for $E_n \leq 500$ keV, recorded with the Diamond Mosaic-Detector during the sample measurement (^{59}Ni, ^{6}Li) at n_TOF. The Landau fit to the distribution corresponding to tritons of ^{6}Li(n,α)^{3}H and α of ^{59}Ni(n,α)^{56}Fe is indicated in green and blue respectively. The implemented thresholds are indicated as vertical lines.

DIAM8 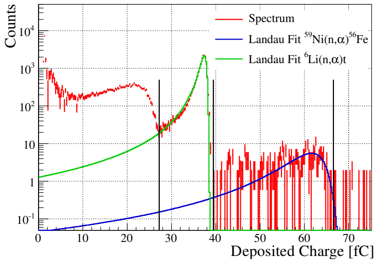 	**DIAM1** 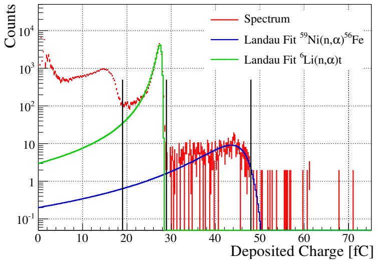 	**DIAM9** 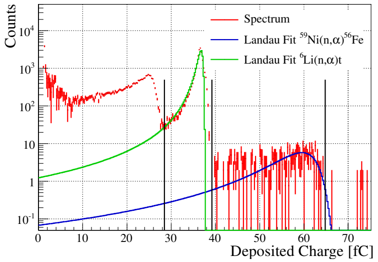
DIAM3 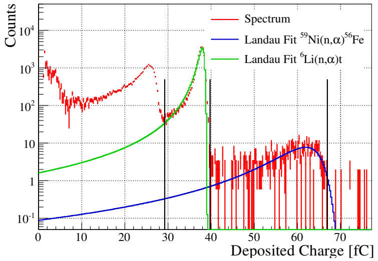 	**DIAM4** 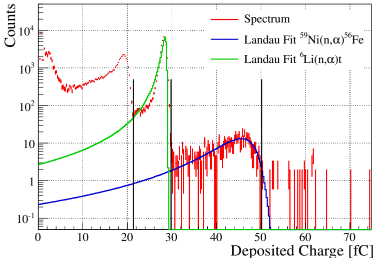 	**DIAM5** 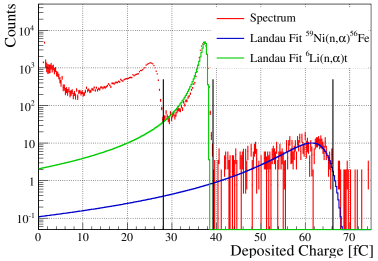
DOID 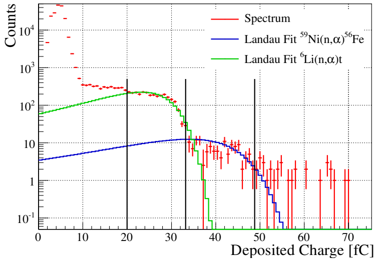 	**DIAM2** 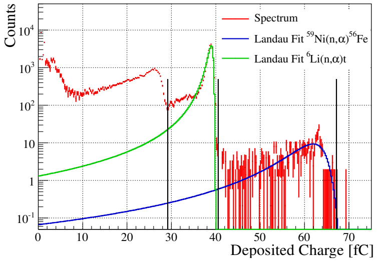 	**DIAM6** 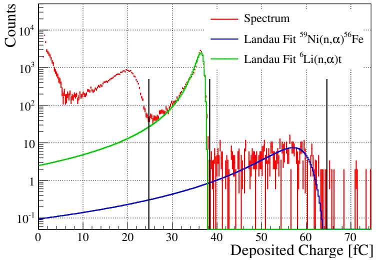

List of Figures

1.1 Schematic sketch of the reaction path of the s and r process on the chart of nuclides, picture taken from [10]; s- and r-only isotopes are indicated with the respective letter. The abundance as a function of the mass number is displayed on the top left. The peaks in this distribution are related to the small capture cross-section of neutron magic nuclei. 7

1.2 Chart of nuclides in the region of Fe and Ni. A neutron capture reaction in the secondary s process seed ^{58}Ni forms ^{59}Ni. At this isotope the capture reaction (light gray arrows) is competing with the (n,α) (green arrow) and (n,p) (red arrow) reaction. The natural decay of the radioactive ^{59}Ni is indicated in dark gray. . . 7

1.3 Microscopic picture of inter-granular (IGSCC) and trans-granular (TGSCC) stress corrosion cracking, picture from [18]. 8

1.4 Existing experimental and evaluated data for the ^{59}Ni(n,α)^{56}Fe reaction. The libraries ROSFOND-2010, ENDF/B-VII.1 and ENDF/B-VII.0 are equivalent to JEFF-3.1 *. 9

1.5 Schematic experimental setup for (n,α) cross-section measurements. The neutron beam, together with the in-beam γ-background, impinges on the sample, detector and the surrounding materials. 10

2.1 Schematic layout of the n_TOF facility at CERN, picture from [33]. The pulsed proton beam, which is delivered by the CERN Proton Synchrotron (PS) impinges on the Pb spallation target. The experimental hall is situated about 200 m behind the target at the end of the horizontal beam line. 14

2.2 Schematic beam line of the n_TOF facility at CERN, picture from [33]. 15

2.3 Simulated particle spectra at n_TOF for water and borated water as neutron moderator respectively, picture from [33]. The in-beam γ-ray background ($E_\gamma \geq$ 1 MeV) is reduced by more than one order of magnitude, when borated water is used. 16

2.4 Simulated photon energy spectra at n_TOF with water and borated water as neutron moderator, picture from [33]. The main contribution of the delayed γ when borated water is used, comes from the ^{10}B(n,α)^{7}Li* reaction. 16

2.5 Evaluated n_TOF neutron flux in the configuration with the capture collimator (18 mm diameter) with water and borated water as moderator. The systematic and statistical uncertainties are given in the bottom panel, see Reference [33] for details. 17

2.6 Different components contributing to observed resonance widths at n_TOF, picture from [36]. Below 3 keV, the Doppler broadening of resonances is dominating. Above this energy, the moderation process in the target and in the surrounding moderator has the biggest influence on the shape of the observed resonances. The proton pulse width starts dominating at even higher E_n. The resonance spacing and intrinsic resonance widths are given for ^{232}Th(n,γ). 18

2.7 Time-of-flight measurement principle. 19

2.8 Multiple γ-flash signals recorded during a test beam at n_TOF in 2010 with a sCVD diamond detector in combination with a 2 GHz current amplifier. The parabolic fit shows a FWHM of 16 ns, corresponding to 6.8 ns rms from the primary proton beam. Signals on the right hand side correspond to signals created by high energetic neutrons. 20

3.1 Schematic view of the formation of a compound nucleus $^{\mathrm{A+1}}$X followed by the emission of a γ ray, corresponding to radiative neutron capture, from [44]. Typical values of the average level spacing (D) at different excitation energies are given as well as the neutron separation energy S_n. 24

3.2 Total cross-sections for various isotopes. σ is proportional to $1/\sqrt{E_n}$ at low neutron energies for all isotopes. For ^{1}H, ^{12}C and ^{56}Fe the elastic scattering is the dominant reaction at intermediate energies, where σ is constant. The resolved resonance region can be seen for ^{56}Fe and ^{235}U. 25

3.3 Binding Energy per nucleon as a function of the atomic mass number A. Elements near Fe have the highest nuclear binding energy. 26

3.4 Fission cross-sections for ^{235}U and ^{238}U from the evaluated nuclear data library JEFF-3.1. 27

4.1 Mean energy loss of positive muons in Cu as a function of $\beta\gamma = p/Mc$, from [48]. The different regions of the approximations, as described in the text, are indicated. 31

4.2 bla . . . 32

4.3 Specific energy loss along the track of an α particle with several MeV initial energy, from [49], for a single α and a beam of α particles. The difference between the two curves is due to energy and range straggling. . . . 33

4.4 Calculated straggling functions $f(\Delta/x) = f(\mathrm{d}E/\mathrm{d}x)$ for $\beta\gamma = 3.6$ particles in Ar, from [51]. While the most probable value varies with the thickness x of the absorber, the mean energy loss is the same for all x. . . . 33

4.5 Photon total cross section and contributions of different interactions as a function of E_γ in Carbon (a) and Lead (b), picture from [48]:
$\sigma_{p.e.}$ = photoelectric effect,
$\sigma_{Rayleight}$ = Rayleight scattering,
$\sigma_{Compton}$ = Compton scattering,
κ_{nuc} = nuclear field pair production,
κ_e = electron field pair production,
$\sigma_{g.d.r.}$ = photo nuclear interactions (target nucleus breaks up). . . . 35

4.6 Cross-sections for different neutron-induced nuclear reactions on ^{12}C, the main isotope in diamond detectors. . . . 38

4.7 Deposited energy spectrum recorded with a sCVD diamond detector in a 14 MeV neutron beam, with an energy spread of FWHM = 0.2 MeV [53]. The peak at 8.3 MeV corresponds to α particles coming from the ^{12}C(n,α)^{9}Be reaction. . . . 39

5.1 Phase diagram of Carbon, picture from [54]. . . . 42

5.2 Unit cell of diamond with a the cubic lattice constant, picture from [23]. . . . 42

5.3 Measurement of the drift velocity v_{dr} in sCVD diamond. The data was fitted using Equation 5.1 for the parameters μ_0 and v_s. The resulting low-field mobility is $\mu_{0,e^-} = (1530 \pm 160)$ cm^2/Vs and $\mu_{0,h^+} = (2660 \pm 160)$ cm^2/Vs for electrons and holes respectively. For the saturation velocities $v_{s,e^-} = (1.12 \pm 0.05) \cdot 10^5$ m/s and $v_{s,h^+} = (1.29 \pm 0.03) \cdot 10^5$ m/s resulted from the fit for electrons and holes respectively. . . . 46

5.4 Schematics of a diamond detector under positive bias voltage with thickness d, without (left) and with homogeneously distributed negative space charge $Q_{s}c$ in the bulk (right). The electric field results directly from the charge distribution and influences the shape of the current pulse which is induced by the α particle. . 48

5.5 Comparison of the theoretical and measured pulse shapes for a signal created by a ^{241}Am α in a 500 μm sCVD diamond sensor, which is operated at E = 1 V/μm, when e^{-}-drift is dominating the signal. 51

5.6 Measured pulse shapes in CVD diamond detectors. The 500 μm thick detectors are operated at E = 1 V/μm. The reduced efficiency of the pCVD material (black) can be seen in both cases. The signal is triangular, even for α particles, and has an exponential decay. The area of the signals is significantly smaller than the the area of the sCVD pulses (red). 52

5.7 Rectangular pulse shapes measured in a 14 MeV neutron beam. Signals dominated by the hole drift (red) as well as signals dominated by the electron drift (yellow) can be observed. The superposition of the two (blue) can be observed when the ionizing particle is created in the center of the detector [92]. 53

6.1 Equivalent circuit diagram of a diamond detector with capacitance C_d operated with a current amplifier in a 50 Ω system. 56

6.2 Simulated transfer function of the Cividec C2 current amplifier, picture from [93]. The cut-off frequencies f_l and f_u define the bandwidth B of the amplifier. 57

6.3 Equivalent circuit diagram of a diamond detector with capacitance C_d operated with a charge amplifier with feed-back capacitance C_f and resistor R_f in a 50 Ω system. 58

6.4 Equivalent circuit diagram of a voltage divider, which corresponds to a detector with resistance R_i read out with an oscilloscope with input impedance R_L. . . . 58

6.5 Different factors influencing the energy resolution of an experiment. The contribution of the used electronics is shown on the example of the Cividec C2 2 GHz current amplifier and the Cividec Cx spectroscopic charge amplifier [99]. The influence of different ADCs is drawn in green. For ΔE/E $\leq$ 0.1, equivalent to SNR $\geq$ 10, a reliable measurement can be performed. 60

6.6 Different factors influencing the energy resolution of the measurements with the DM-D. The input capacitance on the Cividec Cx amplifiers was about 35 fC. The data was recorded with an 8 bit ADC. The statistical uncertainty coming from the ionization process in the diamond detector (red) and the effect of the Al-electrodes of the DM-D (yellow) are less important than the electronics and the ADC. . . . 61

6.7 Rising edge of a signal; the noise level da is equivalent to the amplitude resolution and influences the time resolution dt of the measurement. 62

6.8 Schematics for the calibration of a current amplifier. The fast voltage jump U_{cal} is differentiated on a forming capacitance C_{cal}. The resulting pulse shape is measured as a reference. After attenuation, the current pulse is used for calibration. 63

6.9 Schematics for the calibration of a charge amplifier. The voltage step U_{cal} and the capacitance C_{cal} define the calibration charge Q_{cal}.The amplitude of the output signal compared to Q_{cal} gives the gain of the charge amplifier. 63

7.1 The Diamond Mosaic-Detector. 70

7.2 Two Diamonds as received by DDL, photos taken under the microscope (x10). Some of the diamonds had chipped off corners or cracks. 71

7.3 Mounting of DIAM1-DIAM5 for metallization. 72

7.4 Diamonds after the lithography, both pictures were taken with a cross-polarizer. 73

7.5 bla 74

7.6 Glueing and bonding of the DM-D. 76

8.1 SNR per 1 MeV deposited energy in diamond as a function of the input capacitance C for the CIVIDEC Cx-amplifiers. The working point of the DM-D is indicated at 35 pF, where SNR = 40/MeV. The calibration charge was $Q_{cal} = 12$ fC, which corresponds to 1 MeV in diamond. 79

8.2 Characterization of the CIVIDEC CX-amplifiers used with the DM-D. 79

8.3 Calibration of the CIVIDEC C2 broadband current amplifier. 80

9.1 bla 82

9.2 Dark current as a function of the electric field, for the different sensors of the DM-D. All diodes in the left panel were biased with +1 V/μm during the measurements. The DIAM diodes represented in the right panel were operated at a reduced bias voltage. The DOID was operated biased with -1 V/μm. 83

9.3 Saturation curves for all DIAM sensors of the DM-D. Due to the high leakage current, DIAM1 was only measured up to an electric field of 0.5 V/μm. DIAM6 does not reach saturation below 1 V/μm. 84

9.4 Calibration of the DIAM channels with the 4α-source. On top the results of the FLUKA simulation for the calibration setup, assuming $\epsilon = 13.6$ eV, can be seen. The diodes show various charge gains and differ in resolution, see Table A.1. The Gaussian fits to the different peaks are drawn in gray. 85

9.5 Calibration of the DOID channel with the 4α-source, in comparison with the simulated spectrum. There are no distinguishable peaks visible in the DOID spectrum, hence an energy resolution cannot be given for this diode. 87

9.6 Calibration of the particle spectra recorded with DIAM4. The experimental spectra, in color, are correlated by varying the charge yield with the spectra resulting from the FLUKA simulations for the 4α-calibration and the sample measurement. 88

9.7 Charge yield as a function of the particle's penetration depth for all sCVD diodes of the DM-D. The error bars indicate the confidence interval of the estimated charge yield from the correlation between experimental data and FLUKA simulations. . 89

11.1 Experimental setup at n_TOF during the ^{59}Ni(n,α) measurement campaign . . . 98

11.2 Photograph of the sample used for the ^{59}Ni(n,α)^{56}Fe cross-section measurement at n_TOF in 2012. The circular material deposition with 15 mm diameter can be seen in the center of the foil. 99

11.3 FLUKA simulation results for the expected particle spectra. The spectra are weighed with the cross-section of the corresponding reaction at thermal neutron energies. 100

11.4 Amplitude spectrum of DIAM2 for the first and the last recorded ^{59}Ni run. The gain shift in this diode became apparent via the position of the triton (t) peak of the ^{6}Li(n,α)^{3}H reaction. The gain stability during the ^{59}Ni measurement was monitored for all diodes via the position of the t-peak. 103

12.1 Exemplary experimental data in the raw data analysis program [1]. 106

12.2 Experimental data from DIAM9. 108

12.3 Deposited energy over neutron energy for the DM-D in the n_TOF neutron beam, from the Sample-out measurement. The number of recorded signals is encoded in colour. 109

12.4 Background spectrum of the DM-D in the n_TOF neutron beam. The evaluated neutron cross-section data of the different isotopes is scaled to the spectrum, to show the individual contributions which could be identified. The in-beam γ at n_TOF are the main contribution to the background in the keV region. 110

12.5 TOF to E$_n$ calibration by fitting the non-relativistic expression for the neutron energy as a function of TOF for visible resonances in the background spectrum. . 111

12.6 Result of the TOF to E$_n$ calibration and comparison with the different cross-sections related to the resonant background. 112

12.7 Background from the DM-D (Sample-out) in comparison with the Dummy measurement. The contribution of the in-beam γ increases by a factor 3 when the Pt foil is positioned in front of the detector. 112

12.8 Amplitude over E$_n$ for DIAM9 with the amplitude thresholds used to select only α from ^{59}Ni(n,α)^{56}Fe or tritons from ^{6}Li(n,α)^{3}H. 113

12.9 Comparison of E_n-spectra for the sample and Dummy measurement with DIAM9. 114

12.10 Sum of all particle spectra at the resonance (190 eV $\leq E_n \leq$ 220 eV), where the spectra outside the resonance were subtracted. The protons of ^{59}Ni(n,p)^{59}Co are visible at the corresponding energy of 1.8 MeV, and the alphas at 4.8 MeV. The results of the FLUKA simulations were convoluted with the average energy resolution of the DM-D of $dE = 78.5$ keV (^{148}Gd calibration at $E_\alpha = 3.183$ MeV). 115

12.11 Amplitude spectrum of DIAM9 for E$_n \leq$ 1 keV. The set thresholds are indicated as vertical lines. The Landau-fit which was used for the efficiency correction is shown in blue for the α-spectrum of ^{59}Ni and in green for the t-spectrum of ^{6}Li. . 115

12.12 Evaluation of the product of beam-interception factor and geometrical efficiency BIF$\cdot\varepsilon$ for DIAM9. 116

12.13 ^{59}Ni(n,α)^{56}Fe yield for DIAM9. 118

12.14 ^{59}Ni(n,α)^{56}Fe cross-section measured with the DM-D at n_TOF, top panel, with the statistical uncertainty for each bin shown in the bottom panel. Following a conservative estimation, the correlated uncertainty is 4.2%. 119

13.1 ^{59}Ni(n,α)^{56}Fe cross-section at the dominant resonance, experimental and evaluated nuclear data. The libraries ROSFOND-2010, ENDF/B-VII.1 and ENDF/B-VII.0 are equivalent to JEFF-3.1 *. 122

13.2 ^{59}Ni(n,α)^{56}Fe cross-section, experimental and evaluated nuclear data. The libraries ROSFOND-2010, ENDF/B-VII.1 and ENDF/B-VII.0 are equivalent to JEFF-3.1 *. 122

13.3 The Diamond Mosaic-Detector. 125

13.4 ^{59}Ni(n,α)^{56}Fe cross-section at the dominant resonance, experimental and evaluated nuclear data. The libraries ROSFOND-2010, ENDF/B-VII.1 and ENDF/B-VII.0 are equivalent to JEFF-3.1 *. 126

List of Tables

2.1 Number of neutrons per $7 \cdot 10^{12}$ pot in different neutron energy (E_n) ranges for the capture collimator (18 mm diameter) and borated water as neutron moderator. 16

5.1 Electronic properties of diamond, the range of published values are listed as well as the values which are used as reference in this work. 46

8.1 Bias voltage, capacitance and corresponding amplifier for each channel of the Diamond Mosaic-Detector during the measurement at n_TOF. 78

9.1 bla 86

9.2 Resulting energy resolution dE in keV from the Gauss fits to the peaks corresponding to the individual isotopes. In general, the resolution improves with increasing particle energy. For the ^{148}Gd peak of DIAM1 and DIAM8 the approximation of a Gauss distribution is not applicable (n.a.). 86

9.3 Range and energy E of the different charged particles measured with the DM-D. 88

11.1 Specifications of the sample; the reaction to be measured is listed as well as the maximum energies of the reaction products which can reach the detector (α ... ^{4}He nucleus, t ... triton = ^{3}H nucleus, p ... proton = ^{1}H nucleus). 99

11.2 Dates, proton budget and the corresponding neutron budget for the measurements performed during the ^{59}Ni(n,α)^{56}Fe campaign at n_TOF in 2012. The number of dedicated TOF pulses, with an intensity of $7 \cdot 10^{12}$ protons per pulse (ppp), and the number of parasitic pulses, with $2 \cdot 10^{12}$ ppp, are listed as well. 102

11.3 Gain stability of the diodes during the ^{59}Ni runs. 103

12.1 The resulting BIF·ε from the linear fit to the ratio Y_{ex}/Y_{th} and BIF·ε normalized to the area of the respective diode (BIF·ε/mm^2) for all channels of the DM-D. The neutron-beam spot was apparently shifted to the bottom right during the measurement. According to FLUKA simulations, the efficiency ε of the experimental setup is 45.7%. 117

12.2 Contributions to the systematic uncertainty of the measurement and cross-section evaluation. 118

A.1 Results of the Gauss fits to the peaks corresponding to α form the four isotopes contained in the calibration source. The main α-energy for each isotope with the corresponding intensity is given beyond the isotopes name. For ^{239}Pu, ^{241}Am and ^{244}Cm a summation of multiple Gauss functions, corresponding to multiple E_α, was used as fit function. 130

A.2 The Diamond Mosaic-Detector as seen from the neutron beam. The dimensions of the diodes are given in mm x mm x mm. The 500 μm thick sCVD diamond and the Si diode were intended to be used for additional background measurements. 131

A.3 Current over Voltage behavior of the Diamond Mosaic-Detector. DIAM1 and DIAM8 show a leakage current that is 2-3 orders of magnitude to high for negative voltage. 132

A.4 Experimental data recorded with the Diamond Mosaic-Detector during the sample measurement (^{59}Ni, ^{6}Li) at n_TOF. 133

A.5 Particle spectra for E$_n \leq$ 500 keV, recorded with the Diamond Mosaic-Detector during the sample measurement (^{59}Ni, ^{6}Li) at n_TOF. The Landau fit to the distribution corresponding to tritons of ^{6}Li(n,α)^{3}H and α of ^{59}Ni(n,α)^{56}Fe is indicated in green and blue respectively. The implemented thresholds are indicated as vertical lines. 134

Part V

BIBLIOGRAPHY

Bibliography

[1] D. Upper, *The unsuccessful Self-Treatment of a Case of "Writer's Block"*, Journal of applied Behavior Analysis, **7**(3):497 (1974).

[2] E. Sheldon (Editor), *Neutron Resonances: Neutron Reaction Mechanisms and Nuclear Structure*, CONF-760715-P1 (1976).

[3] P. Koehler, et al., *^{59}Ni(n,α) Measurement*. Private Communication.

[4] E. Rutherford, *The scattering of α and β Particles by Matter and the Structure of the Atom*, Philosophical Magazine, **21**(6):669–688 (1911).

[5] J. Praena, et al., *Micromegas Detector for ^{33}S(n,α) cross section measurement at n_ TOF*, Cern-intc-2012-006 / intc-p-322, CERN (2012).

[6] M. Arnould, et al., *The p-process of stellar nucleosynthesis: astrophysics and nuclear physics status*, Physics Reports, **384**(1-2):1–84 (2003).

[7] W. Hauser, et al., *The Inelastic Scattering of Neutrons*, Phys. Rev., **78**(366-373) (1952).

[8] C. Massimi, et al., *Measurement of the ^{25}Mg(n,α)^{22}Ne reaction cross-section at n_ TOF EAR-2*, CERN.

[9] C. M. Baglin, *Nuclear Data Sheets for A = 59*, Nuclear Data Sheets, **95**(215) (2002).

[10] F. Käppeler, et al., *Nuclear Input for the s process: Progress with Experiments and Theory*, Nuclear Physics A, **777**:291–310 (2006).

[11] I. J. Thompson, et al., *Nuclear Reactions for Astrophysics*, Cambridge University Press (2009).

[12] C. Lederer, et al., *Neutron Capture Cross Section of Unstable ^{63}Ni: Implications for Stellar Nucleosynthesis*, Physical Review Letters, **PRL 110**(022501) (2013).

[13] M. Pignatari, et al., *The weak s-Process in massive Stars and its Dependence on the Neutron Capture Cross Sections*, The Astrophysical Journal, **710**:1557–1577 (2010).

[14] O. N. E. Agency, *Comparison Calculations for an Accelerator-driven Minor Actinide Burner*, Tech. rep., NEA/NSC/DOC (2001).

[15] M. J. Loughlin, *ITER - Activation of Blanket Module*, Tech. rep., ITER (2008).

[16] B. Goel, *Inportance and Status of (n,α)-Cross Sections for a Reliable Prediction of Radiation Damage in Stainless Steel*, KFK 2473, Kernforschungszentrum Karlsruhe (1977).

[17] V. Gopalakrishnan, et al., *Comparison of calculated Helium Production in Stainless Steel due to Neutron Irradiation with Experiment*, Journal of Nuclear Materials, **228**:207–214 (1996).

[18] H. Ugachi, et al., *Development of Test Techniques for In-Pile SCC Initiation and Growth Tests and the Current Status of In-Pile Testing at JMTR*, in *Proceedings of 12th International Conference on Environmental Degradation of Materials in Nuclear Systems-Water Reactors*, pp. 319 – 325, SaltLakeCity, USA (2005).

[19] J. A. Harvey, et al., *(n,α), (n,p), (n,γ) and total neutron-cross-sections measurements on 59Ni*, in *Int. Conf. on Interact. of Neutr. with Nuclei*, vol. 1, p. 143, Lowell USA (1976).

[20] J. McDonald, et al., *Measurements of thermal neutron cross-sections for He production in Ni-59*, in *Conf. in Physics*, Gothenburg, Sweden (1975).

[21] H. M. Eiland, et al., *Measurements of the Ni-59(n,α) Cross Section for Thermal Neutrons*, Nuclear Science and Engineering, **53**:1 (1974).

[22] R. D. Werner, et al., *Measured Thermal-Neutron Cross Section for the 59Ni(n,α)56Fe Reaction*, Nuclear Science and Engineering, **56**:98 (1975).

[23] M. Pomorski, *Electronic Properties of Single Crystal CVD Diamond and its Suitability for Particle Detection in Hadron Physics Experiments*, Ph.D. thesis, Johann Wolfgang Goethe - Universitaet, Frankfurt am Main (2008).

[24] E. Griesmayer, et al., *High-Resolution Energy and Intensity Measurements with CVD Diamond at REX-ISOLDE*, Be-note-2009-028, CERN (2009).

[25] T. R. Collaboration, *Radiation Hardness Studies of CVD Diamond Detectors*, Nuclear Instruments and Methods in Physics Research A, **367**:207–211 (1995).

[26] C. Kurfürst, *Cryogenic Beam Loss Monitoring for the LHC*, Ph.D. thesis, Vienna University of Technology (2013).

[27] C. Rubbia, et al., *A high Resolution Spallation driven Facility at the CERN-PS to measure Neutron Cross Sections in the Interval from 1 eV to 250 MeV*, Cern/lhc/98-002-eet, CERN (1998).

[28] K. Fujii, et al., *Neutron Physics of the Re/Os clock. III. Resonance analysis and stellar (n,γ) cross sections of ^{186,187,188}Os*, Physical Review C, **82**(015804) (2010).

[29] F. Käppeler, et al., *The s process: Nuclear Physics, Stellar Models, and Observations*, Rev. Mod. Phys., **83**:157 – 193 (2011).

[30] N. Colonna, et al., *Advanced Nuclear Energy Systems and the Need of Accurate Nuclear Data: The n_ TOF Project at CERN*, Energy Environ. Sci., **3**:1910–1917 (2010).

[31] F. Gunsing, et al., *Spin Assignments of nuclear Levels above the Neutron Binding Energy in* ^{88}*Sr*, Cern-intc-2011-030 / intc-p-304, CERN (2011).

[32] E. Chiaveri, et al., *Proposal for n_ TOF Experimental Area2 (EAR-2)*, Cern-intc-2012-029 / intc-o-015, CERN (2012).

[33] C. Guerrero, et al., *Perfomance of the neutron time-of-flight facility n_ TOF at CERN*, Eur. Phys. J. A, **49**(27) (2013).

[34] M. Barbagallo, et al., *High-accuracy determination of the neutron flux at n_ TOF*, Eur. Phys. J. A, **49**(156) (2013).

[35] C. Coceva, et al., *On the Figure of Merit in Neutron Time-of-Flight Measurements*, NIMA, **489**:346–356 (2002).

[36] F. Gunsing, et al., *Measurement of resolved resonances of* ^{232}*Th(n,*γ*) at the n_ TOF facility at CERN*, Physical Review C, **85**(064601) (2012).

[37] A. D. Carlson, et al., *International Evaluation of Neutron Cross Section Standards*, Nuclear Data Sheets, **110**:3215–3324 (2009).

[38] T. n_TOF collaboration, *The data acquisition system of the neutron time-of-flight facility n_ TOF at CERN*, NIMA, **538**(1-3):692–702 (2005).

[39] G. Lorusso, et al., *Time-energy relation of the n_ TOF neutron beam: energy standards revisited*, NIMA, **532**:622–630 (2004).

[40] E. Griesmayer, *The Gamma Flash, Study with a Diamond Detector*, in *n_ TOF Collaboration Meeting* (2013).

[41] *R. Steerenberg Privat Communication* (2013).

[42] K. H. Beckurts, et al., *Neutron Physics*, Springer Verlag (1964).

[43] N. Bohr, et al., *The Mechanism of Nuclear Fission*, Phys. Rev., **56**:426–450 (1939).

[44] C. G. Sanchez, *Measurements of the* ^{237}*Np and* ^{240}*Pu Neutron Capture Cross Sections at the CERN n_ TOF Facility*, Ph.D. thesis, Universidad Complutense de Madrid (2008).

[45] W. Heisenberg, *Über den anschaulichen Inhalt der quantentheoretischen Kinematik und Mechanik*, Zeitschrift für Physik, **43**:172–198 (1927).

[46] G. Breit, et al., *Capture of slow Neutrons*, Phys. Rev., **49**:519–531 (1936).

[47] C. E. Rolfs, et al., *Cauldrons in the Cosmos*, The University of Chicago Press (1988).

[48] J. Beringer, et al., *The Review of Particle Physics*, Phys. Rev. D, **86**(010001) (2012).

[49] G. F. Knoll, *Radiation Detection and Measurement*, John Wiley & Sons, Ltc., 4th ed. (2010).

[50] *Stopping Powers and Ranges for Protons and Alpha Particles*, ICRU Report No. 49 (1993).

[51] H. Bichsel, *A method to improve tracking and particle identification in TPCx and silicon detectors*, Nuclear Instruments and Methods in Physics Research A, **562**:154–197 (2006).

[52] A. Einstein, *Über einen die Erzeugung und Verwandlung des Lichtes betreffenden heuristischen Gesichtspunkt*, Annalen der Physik, **17**(6):132–148 (1905).

[53] C. Weiß, et al., *Response of CVD Diamond Detectors to 14 MeV Neutrons*, Tech. Rep. CERN-ATS-Note-2012-093 TECH, CERN (2012).

[54] J. M. Zazula, *On Graphite Transformations at High Temperature and Pressure Induced by Absorption of the LHC Beam*, LHC Project Note 78/97, CERN (1997).

[55] J. W. Anthony, et al., *Handbook of Mineralogy*, Mineralogical Society of America (1990).

[56] J. Koike, et al., *Displacement Threshold Energy for Type IIa Diamond*, Applied Physics Letters, **60**:1450–2452 (1992).

[57] *Element Six Ltd.*
URL `http://www.e6cvd.com/cvd/page.jsp?pageid=415`

[58] A. Oh, et al., *A novel detector with graphitic electrodes in CVD diamond*, Diamond and Related Materials, **38**:9–13 (2013).

[59] A. R. Lang, *The Properties of Diamond*, Academic Press, London (1979).

[60] J. H. Robertson, *Gems made by man*, Acta Crystallographica Section B, **37**(2):493 (1981).

[61] J. E. Field (Editor), *The properties of natural and synthetic diamond*, Academic Press, London (1992).

[62] M. H. Nazare, et al. (Editors), *Diamond*, INSPEC, London (2001).

[63] L. S. Pan, et al., *Diamond: Electronic Properties and Applications*, Kluwer Academic Publ., Boston, MA (1995).

[64] P. W. May, *Diamond Thin Films: a 21st-Century Material*, Phil. Trans. R. Soc. Lond. A, **358**:473 (2000).

[65] *A CVD diamond detector for (n,α) cross-section measurements*, 015, PoS(ENAS 6) (2011).

[66] B. Dehning, et al., *Overview of LHC Beam Loss Measurements*, Proceedings of IPAC 2011, Beam Diagnostics and Instrumentation, pp. 2854–2856 (2012).

[67] M. Hempel, et al., *Bunch to Bunch Beam Loss Diagnostics with Diamond Detectors at the LHC*, in *Advanced Beam Dynamics Workshop on High-Intensity and High-Brightness Hadron Beams 2012*, vol. MOP203 (2012).

[68] M. Mikuz, et al., *The ATLAS Beam Conditions Monitor*, IEEE, **3**:1914–1917 (2007).

[69] F. Burkart, et al., *Diamond Particle Detectors Properties during High Fluence Material Damage Tests and their Future Applications for Machine Protection in the LHC*, in *Proceedings of the IPAC 2013 Conference*, Shanghai (2013).

[70] H. Jansen, *Chemical Vapour Deposition Diamond: Charge Carrier Movement at Low Temperatures and Use in Time-Critical Applications*, Ph.D. thesis, Rheinische Friedrich-Wilhelms-Universität Bonn (2013).

[71] T. Teraji, *Chemical Vapor Deposition of Homoepitaxial Diamond Films*, Phys. Status Solidi A, **203**(13):3324 (2006).

[72] M. Schreck, et al., *Diamond nucleation on iridium buffer layers and subsequent textured growth: a route for the realization of single-crystal diamond films*, Appl. Phys. Lett., **78**(192) (2001).

[73] S. Gsell, et al., *A route to diamond wafers by epitaxial deposition on silicon via iridium / yttria stabilized zirconia buffer layers*, Appl. Phys. Lett., **84**(4541) (2004).

[74] J. Isberg, *CVD Diamond for Electronic Devices and Sensors, Chapter 2*, ISBN:978-0-470-06532-7, John Wiley & Sons, Ltc. (2009).

[75] E. Griesmayer, *Measurement with Diamond Detectors at Temperatures up to $T = 520$ K.* Private Communication.

[76] T. H. Borst, et al., *Boron-Doped Homoepitaxial Diamond Layers: Fabrication, Characterization and Electronic Applications*, Phys. Status Solidi A, **154**:423–444 (1996).

[77] L. Reggiani, et al., *On the Lattice Scattering and Effective Mass of Holes in natural Diamond*, Solid State Commun., **30**:333–335 (1979).

[78] F. Nava, et al., *Electron effective Masses and Lattice Scattering in natural Diamond*, Solid State Commun., **33**:475–477 (1980).

[79] L. Reggiani, et al., *Hole-Drift Velocity in Natural Diamond*, Phys. Rev. B, **23**:3050–3057 (1981).

[80] H. Pernegger, et al., *Charge-carrier properties in synthetic single-crystal diamond measured with the transient-current technique*, J. Appl. Phys., **97**(073704) (2005).

[81] M. Pomorski, et al., *Development of Single-Crystal CVD-Diamond Detectors for Spectroscopy and Timing*, Phys. Status Solidi A, **203**(12):3152–3160 (2006).

[82] R. C. Alig, et al., *Scattering by Ionization and Phonon Emission in Semiconductors*, Physical Review B, **22**(12):5565 (1980).

[83] J. Kaneko, et al., *Diamond Radiation Detector using a synthetic IIa Type Mono-Crystal*, Nuclear Instruments and Methods in Physics Research A, **383**(2-3):547 (1996).

[84] A. Owens, et al., *Compound Semiconductor Radiation Detectors*, Nuclear Instruments and Methods in Physics Research A, **531**(1-2):18 (2004).

[85] J. H. Kaneko, *Radiation Detector made of a Diamond Single Crystal Grown by a Chemical Vapor Deposition Method*, Nuclear Instruments and Methods in Physics Research A, **505**(1-2):187 (2003).

[86] W. Shockley, *Currents to Conductors Induced by a Moving Point Charge*, J. Appl. Phys., **9**:635–636 (1938).

[87] Proceedings of the I.R.E., *Currents Induced by Electron Motion*, 584-585 (1939).

[88] C. Weiß, et al., *Investigation of Diamond on Iridium Detector Materials for Spectroscopic Applications*, Tech. Rep. CIVIDEC NOTE/CW/2012-12-01/001, CIVIDEC Instrumentation GmbH (2012).

[89] P. Kavrigin, Ph.D. thesis, Vienna University of Technology (under preparation).

[90] P. J. Bryant, *Signal analysis for semiconductor diode detectors with trapped charges*, Tech. Rep. CIVIDEC NOTE/PJB/2013-05-14/011, CIVIDEC Instrumentation GmbH (2013).

[91] E. Griesmayer, *Beam Loss Measurements with Diamonds*, in *2nd ADAMAS Workshop*, GSI Darmstadt (2013).

[92] C. Weiß, et al., *Pulse Shape Analysis for Neutron Interactions in sCVD Diamond Detectors*, Tech. Rep. CIVIDEC NOTE/CW/2013-05-18/002, CIVIDEC Instrumentation GmbH (2013).

[93] E. Griesmayer, *Schnelle Messsignalverarbeitung*, Vienna University of Technology, VO 354.001 (2013).

[94] J. B. Johnson, *Thermal Agitation of Electricity in Conductors*, Phys. Rev., **32**:97–109 (1928), doi:10.1103/PhysRev.32.97.
URL http://link.aps.org/doi/10.1103/PhysRev.32.97

[95] H. Nyquist, *Thermal Agitation of Electric Charge in Conductors*, Phys. Rev., **32**:110–113 (1928), doi:10.1103/PhysRev.32.110.
URL http://link.aps.org/doi/10.1103/PhysRev.32.110

[96] C. W. Fabjan, et al., *Calorimetry for Particle Physics*, Cern-ep/2003-075, CERN (2003).

[97] U. Fano, *Ionization Yield of Radiations. II. The Fluctuations of the Number of Ions*, Phys. Rev., **72**(1) (1947).

[98] R. Frühwirth, *Analysis and Smoothing of Diamond Detector Signals*, Tech. Rep. CIVIDEC NOTE/RF/2012-11-12/001, CIVIDEC Instrumentation GmbH (2012).

[99] *Cividec Instrumentation GmbH.*
URL www.cividec.at

[100] *Diamond Detectors Ltd.*

[101] *CEA, LIST, Diamond Sensors Laboratory.*

[102] G. Battistoni, et al., *The FLUKA code: Description and benchmarking*, in M. Albrow, et al. (Editors), *AIP Conference Proceeding*, vol. 896 of *Proceedings of the Hadronic Shower Simulation Workshop 2006*, pp. 31–49 (2007).

[103] A. Ferrari, et al., *FLUKA: a multi-particle transport code*, Tech. rep., CERN-2005-10, INFN/TC_05/11, SLAC-R-773 (2005).

[104] *R. Fruehwirth Private Communication* (2012).

[105] S. Raman, et al., *Angular Anisotropy in the* $^6Li(n,\alpha)^3H$ *Reaction in the eV and keV Energy Region.*, in *Proc. Int. Conf. on Interactions of Neutrons with Nuclei*, vol. CONF-760715-72, p. 1340 (1976).

[106] M. Cerv, *Diamonds as versatile Beam Monitors*, Ph.D. thesis, Vienna University of Technology (under preparation).

Curriculum Vitae

Christina Weiss
Date of Birth: 25. July 1978
Place of Birth: Vienna / Austria
Citizenship: Austria

Research Experience
since 09/2013 CERN Fellow at the n_TOF Experiment
08/2010 - 07/2013 CERN Doctoral Student
08/2009 - 06/2010 Vienna Inst. of Atomic and Subatomic Physics as Master Student
07/2009 - 08/2009 n_TOF experiment at CERN as Master Student
10/2008 - 06/2009 Institute of Quantum Optics and Information, Univ. of Vienna
09/2008 Institute for Solid State Physics of the Vienna Univ. of Technology

Education
Vienna University of Technology, Vienna, Austria
CERN, Geneva, Switzerland

- 2010 - 2014: PhD Technical Physics, *A CVD Diamond Detector for (n,α) Cross-Section Measurements*
  Advisor: Prof. Gerald Badurek
  Area of Study: Experimental Nuclear Physics
- 10/2007 - 06/2010: M.S. Technical Physics, *Fluence measurement at the neutron time of flight experiment at CERN*
  Advisor: Prof. Gerald Badurek
  Area of Study: Applied Nuclear Physics

Graz University of Technology, Graz, Austria

- 10/2004 - 09/2007: B.S. Technical Physics, *Quantumteleportation*
  Advisor: Prof. Hans Gerd Evertz
  Area of Study: Quantum Mechanics

Previous Career
09/1997 - 09/2000 **Academy of Physiotherapy, WSP Wien**, Vienna, Austria
10/2000 - 09/2004 Work as a Physiotherapist in the neurological Hospital
Neurologisches Zentrum Otto Wagner Spital, Vienna, Austria
2001 - 2010 Work as freelance Physiotherapist in Austria